MEMS BASED MULTI-MODE MULTI-CHANNEL PIEZOELECTRIC SENSOR FOR FULLY IMPLANTABLE COCHLEAR IMPLANTS

A THESIS SUBMITTED TO
THE GRADUATE SCHOOL OF NATURAL AND APPLIED SCIENCES
OF
MIDDLE EAST TECHNICAL UNIVERSITY

BY

FEYZA PIRIM

IN PARTIAL FULFILLMENT OF THE REQUIREMENTS
FOR
THE DEGREE OF MASTER OF SCIENCE
IN
MICRO AND NANOTECHNOLOGY

SEPTEMBER 2022

Approval of the thesis:

MEMS BASED MULTI-MODE MULTI-CHANNEL PIEZOELECTRIC SENSOR FOR FULLY IMPLANTABLE COCHLEAR IMPLANTS

submitted by **FEYZA PIRIM** in partial fulfillment of the requirements for the degree of **Master of Science** i**n Micro and Nanotechnology, Middle East Technical University** by,

Prof. Dr. Halil Kalıpçılar
Dean, Graduate School of **Natural and Applied Sciences** _____

Prof. Dr. Deniz Üner
Head of the Department, **Micro and Nanotechnology** _____

Prof. Dr. Haluk Külah
Supervisor, **Micro and Nanotechnology, METU** _____

Assoc. Prof. Dr. Mehmet Bülent Özer
Co-Supervisor, **Mechanical Eng., METU** _____

Examining Committee Members:

Prof. Dr. Tayfun Akın
Electrical and Electronics Eng, METU _____

Prof. Dr. Haluk Külah
Micro and Nanotechnology, METU _____

Assoc. Prof. Dr. Mehmet Bülent Özer
Mechanical Eng. Dept., METU _____

Assoc. Prof. Dr. Ender Yıldırım
Mechanical Eng. Dept., METU _____

Assist. Prof. Dr. Erdinç Tatar
Electrical and Electronics Eng, Bilkent University _____

Date: 05.09.2022

I hereby declare that all information in this document has been obtained and presented in accordance with academic rules and ethical conduct. I also declare that, as required by these rules and conduct, I have fully cited and referenced all material and results that are not original to this work.

Name Last name : Feyza Pirim

Signature :

ABSTRACT

MEMS BASED MULTI-MODE MULTI-CHANNEL PIEZOELECTRIC SENSOR FOR FULLY IMPLANTABLE COCHLEAR IMPLANTS

Pirim, Feyza
Master of Science, Micro and Nanotechnology
Supervisor : Prof. Dr. Haluk Külah
Co-Supervisor: Assoc. Prof. Dr. Mehmet Bülent Özer

September 2022, 130 pages

This thesis presents a novel multi-mode, multi-channel piezoelectric sensor with broad bandwidth that is placed on the ossicles via an attachment system. The proposed sensor collects the vibration of the ossicles and mechanically filters the incoming sound.

The finite element model of the middle ear is constructed as a starting point to examine the characteristics of the middle ear. The vibration characteristic of the ossicle chain is studied and the most suitable locations for the sensor placement are discussed. The attachment mechanism is designed. The finite element model of the middle ear and the attachment mechanism is verified with the cadaver experiments.

Requirements and limitations of the sensor are presented. Thin film pulsed laser deposited PZT is selected as piezoelectric material. The proposed sensor design is composed of 4 multi-mode M-shape cantilevers together with 11 standard cantilevers. It has a volume of $4.6\times4.2\times0.5$ mm^3. Resonance frequencies of the cantilevers are tuned by using finite element methodology.

The performance of the sensor is examined experimentally. It is observed that multi-mode, multi-channel sensor can fully perform at 0.1g for the interval of 300Hz and

6kHz. Acoustic performance characterization of the sensor is conducted by placing the sensor on the artificial tympanic membrane. Sensor gives peak-to-peak voltage readouts of 546.2mV$_{pp}$, 252.6mV$_{pp}$, and 69.7mV$_{pp}$ at 100dB, 90dB and 80dB respectively.

An alternative multi-mode design P-shape is presented. A maximum of 120.5mV$_{pp}$ is recorded from the P-shape design at 0.1g. Its results are examined and compared with M-shape multi-mode design.

Keywords: cochlear implants, MEMS, piezoelectric sensor, PLD PZT, multi-mode cantilever

ÖZ

TAMAMEN İMPLANTE KOKLEAR İMPLANTLAR İÇİN MEMS TABANLI ÇOK MODLU ÇOK KANALLI PIEZOELEKTRİK SENSÖR

Pirim, Feyza
Yüksek Lisans, Mikro ve Nanoteknoloji
Tez Yöneticisi: Prof. Dr. Haluk Külah
Ortak Tez Yöneticisi: Doç. Dr. Mehmet Bülent Özer

Eylül 2022, 130 sayfa

Bu tez, bir bağlantı sistemi aracılığıyla kemikçiklere yerleştirilen geniş bant genişliğine sahip yeni çok modlu, çok kanallı piezoelektrik sensör sunmaktadır. Önerilen sensör, kemiklerin titreşimini toplar ve gelen sesi mekanik olarak filtreler.

Orta kulağın özelliklerini incelemek için bir başlangıç olarak orta kulağın sonlu elemanlar modeli oluşturulmuştur. Kemik zincirinin titreşim karakteristiği incelenmiş ve sensör yerleşimi için en uygun yerler tartışılmıştır. Bağlantı mekanizması konuma göre tasarlanmıştır. Orta kulağın sonlu elemanlar modeli ve bağlanma mekanizması kadavra deneyi ile doğrulanmıştır.

Sensörün gereksinimleri ve sınırlamaları sunulmuştur. Piezoelektrik malzeme olarak ince film darbeli lazerle biriktirilmiş PZT seçilmiştir. Önerilen sensör tasarımı, 11 normal konsol ile birlikte 4 çok modlu M-şekilli konsoldan oluşmaktadır. $4.6\times4.2\times0.5$ mm^3 hacme sahiptir. Konsolların rezonans frekansları, sonlu elemanlar metodolojisi kullanılarak ayarlanmıştır.

Sensörün performansı deneysel olarak incelenir. Çok modlu, çok kanallı sensörün 300Hz ve 6kHz aralığında 0.1g'de tam performans gösterdiği gözlemlenmiştir. Sensörün akustik performans karakterizasyonu, sensör yapay kulak zarı üzerine

yerleştirilerek gerçekleştirilir. Sensör, sırasıyla 100dB, 90dB ve 80dB'de 546.2mVpp, 252.6mVpp ve 69.7mVpp'lik tepeden tepeye voltaj okumaları verir.

Alternatif çok modlu P-şekli tasarımı sunulmaktadır. 0.1g'de P-şekilli tasarımdan maksimum 120.5mVpp kaydedilir. Sonuçları incelenmiş ve M-şekilli çok modlu tasarımla karşılaştırılmıştır.

Anahtar Kelimeler: koklear implantlar, MEMS, piezoelektrik sensör, PLD PZT, çok modlu konsol

To my precious family

ACKNOWLEDGMENTS

I would like to express my deepest gratitude to my supervisor Prof. Dr. Haluk Külah for the support and guidance he gave me during my graduate study and also for giving me the opportunity to work on an exciting project. I am also grateful to my co-advisor Assoc. Prof. Dr. Mehmet Bülent Özer for his valuable guidance, comments, and support.

I am deeply thankful to Ali Can Atik for his great support, contribution, and friendship during this research. He inspired me in so many ways and our discussions helped me a lot in my research and increased my critical thinking skills. I also would like to thank Berat Yüksel for his help and support.

I am very happy to have Dr. Aykan Batu in our group with so much life experience he shares. Further, I would also like to thank Dicle Balcı, Akın Mert Yılmaz, and Pamir Kıldiş for their great friendship and collaborations. I would like to also thank all members of the BioMEMS research group for their collaborations, support, and friendship. In no specific order, I am thankful to Cansu Aslantürk, Beyhan Türkyılmaz, Özlem Topçu, Anıl Aydın, Mert Doğan, Zeynep Çağlayan, Aziz Koyuncuoğlu and Berkay Özbek. I am honored and enjoyed sharing the same office while creating beautiful memories. My special thanks go to METU-MEMS Center staff for their kind help in the cleanroom.

I am deeply thankful to all my friends for their encouragement and support. I would like to sincerely thank Hatun Taşkaya, Hatem Ak, and Elif Tola for such a great friendship. I am deeply thankful to Merve Saraç for being always one call away from me and for her great friendship through the years. I am especially thankful to Denge Uzel for being always there for me, for her endless support, and for her great friendship through the years. I am lucky to have her beside me.

I would like to express my deepest gratitude to my parents Ali and Gül Pirim for their never-ending support, encouragement, and unconditional love throughout my life. I would especially like to thank my brother, Ömeralp Pirim for his support, faith,

and advice during my entire life. I am thankful to him for turning every situation into such fun and for being such an inspiration source to me whole my life. I am proud to be his little sister.

This author is financially supported by TUBITAK BIDEB 2210-A 2020/2 Scholarship during this study.

This work has received funding from the European Research Council (ERC) under the European Union's Horizon 2020 research and innovation program (Grant No:682756).

TABLE OF CONTENTS

LIST OF TABLES

TABLES

LIST OF FIGURES

FIGURES

CHAPTER 1

INTRODUCTION

Advances in technology bring the requirement for very small electromechanical parts. Micro-Electro-Mechanical Systems, or MEMS, is a field that arises due to this requirement. With the MEMS technology, the mechanical and electrical parts that are normally produced in conventional manufacturing techniques can be produced in the dimension range of a few microns. Thus, with this technology, size limitations can be overcome. MEMS devices vary in complexity from basic structures with no moving parts to very sophisticated electromechanical systems with several mechanical components controlled by integrated microelectronics. It is an interdisciplinary field that utilizes different specialties such as mechanical engineering, electrical engineering, chemical engineering, and material engineering. This interdisciplinary nature of MEMS creates various applications in the market.

BioMEMS is a special field of MEMS that focuses on biocompatible micro systems. First, the application of the BioMEMS was based in 1967. S. B. Carter published a paper in 1967 describing the use of shadow-evaporated palladium islands for cell attachment [1]. After this breakdown, the BioMEMS field grew slowly for a while and in the 1990s it started to develop again. With the 2020 Corona pandemic, demand in the BioMEMS market shows a high rise. The Global BioMEMS market had 3.7 billion dollars' worth in 2019 and it is expected to become 6.3 billion by 2025 [2].

One of the most promising applications of BioMEMS is implantable systems. Various microelectronic and micromechanical sensors, such as gyroscopes, accelerometers, and transducers, may now be embedded in a tiny area on a rigid or flexible substrate with great sensitivity at a cheap cost because of advancements in packaging and manufacturing methods. Pacemakers are the most popular examples of implantable sensor applications of BioMEMS. Another possibility is cochlear

implants. There is a gap in the market about fully implantable cochlear implants and MEMS technology, especially when it is thought that according to the WHO, nearly 2.5 billion people are expected to suffer hearing loss by 2050, with at least 700 million requiring hearing rehabilitation. [3].

In this research, a MEMS-based piezoelectric sensor is tried to develop for hearing losses which makes mechanical filtering to the incoming sound and provides a hearing. It aims to overcome the problems with conventional cochlear implants and provides a more efficient and new solution to hearing disorders.

In this chapter, firstly general information about ear anatomy is presented. Then, it continues with hearing disorders and conventional solutions to them. A general literature review of implantable sensors is expressed to provide insight into recent developments in this area. Finally, the motivation and aim of the research are presented together with the organization scheme of the thesis.

1.1 Ear Anatomy

The ear is the organ of the mammalian which provides hearing and equilibrium. It is composed of three sections external ear, middle ear, and inner ear. In Figure 1.1 [4], an illustration of the ear is presented.

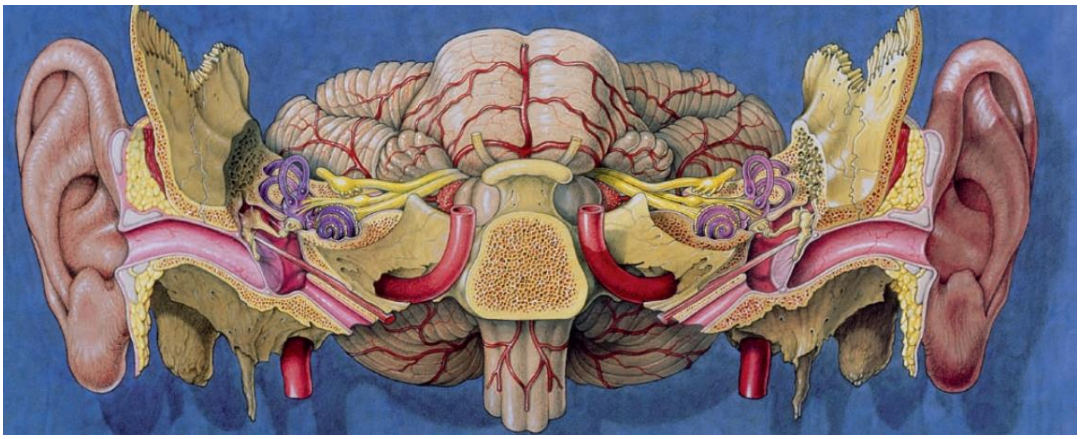

Figure 1.1. Illustration of the ear [4]

In Figure 1.2, the ear and its components are described. The external ear is composed of the pinna and ear canal. Pinna (auricle) is the outer part of the ear and the ear canal is the part that connects the middle ear and external ear. The ear canal is a tiny channel that connects the eardrum to the outside world. Sound travels in waves from the ear canal to the eardrum through a thin tube called the ear canal. Sound waves are 'caught' by the pinna and sent via the ear canal to the middle ear. The eardrum vibrates as a result of the incoming sound waves. The process of comprehending these sound waves starts here. The eardrum, i.e., the tympanic membrane, is the thin membrane-based part of the ear that separates the middle ear and external ear. The middle ear is composed of two main sections which are ossicles and the eustachian tube. Ossicles are three small bones, malleus, incus, and stapes respectively. The eustachian tube is the canal in which the middle ear and the back of the nose are connected. The eustachian tube aids in the equalization of middle ear pressure. For optimal sound wave transmission, equalized pressure is required. The last part of the ear is the inner ear. The inner ear is composed of three parts cochlea, vestibule, and semi-circular canals. The cochlea is where the hearing nerves are located. The vestibule contains balancing receptors. Semi-circular canals contain balancing receptors.

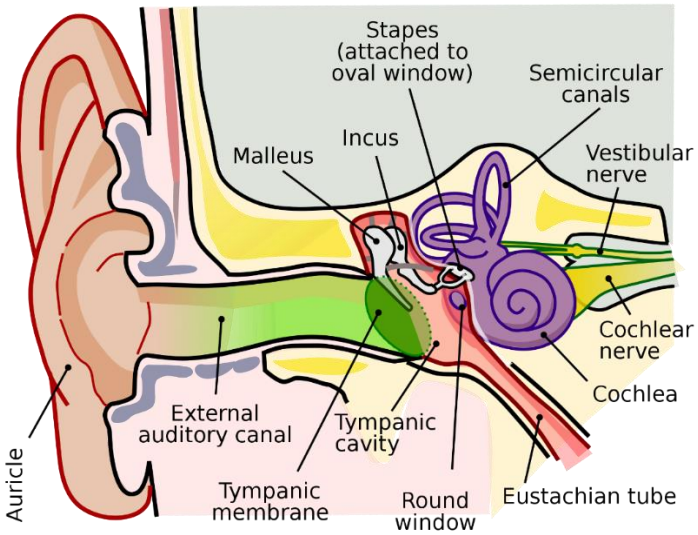

Figure 1.2. Ear and its components [5]

When sound comes to the external ear, sound waves are collected by the pinna and transferred to the tympanic membrane via the ear canal. At the tympanic membrane, acoustic vibration turns into mechanical vibration. The vibration of the tympanic membrane transmits to the malleus via the manubrium which is the part where the malleus and tympanic membrane connects each other. After the malleus, mechanical vibration transferred to firstly incus and then stapes. Ossicle chains behave like a lever mechanism; thus, input vibration is transferred to the inner ear by amplifying. The fluid within the inner ear cochlea, named perilymph, is moved by the vibration of the stapes. A layer of tiny hair cells covers the bottom layer of the cochlea, each of which is triggered by certain frequencies of sound waves. They convey information to the brain via the auditory nerve after being triggered by the movement of the perilymph fluid, which is perceived as sound in the brain. All of the preceding phases are essential to the hearing process. Damage or a deficiency in any of these structures might result in hearing loss as a result of this interaction.

1.2 Hearing Disorders and Treatments

Hearing loss is a deficiency in the auditory system, and it can be explained as a rise in the threshold of sound perception level. It can be examined under four main categories as follows:

- Sensorineural hearing loss
- Conductive hearing loss
- Mixed hearing loss (both sensorineural and hearing loss)
- Central hearing loss

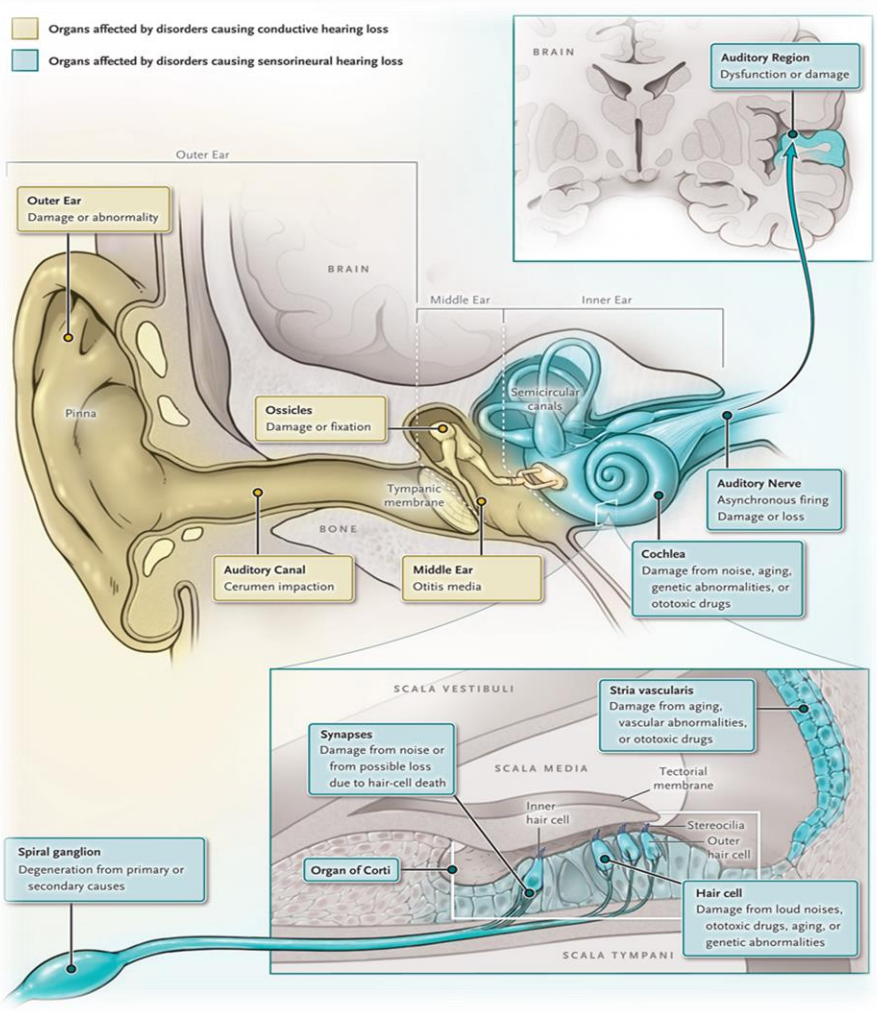

Figure 1.3. Organs which are affected by the sensorineural and conductive hearing loss [6]

The most common hearing loss types are a sensorineural and conductive hearing loss. In the sensorineural hearing loss, cochlear sensory epithelium or peripheral auditory neurons are damaged. According to the damage, whether it is due to cochlear sensory epithelium or peripheral auditory neurons, different difficulties occur. In the first case, hearing loss shows itself as a shift in sound threshold; on the other hand, in the second case in which peripheral auditory neurons are damaged, considerable sound distortion frequently shows up as word discrimination issues [7]. In the conductive hearing loss, there is corruption in transmitting sound waves from the air to the inner ear. Dysfunction at the level of the external auditory canal,

tympanic membrane, or ossicular chain is the root cause of the problem, which results in ineffective sound wave conversion from the air to the liquid medium of the membranous-labyrinth endolymph [7]. In Figure 1.3, organs that are affected during a sensorineural and conductive hearing loss are presented. It can be seen also from Figure 1.3 that in conductive hearing loss mostly outer and middle ear components are affected, whereas, in sensorineural hearing loss, affected components are parts of the inner ear. Mixed hearing loss is the combined version of the sensorineural and conductive hearing loss in which outer, middle and inner ear organs are affected. The last type of hearing loss is central hearing loss. A lesion in the auditory brain or central auditory pathway leads to central hearing loss. Ossicles and cochlear hair cells amplified and processed sounds by the auditory cortex. Aphasia, pure word deafness, auditory agnosia, cortical deafness, and auditory hallucinations are examples of central hearing loss. Presbycusis, or age-related hearing loss, is connected to a different more prevalent type of central hearing loss. Speech distortion in the elderly is frequently worse than would be estimated depending on their pure-tone hearing thresholds. This is thought to be caused by a variety of aging-related alterations in central auditory processing, loss of cochlear hair cells, and neuronal loss [7].

Any impairment to the peripheral or central auditory systems might result in hearing loss. Degenerative aging processes, genetic anomalies, noise-induced hearing loss, taking therapeutic medications with autoimmune adverse reactions, and chronic illnesses are the main causes of sensorineural hearing loss.

The effects of aging on the auditory system are the main cause of hearing loss that first appears in adults. Although, aging has a significant effect on adult hearing loss, exposing excessive noise and some drugs have also an adverse effect on the audiological system. In age-based hearing loss, dominant symptoms are hearing loss at high frequencies, above 2kHz, and another significant symptom is a decline in speech comprehension.

Hereditary reasons are one of the other reasons of the hearing loss. It is known that mutations in more than 100 genes can cause hearing loss [6]. Age-based or gradual deafness that is transmitted as an autosomal dominant trait is linked to mutations in about 30 of these genes [8].

Excessive noise exposure is another reason of the hearing loss. A ubiquitous part of modern life is excessive noise levels that are exposed during daily life events such as concerts, theatres, or due to power tools. Due to excessive noise exposure, sound pressure creates extreme mechanical stress on the inner ear, and damage to the hair cells can occur. This type of damage can be permanent or temporary according to the intensity.

Chemicals and drugs can be resulted in damage to the auditory system, especially in long-term usage. Nearly 20% of individuals using aminoglycosides experience hearing loss [9], [10]. In addition to this, patients with cystic fibrosis, who frequently receive aminoglycoside therapy, have a higher prevalence of hearing loss up to 56% [11], [12]. About 60% of individuals with testicular cancer and 65% of patients with head and neck cancer who have received cisplatin as an adult had clinically significant hearing loss [13], [14].

Other factors that can be resulted with or have an effect on hearing loss can be smoking, obesity, cardiovascular problems, and diabetes. Also, some rheumatological and immune diseases may have an adverse effect on the auditory system, such as rheumatoid arthritis and systematic lupus erythematosus [15].

Although age-related hearing loss is still difficult to prevent, certain lifestyle changes, attention to noise levels, and regular health check-ups can help reduce the amount of loss. Hearing aids can be used for curing conductive hearing loss and some minor sensorineural loss. Three elements are involved in a hearing aid: a microphone, an amplifier, and a speaker. A microphone in the hearing aid picks up sound, transforms it into electrical impulses, and then transmits those signals to an amplifier. The signals are given more strength by the amplifier before being transmitted to the ear via a speaker. Sound waves amplified by hearing aids are

transmitted to healthy hair cells and converted into neural signals that stimulate the brain through hair cells. In Figure 1.4, types of hearing aids are presented. The amplification required by the hearing aid varies according to the damage to the hair cells; therefore, hearing aids may not be suitable for severe hearing loss.

Figure 1.4. Types of hearing aids [16]

At the point where severe or total hearing loss is observed, hearing aids cannot provide healthy hearing. Cochlear implants are used in which are placed into the middle ear and electrically stimulate the auditory nerve without passing through the cochlear hair cells, enable partial hearing restoration for such situations that hearing aids are insufficient [17]-[19]. These devices have also been shown to enhance speech perception, occupational, social, and psychological functioning, and quality of life [20].

1.3 FICI Concept and Its Applications

Cochlear implant is used where hearing aids are insufficient to help hearing problems. It is a small, compact electronic device, and it is composed of four components which are microphone for collecting the sound, a speech processor for organizing captured sounds, a transmitter and stimulator for transmitting signals which come from the processor and turning them into electrical signals respectively, and an electrode array for stimulating the various regions of auditory nerves [21]. An

illustration of the conventional cochlear implant together with all of its components in ear is presented in Figure 1.5.

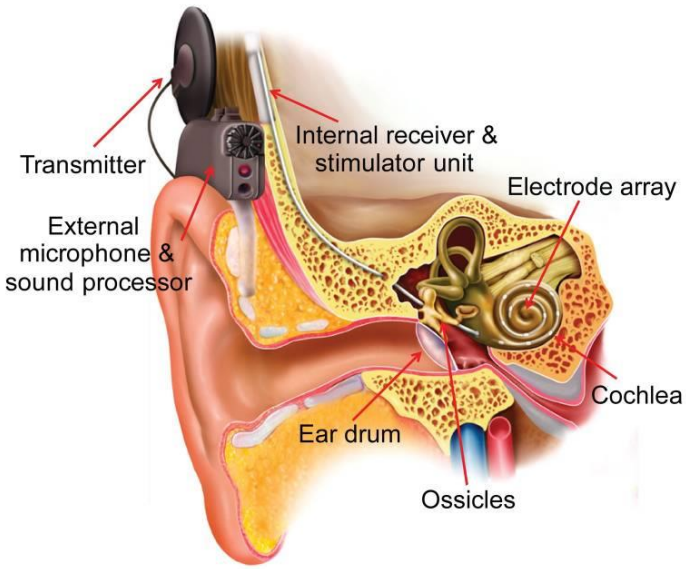

Figure 1.5. Representative image of cochlear implant [23]

A general working principle of the cochlear implant is different than hearing aids. Hearing aids magnify sounds so that ears with hearing loss can hear them. Avoiding damaged ear tissue, cochlear implants stimulate the auditory nerve directly. The auditory nerve transmits impulses produced by the implant to the brain, which interprets them as sound. It takes some time to retrain one's ears to hear with a cochlear implant because it differs from regular hearing [21].

Conventional cochlear implants (CI) have both advantages and disadvantages which can be lined up as follows respectively. First of all, CI helps to hear nearly normal levels and it increases speech perception. Cochlear implants may also help by providing control over one’s voice which could improve communication for people with hearing problems. Main disadvantages of the cochlear implant are complications that can be occur during the surgery. However, this problem is one of the possible disadvantages of all procedures that require surgical operation. Other disadvantages of the cochlear implants are their external components which are not enduring to the water. MRI compatibility, recharging of the battery, high cost and

aesthetic concerns due to the external parts are also discomfortable issues about the cochlear implants.

Above explained problems can be overcomed with fully implantable cochlear implant (FICI) concept. In FICI concept, there is no need for external components. An implantable acoustic sensor, low power stimulation circuits, and an implantable battery are the key elements of the FICI concept.

Although, there are some commercial fully implantable implants are present such as Cochlear Carina and Envoy Esteem, still they have some problems such as the ossicular chain has to be interrupted; long duration of surgery, the battery charging times and impaired MRI examinations [22]. In Table 1.1, according to the working principle, whether piezoelectric or electromagnetic principles and according to the visibility cochlear implants can be presented in a classified way.

Table 1.1 Commercial middle ear implants according to the working principle and visibility [22]

Type	***Fully Implantable***	***Partially Implantable***
Piezoelectric	Envoy Esteem	Rion Device
	Implex TICA	
Electromagnetic	Cochlear Carina	Cochlear MET
		Cochlear Codacs
		Ototronix Maxum

Except the commercial products and works of companies, there are ongoing research projects. Yip et. al proposed FICI concept as a system on a chip sense [23]. In their model, there is a piezoelectric sensor coupled to the system-on-chip (SoC), and sensing is accomplished with this piezoelectric sensor placed into the umbo in the middle ear. To reduce implant size and provide proof-of-concept for a FICI, the SoC incorporates an implantable acoustic sensor front-end, sound processor, and brain stimulator on one chip [23]. In Figure 1.6, overall concepts block diagram and effective frequency response of the designed filter bank for 4, 6 and 8 channel are presented.

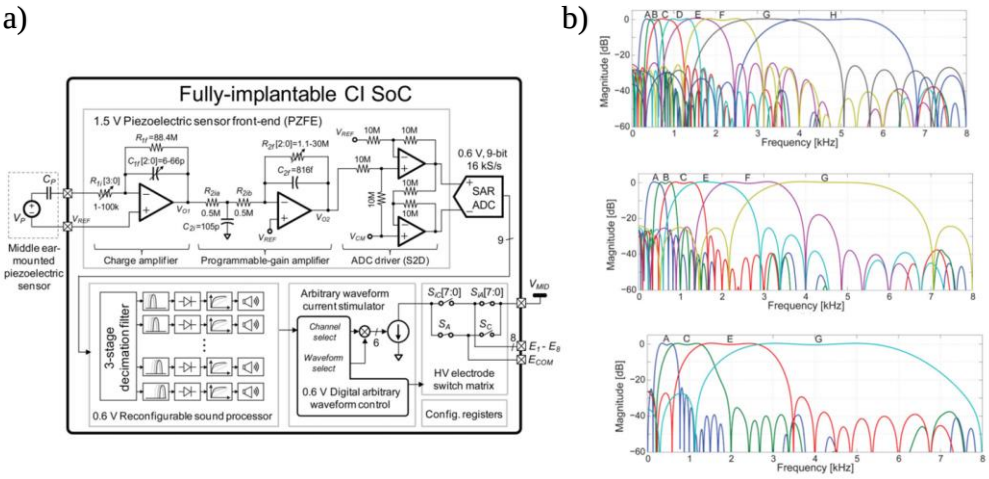

Figure 1.6. a) Block diagram of the SoC concept [23] b) Frequency response of the filter bank for 4-channel; 6-channel; 8-channel from top to bottom [23]

Although, there are not many MEMS-based applications of FICI concept, there is ongoing research about possible solutions of hearing impairments. Svatos et. al (2015) [24] proposed an array of MEMS-based piezoresistive diaphragms for cochlea whose resonances can be tuned to cover audible frequency range. Heredia et. al (2012) [25] proposed a thin film of SiGe as a diaphragm which is used for acoustic sensing implications. Schematics and SEM image of their designed diaphragm are presented in Figure 1.7. Based on the resistance change of the piezoresistive membrane sensing of the incoming sound is conducted.

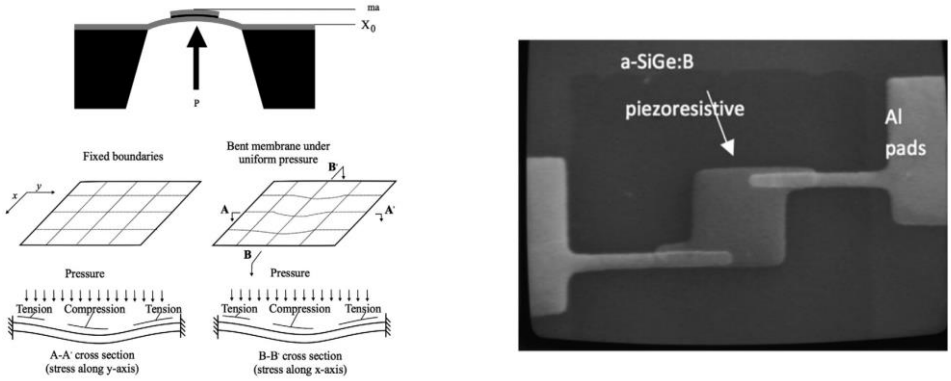

Figure 1.7. Left: Schematics of MEMS-based diaphragm for acoustic vibration sensing Right: SEM image of the diaphragm [25]

Jang et. al [26] developed an artificial basilar membrane and conducted its in-vivo experiments. Their design is composed of an array of piezoelectric cantilevers that mimic a basilar membrane's characteristics; each cantilever length is arranged to filter the incoming frequency. In Figure 1.8, proposed device, frequency domain and time domain responses, each channels deviation around resonance, deflection of the cantilever under resonance is presented. Based on the presented graphs at the figure, it can be said that general response under acoustic input is well and overall deviation margin of the cantilevers from expected resonance is small. They also examined the evoked auditory brain responses of the deafened guinea pigs. Therefore, it can be said that although there are some deficiencies in terms of fulfilling the functions of the healthy ear, it is a promising study.

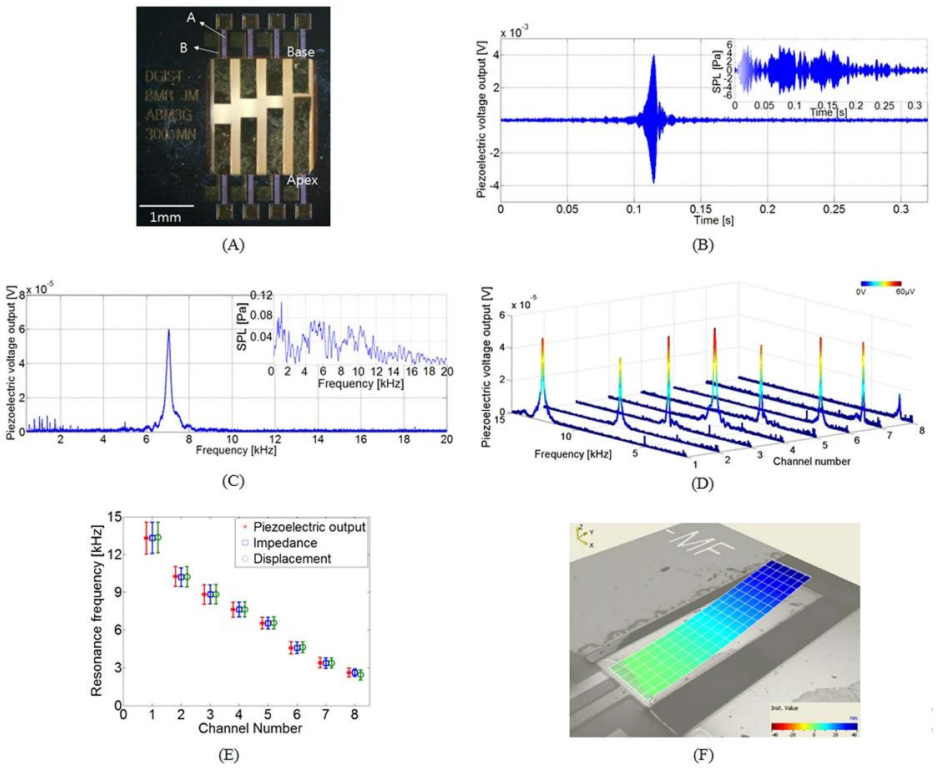

Figure 1.8. a) Image of the piezoelectric basilar membrane b) Response of the fourth channel in terms of voltage with respect to time c) FRF response of the fourth channel d) Overall FRF response of the device e) Mean resonance values and their deviations according to channels f) Deflection of the cantilever at its resonance [26]

1.4 Aim of the Research and Organization of the Thesis

FLAMENCO project is the development of a fully implantable MEMS-based autonomous cochlear implant. In Figure 1.9, illustration of the overall concept of the FLAMENCO is presented. Concept is based on eliminating the problems of conventional cochlear implants. First of all, most of the conventional cochlear implants have a limited battery life, thus, they require re-charging which is again decreases the life standard of the patient. Secondly, they have external parts which can harm under water which makes life with them unpleasant and difficult; lastly, those external parts can bring some aesthetic concerns, especially among younger patients. FLAMENCO project proposes a fully implantable cochlear implant that has no external units, and thanks to its low-power interface electronics and harvester unit, it does not require any charging.

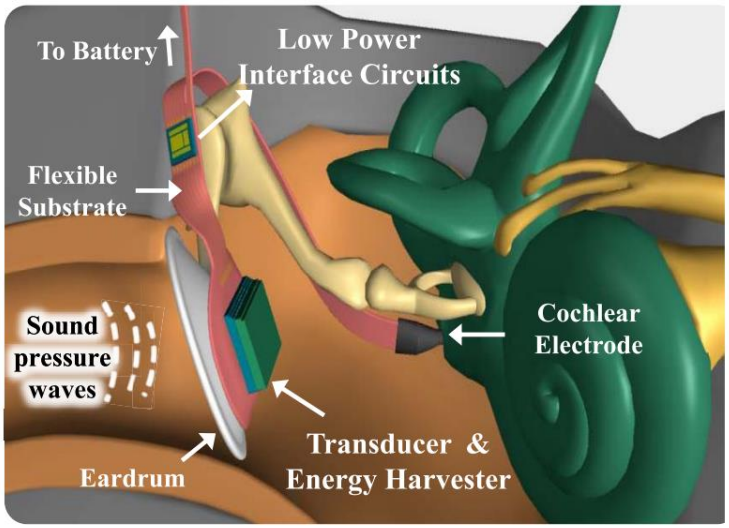

Figure 1.9. Illustration of the FLAMENCO Project [27]

It is a novel approach as a solution to the problems of conventional cochlear implants in which the following milestones are aimed:

- MEMS-based piezoelectric sensor is designed in order to mimics the sensing characteristics of a healthy ear.

- An interface circuit that will process the sensor output and convert it into stimulation pulses is designed.
- Piezoelectric energy harvesting system is proposed in order to eliminate the need for regular battery charge of the conventional cochlear implants.

In scope of above explained objectives, thin film multi-channel piezoelectric sensor is proposed and studied by Yuksel et.al [27], [28] and Ilik et.al [29] in our research group. Interface circuit and MEMS-based piezoelectric harvester studies are conducted by Ulusan et.al [30] and Koyuncuoglu et.al [31] respectively.

In this thesis, a new and novel approach to the piezoelectric sensor is studied. Thanks to previous studies, microfabrication is optimized and, multi-channel regular cantilevers' performance under some dimension constraints is examined. However, the desired frequency range which is decided as 300Hz and 6 kHz cannot be fully covered. Hence, the aim of this thesis is to improve the performance of the piezoelectric sensor with a novel approach. In addition to this, although, the previously mounting location for the sensor is decided as a tympanic membrane, after discussion with ENT surgeons it is decided that the tympanic membrane may not be the most suitable location due to the difficulty of surgical operations and also the regeneration of the tissue above membrane which may result with in tissue growth above the sensor. Therefore, middle ear vibration characteristics are also examined for possible coupling locations together with the design and examination of possible coupler mechanisms under the scope of this thesis.

Within the scope of this research, the structure of the thesis is formed as follows:

1. Middle ear vibration characteristics and attachment mechanisms are examined.
   - Simplified finite element model of the middle ear is constructed.
   - Based on the literature, constructed FEM model, and guidance of the surgeons, possible locations for the sensor are decided.

- ❖ Possible attachment mechanisms according to the overall volume and geometry of the location, and the dimension of the sensor is designed.
- ❖ FEM simulations for stress distributions and life calculations under impact forces are done for the attachment mechanism.
- ❖ Experimental verification of the attachment mechanism is done.

2. Design of the piezoelectric sensor is conducted.
   - ❖ Overall constraints and requirements are determined.
   - ❖ Material selection and properties are defined.
   - ❖ Different geometrical structures are examined for broadening the covered frequency range.
   - ❖ FEM simulations are conducted in order to arrange the frequencies and observe the frequency domain responses.
   - ❖ Optimization of the designs is performed.
3. Microfabrication of the piezoelectric sensor is conducted.
4. Experimental verification of the sensor is done.
5. Finally, alternative design possibilities for broadening the bandwidth are presented.
   - ❖ Under constraints and requirements different geometrical configurations are done.
   - ❖ FEM simulations of the designs are conducted.
   - ❖ Optimization of the designs is done.
   - ❖ Microfabrication of the alternative sensor possibilities is conducted.
   - ❖ Experimental verifications are done.

In this chapter, a general overview of cochlear implants, hearing loss, and the FICI concept is presented. FLAMENCO project is explained together with its aim and successions until now. After explaining the overall concept of the research, the scope of the thesis is explained together with a high-level list of studies conducted throughout the study.

CHAPTER 2

Middle Ear FEM Modelling and Attachment System Design for Piezoelectric Sensor

In this chapter, simplified middle ear FEM modeling is conducted and possible attachment systems for middle ear implant is modeled and examined. Firstly, membrane and ossicles modeling is conducted, and based on the initial created model, parameters are tuned in order to obtain the suitable vibration characteristics of the middle ear. Secondly, possible locations and coupling mechanisms for the sensor are examined. Then, material selections and possible coupler designs together with FEM simulations are conducted. Finally, the attachment mechanism design is verified experimentally.

2.1 Middle Ear FEM Modelling

2.1.1 Modeling of Tympanic Membrane and Ossicles

The tympanic membrane is the entrance part of the middle ear and it has crucial importance on the vibration characteristics of the ear. Its physical characteristics can change from person to person, but general physical dimensions lie in a range. Although even those small deviations have an importance, until it does not deviate too much general characteristic of it is preserved.

The tympanic membrane is modeled according to the given dimensions from [32]. The layout of the model is presented in Figure 2.1. While tympanic membrane is modeled four main categories are considered which are pars tensa, pars flaciada, malleus attachment on the eardrum and tympanic annulus.

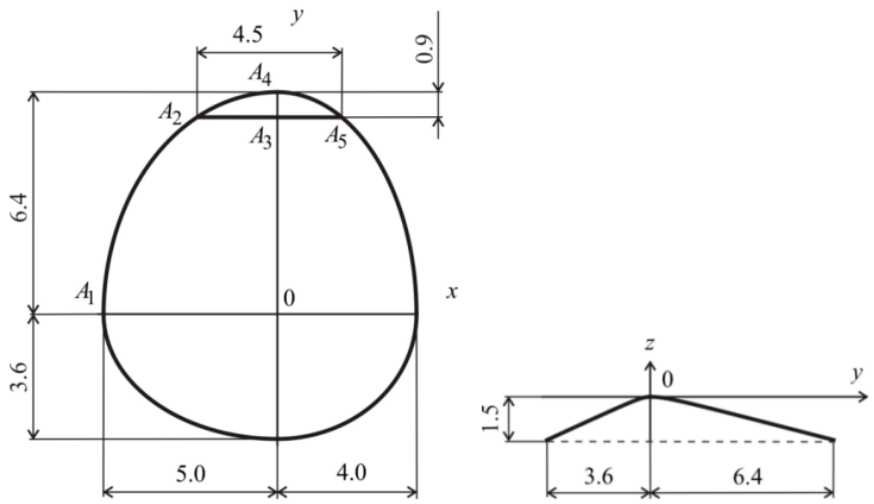

Figure 2.1. Layout of the tympanic membrane [32]

In Figure 2.2, the assembly of the ear together with the ear canal, ossicles and tympanic membrane are presented. Ossicles are meshed CAD files from an open source with an approximate scale of 10:1. They are divided into different bodies and their sizes are arranged according to the average dimensions of the ossicles; dimensions of the ossicles are presented in Table 2.1.

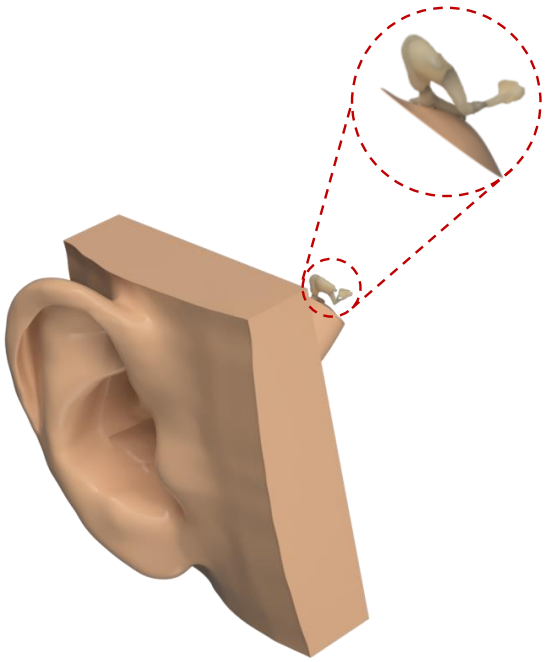

Figure 2.2. Middle Ear Model

Table 2.1 Dimensions of the Ossicles

	Parameters	Model mm	Unur et. al [33] mm	Wadha et. al [34] mm	Harneja and Chaturvedi [35] mm	Arensburg et al [36] mm
STAPES	Total height	3.43	3.22± 0.31	3.41± 0.20	3.12 ± 0.21	3.20 ± 0.21
	Length of basis stapedis	2.65	2.57± 0.33	2.97± 0.31	2.68 ± 0.27	2.8 ± 0.15
	Width of basis stapedis	1.36	1.29± 0.22	0.39± 0.10	1.26 ± 0.08	1.3 ± 0.07
INCUS	Total length	5.45	6.47± 0.55	-	3.14 ± 0.19	6.4 ± 0.24
	Total width	4.36	4.88± 0.47	-	1.82 ± 0.14	
MALLEUS	Total length	7.15	7.69± 0.60	-	7.15 ± 0.31	7.8 ± 0.35
	Length of manubrium	4	4.70± 0.45	-	4.22 ± 0.35	4.4 ± 0.47
	Length of head and neck	4.14	4.85± 0.29	-	-	-

2.1.2 FEM Model

Discrete mass-spring-damper system can be used for modeling of auditory system which is presented in Figure 2.3. In this modeling, each part of the ear is represented as a mass-spring-damper and under an external force, whether acoustic force or mechanical force due to start point of the modeling, hearing can be modeled. In Figure 2.3a and Figure 2.3b, two models are presented according to the type of viscoelasticity whether Maxwell viscoelastic model or Kelvin-Voigt model is preferred respectively. Zener model uses a linear combination of springs and dampers to represent the elastic and viscous components of a viscoelastic material. Maxwell model and Kelvin-Voigt model are sub-models of Zener model in which the Maxwell model does not account for creep or recovery, and the Kelvin-Voigt model does not account for stress relaxation.

a)

b)

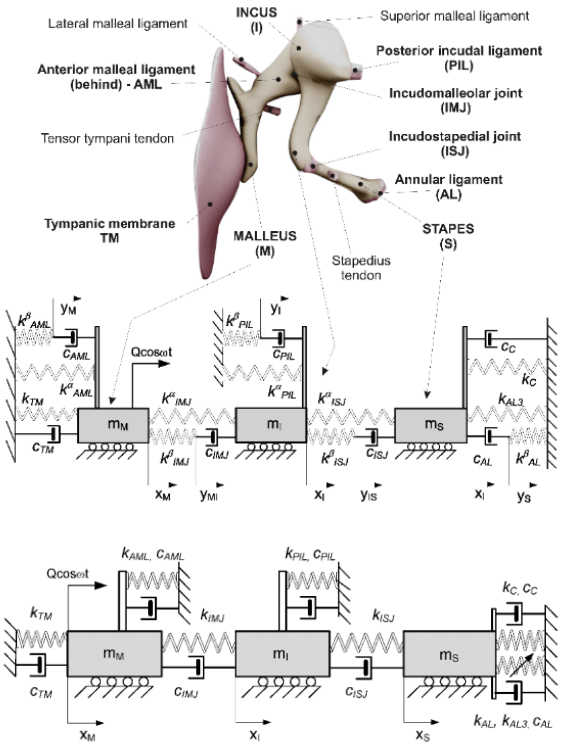

Figure 2.3. a) Mass-spring-damper model of the auditory system based on Maxwell representation b) Mass-spring-damper model of the auditory system based on Kelvin-Voigt representation [37]

In this 3D-FEM modeling, Rayleigh damping model is preferred in a more simplified manner. Equation of motion for the model can be presented with mass-spring-damper matrices which are expressed in equation (1). For Rayeigh damping, classical viscous Rayleigh damping model is preferred which is expressed in equation (2). The multiplier coefficients of mass and stiffness matrices, α and β, are mass and stiffness proportionality constants respectively.

$$m\ddot{x} + c\dot{x} + kx = f(t) \qquad (1)$$

$$\alpha[M] + \beta[K] = [C] \qquad (2)$$

For 3D-FEM modeling of the middle ear, used material properties in the ANSYS are presented in Table 2.2. All of the parts are modeled with Rayleigh damping of α=0 and β=1e-4, except malleus and tympanic membrane. For malleus, damping is

assumed as zero. For tympanic membrane, α is taken as 260 s^{-1} except malleus attachment on the eardrum section [39]. Moreover, the poisons ratio is taken as 0.3 for all parts. With Young's modulus of 14.1 GPa, three ossicles (malleus, incus, and stapes) were modeled as linear elastic, isotropic, and homogeneous. Table 2.2 shows the varied mass densities in different parts of the ossicles. The part where malleus and tympanic membrane is connected was modeled as softer than the ossicles with one third of the Youngs modulus of ossicles. This softer connection is because of the loose attachment between manubrium and membrane [40]. In Figure 2.4, FEM model of the middle ear is presented together with its connections.

Table 2.2 Material Properties of The Middle Ear [38]

	Density (kg/m^3)	**Youngs Modulus (Pa)**
Pars Tensa	1200	2e7(circumferential); 3.2(radial)
Pars Flaciada	1200	1e7(circumferential); 1e7(radial)
Malleus Attachment on Membrane	1000	4.7e9
Malleus Head	2550	1.41e10
Malleus Neck	4530	1.41e10
Malleus Handle	3700	1.41e10
Incus SP	2260	1.41e10
Incus LP	5080	1.41e10
Incus Body	2360	1.41e10
Incudomalleolar Joint	3200	1.41e10
Incudostapedial Joint	1200	6e5
Stapes	2200	1.41e10

According to the studies of Vlaming et. al [41], Incudomalleolar joint, which is the main connection between malleus and incus, has more rigid behaviour at frequencies lower than 3 kHz. Thus, it is modelled with same Youngs modulus of ossicles as homogenous and isotropic material.

According to the research of Cheng et. al [42], incudostapedial joint, which is the main connection between incus and stapes, has some mobility in order to prevent the loud noise and a rapid pressure change in the inner ear.

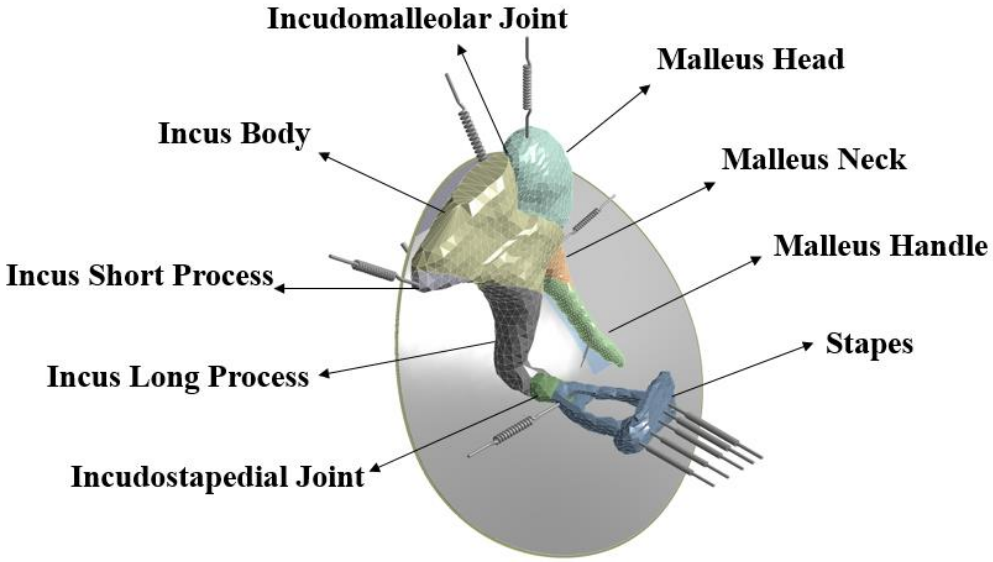

Figure 2.4. Model of middle ear together with the connections

2.1.2.1 Boundary Conditions

In modeling, ligaments and tendons are taken as boundary conditions Each ligament and tendon, which are lateral malleolar ligament (LML), anterior malleolar ligament (AML), posterior incudal ligament (PIL), tensor tympani tendon (TT), stapedial tendon (ST), superior malleolar ligament (SML), is assumed behave as 1D spring elements.

Tympanic annulus and stapes footplate are the remaining boundary conditions of the model. Tympanic annulus is assumed as an elastic ring which can only make translational movement in the normal direction of the surface. It is fixed with spring-to-ground connection for representing the connection between the ear canal. In Figure 2.5, boundary condition representation of the tympanic membrane is shown.

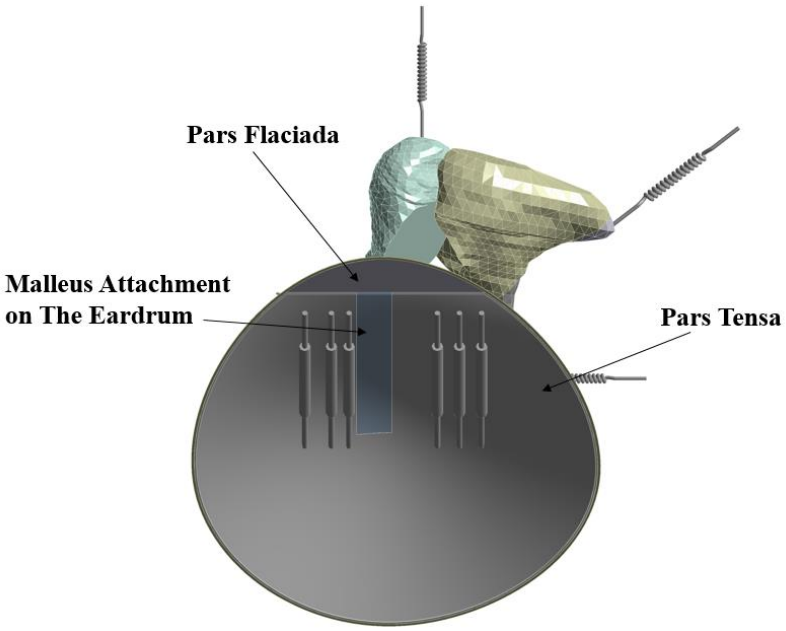

Figure 2.5. Tympanic membrane connections

The other end of the model is the stapes footplate. It transmits vibrations to the cochlea by resonating with the oval window. Sun et. al [38] modeled the cochlear impedance with a set of one-end-fixed springs together with damping. In the current FEM model, this approach has been adopted. In Figure 2.6, ligaments and tendons of the ossicles are presented as spring.

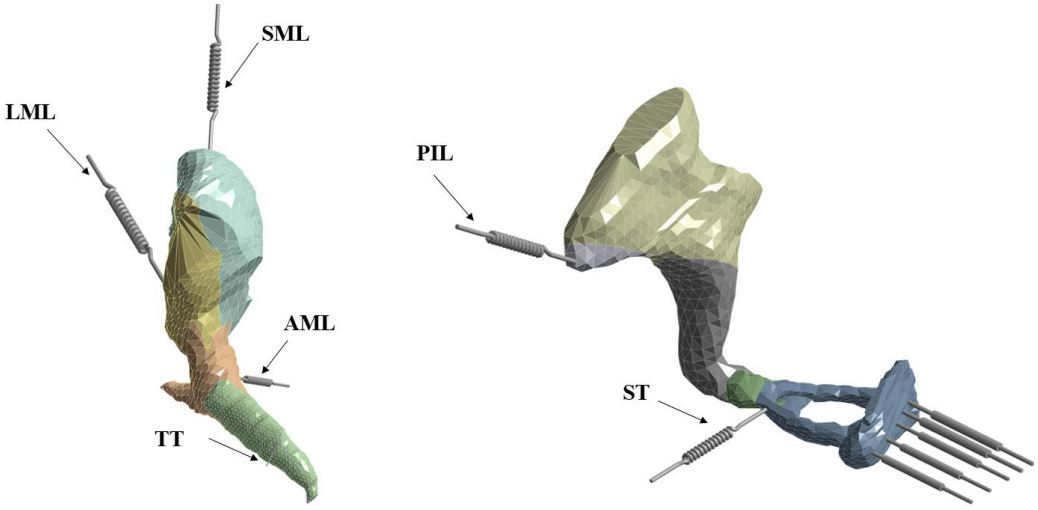

Figure 2.6. Spring representation of ligaments and tendons

2.1.2.2 Modal Analysis and FRF Response of The Middle Ear

The model of the middle ear is meshed with 20016 elements and 53972 nodes, and also face sizing is used for the tympanic membrane. Mesh size and elements are arranged also by considering computational time.

In order to optimize the FEM model according to the experimental data, a cross-calibration process is followed. After all connections were preceded, simulation logic is presented in the Figure 2.7. For experimental data, the response of the umbo and stapes footplate is examined under 80dB SPL. In order to provide the acoustic to structural vibration relation, equation (3) is used. Equation (3) provides the conversion between acoustic sound pressure and root mean square pressure form of sound under reference pressure level of P_0. For the middle ear conditions, reference pressure P_0 is taken as 20 μPa.

$$P_{SPL} = 20 * log_{10}\left(\frac{P}{P_0}\right) \qquad (3)$$

During modelling, two main strategy is followed. In the first one, the analysis is conducted from a prestressed membrane. In this analysis, first, 10 to 12 μm displacement is given to the membrane, then modal and harmonic responses are examined. During this process, spring and damping parameters are tried to be optimized. In the second logic, without any previous static analysis, model is gone under modal and harmonic analysis; then, parameter optimization is conducted. It is seen that for the built FEM model, pre-stress on membrane is resulted with undesired results, mainly due to the not fixed but spring to ground connections at tympanic annulus. Thus, instead of prestressed membrane-based analysis logic, only parameter optimized modal and harmonic analysis are followed.

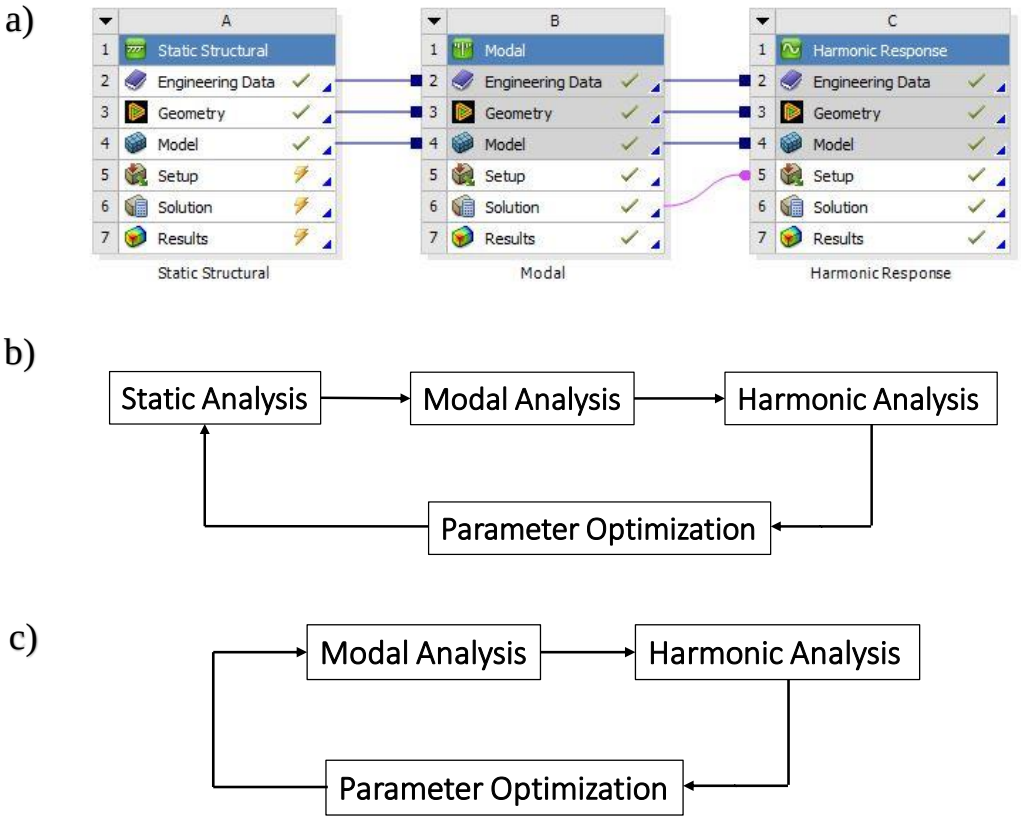

Figure 2.7. a) Interface of the Workbench Module of ANSYS for Executed Logic b) Prestressed Optimization c) Only Parametric Optimization

In modelling of the tympanic membrane, the tympanic annulus, which is taken as a fixed part, is assumed fixed with spring in order to provide the elastic characteristics. Other boundary condition for model is stapes footplate. It is fixed with 5 longitudinal springs. Cochlear fluid impedance of the middle ear is modeled as viscous damping. The stiffness and damping values of the springs are taken as 10 N/m and 0.001 N.m/s. For boundary condition at tympanic annulus, cross calibration is applied. In order to obtain the right characteristics of the middle ear, optimum conditions are found as four longitudinal springs with spring constants of 850 N/m and viscous damping of 0.07 N.m/s; and two torsional spring with spring constants of 0.06 N.m/° and viscous damping of 0.001 N.ms/°. For ligaments and tendons, cross-calibration is done based on the range at the literature [32],[42]-[44], which is presented at the Table 2.3.

Table 2.3 Spring constants k of the ligaments and tendons

Parameter(N/m)	**Range(N/m) [32],[42]-[44]**	**FEM Model(N/m)**
K_{SML}	20-1500	1500
K_{AML}	1300-22000	1500
K_{LML}	20-2000	1000
K_{PIL}	200-20000	600
K_{ST}	42-12000	300
K_{TT}	364-79000	2000

2.1.2.3 Experimental and FEM Results Comparison

After modeling, harmonic analysis is conducted under 0.2 Pa, which is pressure equivalent of SPL of 80dB under reference pressure of P_0, 20 μPa. Experimental data for the umbo and stapes footplate is compared with the FEM model.

The validity of the FEM model is confirmed by fitting of the results to the experimental data from literature (Nishihara (1996) [45], Hato (2003) [46], Nishihara (1993) [47], Young (2010) [48] and Zhang (2014) [49]) for umbo at 80 dB SPL in Figure 2.8.Obtained results are close to the lower bound of Nishihara et.al [45] with a small discrepancy at high frequencies.

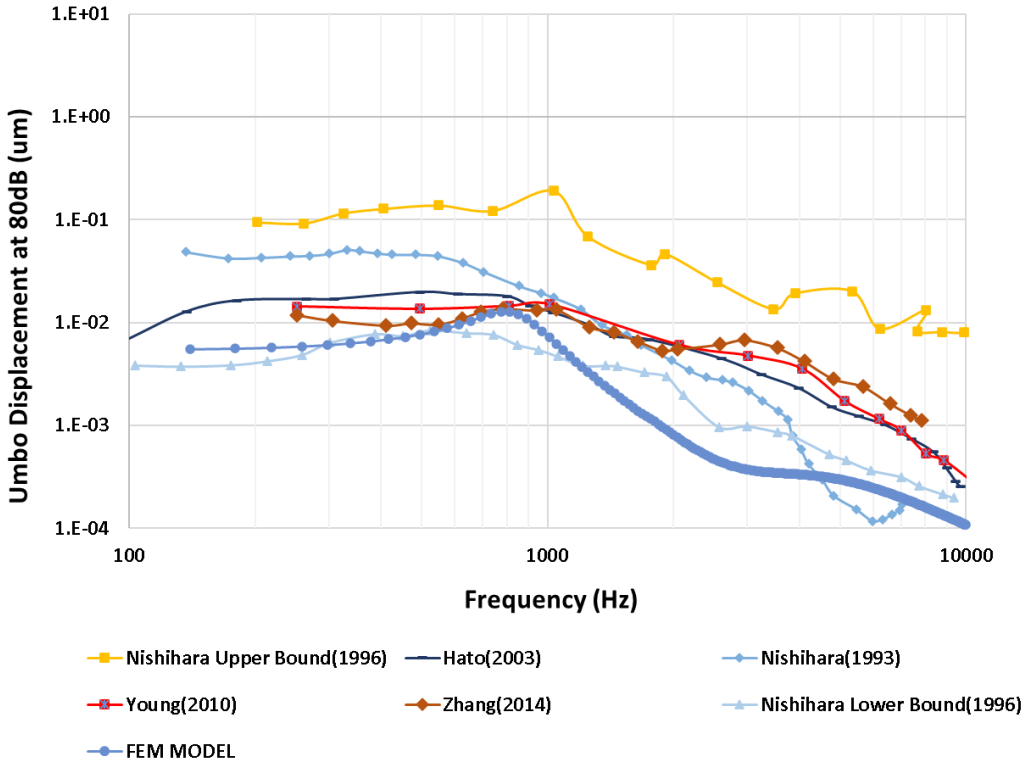

Figure 2.8. Umbo Displacement for 80dB. Comparison with experimental data of Nishihara (1996) [45], Hato (2003) [46], Nishihara (1993) [47], Young (2010) [48] and Zhang (2014) [49]

The other confirmation of the FEM model is conducted from displacement data of the stapes footplate. In Figure 2.9, experimental stapes footplate data from literature (Nishihara (1993) [47], Ferris (2000) [39], Chien (2009) [50] and Hato (2003) [46]) is presented together with data of the FEM model. Results obtained from FEM model shows the same motion characteristics with Nishihara et. al [47] and Hato et. al [46], and shows very close amplitudes to the experimental data of Chien et.al [50]. Chien et. al [50] and Ferris et. al [39] data show a little different characteristics than other two experimental data. In their results, relatively sharper peaks are observed.

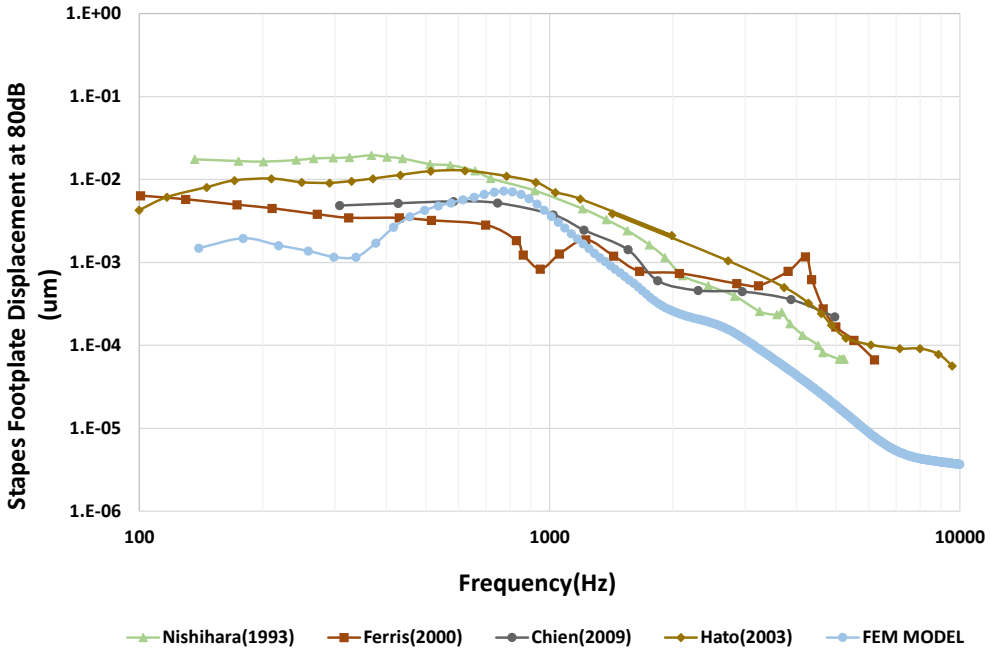

Figure 2.9. Stapes Footplate Displacement for 80dB. Comparison of experimental data of Nishihara (1993) [47], Ferris (2000) [39], Chien (2009) [50] and Hato (2003) [46]

2.2 Attachment System Design and FEM Analysis

After modeling the middle ear, possible attachment system mechanisms for middle ear are examined for connection between ossicles and piezoelectric sensor. Middle ear implants are crucial devices which are used for auditory rehabilitation. Together with the advancements in technology, fully implantable MEMS-based devices are developed. Those devices are advantageous in terms of both health aspects and cosmetic aspects.

A common characteristic of all hearing implants is that the transducer is coupled to the ossicular chain or directly to the inner ear fluid. Consequently, implantable transducers have to fulfill specific mechanical, biological, and surgical requirements. According to the position of the coupling, results will differ. The displacement and force characteristic of each point in the ossicular chain is different. Therefore,

different dynamic characteristics can be observed depending on transducer's coupling location. Many devices are rigidly supported with one end attached to a bony structure such as cranium, tympanic cavity wall, ear canal wall. The other end is attached to the ossicular chain or the inner ear fluid. There is an exception to this situation, which is a free-floating actuator, Vibrant Sound bridge Floating Mass Transducer (FMT) [51]. It is only coupled to the ossicular chain. The coupling point at the ossicular chain influences the transducer performance because of differences in load impedance.

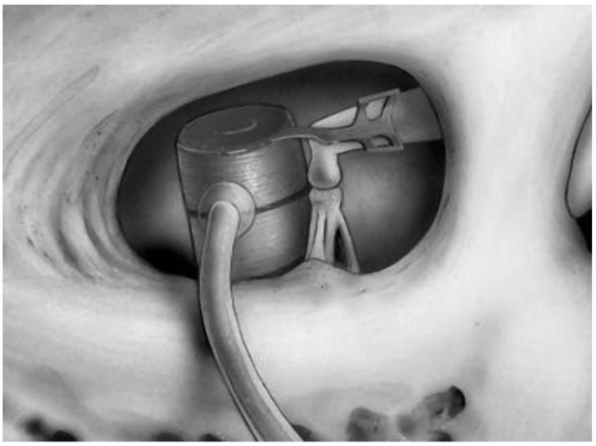

Figure 2.10. FMT on the long process of the incus [51]

To sum up, possible locations, materials, and designs for the middle ear coupler are examined in this part. According to the decided criteria and selections, finalized design options are presented.

2.2.1 Design and Modelling

In order to optimize the input vibration to the transducer without spoiling the overall mechanical characteristics of the middle ear too much, the design of the attachment system has crucial importance. The main criterion for this attachment system is as follows:

- Biocompatibility
- Low mass in order to pevent mass loading effects

- High resonance frequency in order to prevent any mechanical filtering
- High strength

2.2.1.1 Material Selection

Material selection is a crucial part of each design in which there is an interaction between the living tissue and the design. Biocompatibility is defined as the absence of unfavorable tissue responses caused by the materials i.e., it is the capacity of the material to function with an adequate host reaction in a given application [52].

For this coupler design, chosen biocompatible material should have high strength for both impact and cycling loadings. Under these circumstances selected material groups are as follows:

- Nitinol
- PTFE
- Titanium and its alloys

2.2.1.1.1 Nitinol

Nitinol is a nickel-titanium shape memory alloy in which the two elements are almost identical in atomic ratio. Nickel titanium Naval Ordnance Laboratory, where this alloy was developed, is the origin of the name. Nitinol has superior properties; the main two are super elasticity and shape memory effect. It has superior strength besides its relatively lower elastic modulus. It is also bio-inert material which means it does not react with the body and also, it is not damaged by inflammatory processes. It is only coated by a thin layer of mucous membrane. In addition to these, it has high fatigue resistance and MRI compatibility. Nitinol is a special material that can return to its original crystal structure when the applied external load is removed. This feature is named as “super elastic behavior”.

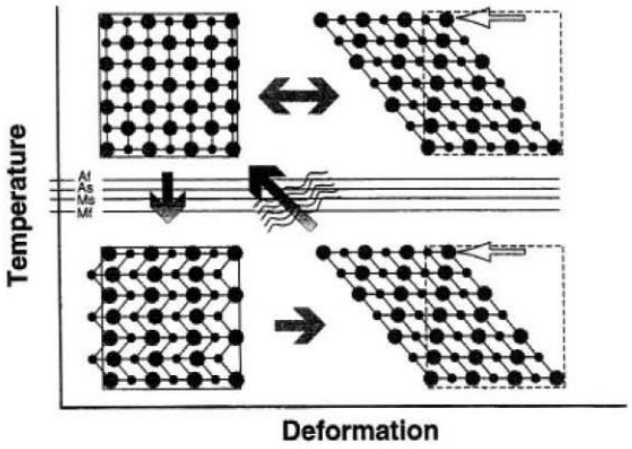

Figure 2.11. Schematic representation of the shape memory effect and super elasticity [53]

The second main behavior of shape memory alloys is after a specific heat treatment process, they can remember the training shape. The effect of heating a plastically distorted sample back to its original shape is known as "Shape Memory." The "thermoelastic martensitic transition" is a crystalline phase shift that causes this phenomenon. Shape memory alloys are martensitic at temperatures below the transformation point, and their microstructure is characterized by "self-accommodating twins" in this state. Because martensite is soft, it is easily distorted by de-twinning. Heating the material over its transition temperature restores its original shape and changes it to its high-strength austenitic state [53].

Nitinol has excellent qualities that make it a viable choice for coupler material, but it also has some significant drawbacks in terms of safety and its ease of use in surgical procedures. In order to provide the crimping of the nitinol coupler, heat should be used to activate the shape memory effect. The placement of the coupler is done in a really small volume. This surgery is risky and might not be appropriate for every patient or every surgeon to do such an operation, especially given that such a volume contains highly sensitive tissues.

2.2.1.1.2 PTFE

Polytetrafluoroethylene in short PTFE is the most popular polymeric biocompatible material. It shows hydrophobic features; and, it also has low surface energy [54]. It has lower elastic modulus, yield strength, and density. It is a bio-tolerant material which is first perceived as foreign compounds by the body; nevertheless, a robust capsule forms shortly after, to which indigenous proteins adhere, concealing the implant from the immune system.

PTFE has the lowest density, lowest elastic modulus, and lowest yield strength compared to nitinol and titanium compounds. Although lower density is desired in terms of weigh limitation in implants; its low strength does make it not preferable. There are multiple reasons behind it. First of all, when coupler possibilities from PTFE is examined, overall stiffness is also too low; thus, it results with lower resonance frequency which is not desired due to mechanical filtering and resonance shifting, especially when it is considered for this research one end of coupler is fixed to the sensor which causes mechanical filtering.

2.2.1.1.3 Titanium and Titanium Alloys

Titanium is an excellent biocompatible, bioinert metal that has a high mechanical strength, very good corrosion resistivity, and comparably lower density. It has a relatively lower elasticity than other metals however it behaves more like a natural joint which results with fewer complications in body.

“Commercially pure titanium” has four grades with different elastic moduli and strength values. Pure titanium shows more flexibility than its alloys which makes it a preferable choice for implants where high strength is not the case.

Titanium can be alloyed in order to enhance or adapt its properties according to the aim. Ti-6Al-4V is the most popular alloy form of titanium. It is also known as Grade 5 titanium. Its composition consists of aluminum and vanadium, with percentages of 6% and 4% respectively.

In Table 2.4 [55], titanium (and titanium alloy) properties according to the elemental compositions are presented. According to Table 1, oxygen is the most significant element in terms of the chemical content of pure titanium. With an increased content of oxygen, there is an increase in tensile strength of the material. For the Grade 5, alloy of titanium, increased strength is due to the aluminum and vanadium.

Table 2.4 Composition and mechanical properties of Ti alloys [55]

	Elements (% max)						**Mechanical Properties**		
Sample Ti Alloy	**C**	**O**	**N**	**H**	**Fe**	**Ti**	**Youngs Modulus (GPa)**	**Yield Strength (MPa)**	**Tensile Strength (MPa)**
Grade 1	0.10	0.18	0.03	0.015	0.20	Balance	103	170	240
Grade 2	0.10	0.25	0.03	0.015	0.30	Balance	103	275	345
Grade 3	0.10	0.35	0.05	0.015	0.30	Balance	103	380	450
Grade 4	0.10	0.40	0.05	0.015	0.50	Balance	104	485	550
Grade 5	0.08	0.13	0.05	0.0125	0.25	Balance	110	795	850

2.2.1.2 Possible Locations for Middle Ear Coupler

In terms of collecting the maximum vibration, which has high importance in terms of actuating the sensor, the location of the coupler is significant. In order to make comments about the best possible location for both coupler and sensor, vibration amplitude data of the middle ear should be examined.

In Figure 2.12b, the vibration amplitudes of tympanic membrane and footplate are given from temporal bone experiments of Gan et.al [57] at 90 dB SPL. In Figure 2.12a, relative amplitudes of ossicles and tympanic membrane with respect to each other are given. From the presented data, in terms of amplitude, the most advantageous place is found as umbo or tympanic membrane, in terms of collecting maximum vibration amplitude. However, gluing the sensor to the umbo is not quite advantageous due to medical issues. First of all, human tissue naturally regenerates

over time; thus, when the sensor is glued to the membrane, the tissue grows over it with time. Tissue regeneration over the sensor could result with deficiency in performance. Secondly, in terms of ease of surgical operation, approaching the membrane is harder than approaching the ossicles. Hence, malleus or incus are better choices than the tympanic membrane.

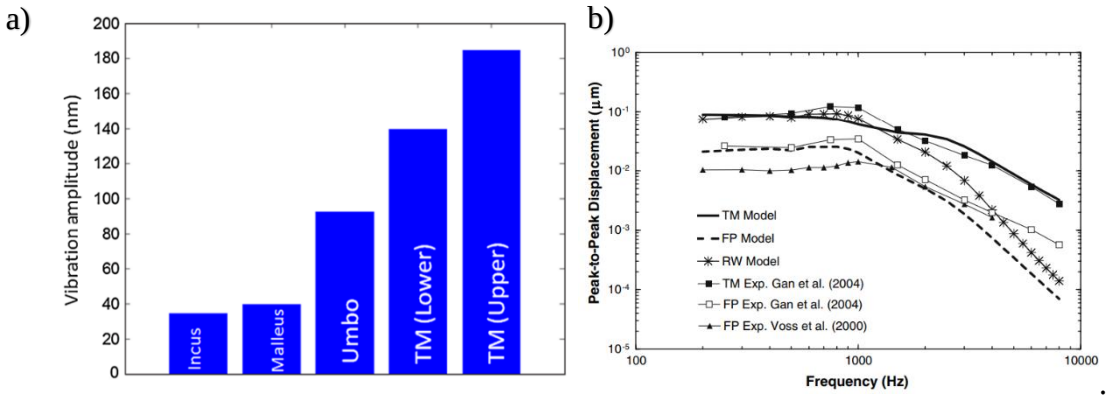

Figure 2.12. a) Relative vibration amplitude plot of different ME structures of a normal human cadaver temporal bone [56] b) Model-derived displacements at the TM, stapes footplate (FP), and round window (RW) in comparison with the experimental data reported by Gan et al. [57] and Voie et al. [58] on human temporal bones. The input sound pressure in the ear canal was 90 dB SPL. [59]

In Figure 2.13, vibration acceleration amplitude in terms of g is presented in a comparative way together before and after incus removal. When the auditory system is considered as discrete mass-spring-damper components, removal of incus means decreasing the overall stiffness of the system. This decrease in the overall stiffness results in the increased vibration amplitude of the umbo. Umbo and malleus vibration are correlated to each other; hence, it can be said that an increased amplitude at the umbo results in increased vibration amplitude of the malleus. Thus, one possibility for the sensor coupler is “malleus bone”. For the case where incus will not be

removed, the possible coupler location is “incus”, which has almost the same vibration amplitude as the malleus.

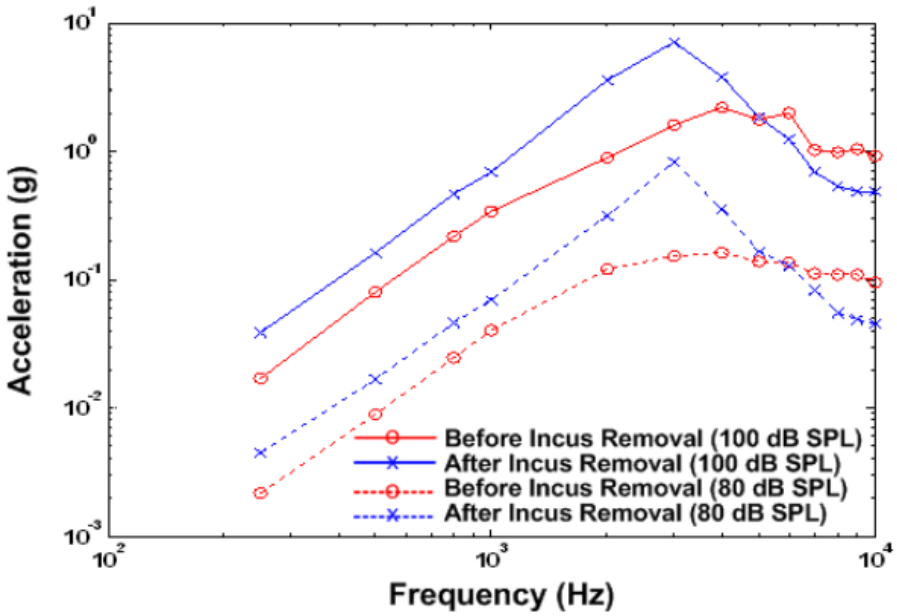

Figure 2.13. Laser Doppler vibrometer measurements of umbo acceleration vs. frequency before and after incus detachment at 80 SPL and 100 SPL [60]

2.2.2 Attachment Design

In previous sections, possible locations, material selections and main requirements for the coupler are discussed. Possible coupler designs are studied by considering the manufacturability and material availability. In this part, these designs will be discussed together with the FEM simulations and analysis.

During the design process, there are main requirements that should be satisfied which can be listed as follows:

- First of all, the resonance frequency of the attachment design, together with the mass of the transducer and interface circuit elements, should be out of the resonance range of the transducer which is decided as 6kHz. Overall mass from the transducer, circuit and other components is estimated as 30mg for

the worst case. Thus, under 30mg resonance of the attachment system should be above 6 kHz.

- Secondly, mass is a serious limitation and consideration for FICI, because it has a direct effect on the amplitude of the vibration. Hence, the attachment system should be light enough not to bring any significant mass to the bone and not disturb the vibrational characteristics of the ossicle chain.
- Thirdly, the design should be durable enough to withstand high impact forces. In
- Table 2.5, g-forces that human body encounter is listed.

Table 2.5.G-force that human being can withstand under different circumstances [61]

Situation	**Amplitude**
Standing on the Earth	1G
Rollercoasters	3.5-6.3G
A slap on the back	4.1G
Formula 1 racing car	5G
The luge at Whistler	5.2G
Sneezing (open mouth)	2.9G

Although, the human body can withstand high g-forces, it is also well-known that most of these impact forces are absorbed well before being transmitted to the viscera. In the research of Wu et.al [62], they reconstructed the skull and made the analysis of energy absorption characteristics of the skull. In Figure 2.14, the reconstructed skull model and its sections presented.

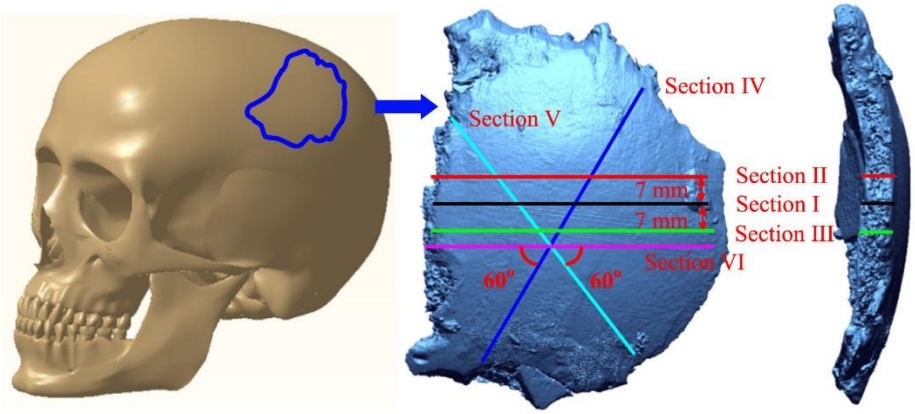

Figure 2.14. Skull Sections [62]

According to the built model under an impact force, energy absorption and impact kinetic energy relation are presented with respect to the impact velocity in Figure 2.15. It can also be seen from the graph that there is a threshold point for skull; up to this point, skull shows excellent absorber and bounder effects.

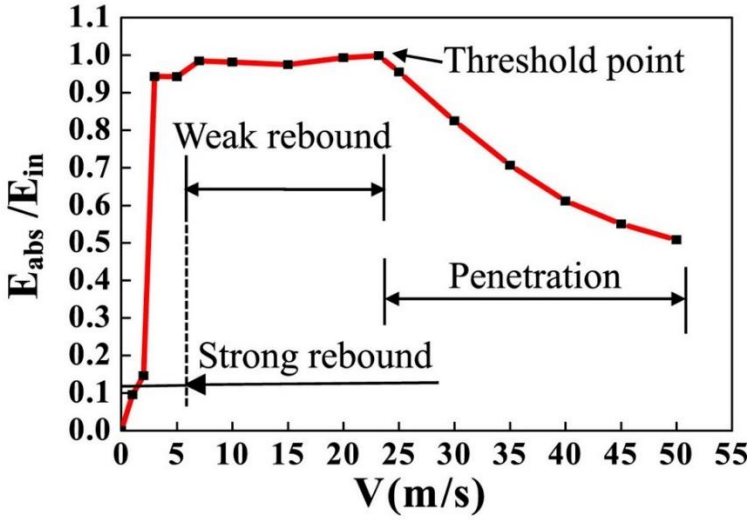

Figure 2.15. Energy absorption/initial kinetic energy. E_{abs} is the energy absorption of the human skull bone section, and E_{in} is the impactor's initial kinetic energy. [62]

In short, it can be said that the designed coupler should have high strength and for the life and stress analysis limitation can be taken as 5g when it is considered serious amount of the shock will be absorbed.

After this criterion, another point is manufacturability of the designed coupler, for this aim market research, is conducted. Nitinol and PTFE are mentioned as an alternative material; however, as explained before, nitinol's feasibility is low due to surgical operation constraints; and PTFE is a difficult material for arranging frequencies and is also hard to work in terms of machining. Thus, Grade 5 Titanium is selected as the material due to previously mentioned advanatges as well as high availability in the market. For such a small dimension and tight tolerance designs, one of the most suitable manufacturing techniques is electrical discharge machining (EDM). It is applicable to metals. Wire EDM is an electro-thermal manufacturing technique in which a fine single-stranded metal wire is used in conjunction with de-ionized water, which is used to transmit electricity; and to cut through metal using heat from electrical sparks while preventing corrosion. Figure 2.16, presents a schematic of the μ-Wire EDM device which also illustrates the working principle. With EDM, very small feature size parts can be machined. Minimum feature size is dependent on the diameter of the EDM wire. Therefore, wire-EDM micromachining technique is preferred for the manufacturing of the couplers.

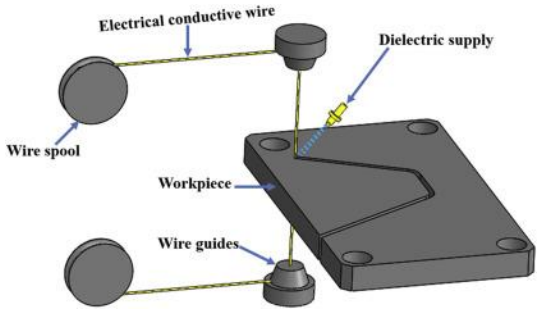

Figure 2.16. Schematics of Wire EDM [63]

2.2.3 Design and Simulations

As explained before, one of the location possibilities for transducer attachment is malleus neck. For this aim, one of the design possibilities, by considering manufacturability, is presented in Figure 2.17.

Figure 2.17. Malleus attachment system representative image

Clip is designed from Ti-Gr5 due to the previously explained reasons and it has a mass of 6.83 mg. In order to verify if the design provides the desired features, FEM simulations are conducted with ANSYS software. The flow of the simulation steps and the interface of the FEM simulations are presented in Figure 2.18.

a)

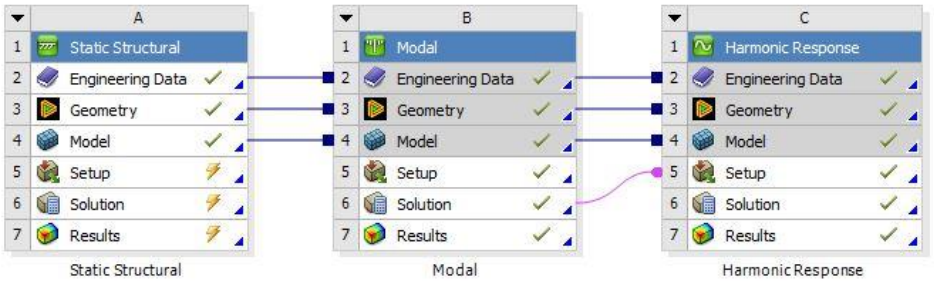

b)

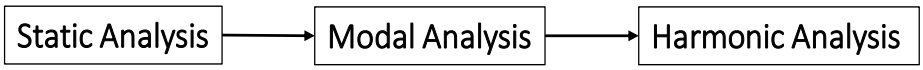

Figure 2.18. a) Interface of the Workbench Module of ANSYS for Executed Logic b) Logical Scheme of the FEM analysis of attachment system

First of all, pre-stressed modal analysis is conducted just under standard earth gravity in order to observe the natural frequency on its own. Then, simulations are repeated under 30mg distributed mass on the back of the clips where the transducer is glued.

Resonance frequencies and equivalent maximum stress values of the clips together with 30mg distributed mass and without mass loading are presented in Table 2.6. It can be observed from Table 2.6 that all resonances are out of the range, above 6kHz, as desired. Thus, according to transmissibility, it can be safely said that in a rigid coupling case transmissibility is 1 regardless of the damping ratio. Also, stress values under 5g acceleration from all three directions, are way lower than the yield strength of the Ti-Gr5 which is 795 Mpa.

Table 2.6 FEM results of the clips

	Resonance Frequencies (kHz)	***Equivalent Von-Misses Stress (kPa)***
Without mass loading	24.7 25.9 29.1 83.8	64.5
With 30mg distributed mass	8.9 9.5 10.9 33.2	452.5

After static and modal analysis, harmonic simulations are conducted. For this aim, effect of high SPL levels on clips is examined. For this purpose, 100dB is selected which corresponds to the SPL of power tools, jackhammers, sirens, and helicopter landings. SPL of 100dB corresponds to 2 Pa; thus, as an input 2 Pa is applied to the whole body. In Figure 2.19, stress distribution of the body under 2 Pa over frequency range of 20Hz and 20kHz is presented. It is seen that the maximum stress value is around the neck part of the clips and is about 9.6 Pa which is quite a safe value when the yield point of Ti-Gr5 is considered.

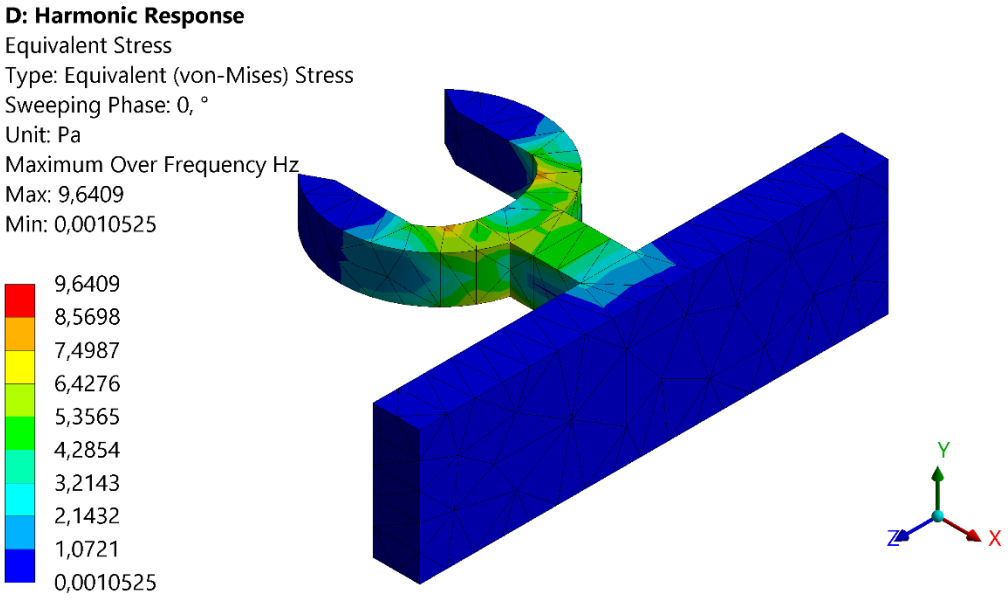

Figure 2.19. Equivalent Von-Misses stress distribution under 2 Pa

2.2.4 Cadaver Experiment

After FEM models are used to confirm the design, a cadaver experiment is conducted to examine the integration and vibration characteristics. Experiment was done in two steps. Firstly, coupler is attached to the incus short process together with the accelerometer (LSM6DSL [64]). Vibration characteristics of the ossicle chain is observed. Cyanoacrylate based adhesive is used on the surfaces of the clips, neck surface where it is attached to the bone and back surface where accelerometer is attached, in order to ensure the coupling between clips and bone is rigid. Secondly, clip is attached to the malleus which is the design's main placement location. The aim behind the selection of the malleus neck as an attachment location is to take advantage of the increased vibration amplitude when the incus is removed. Thus, integration of the design to the malleus bone is examined in terms of dimensions and ease of coupling.

In Figure 2.20, close-up images of the clips relative to malleus bone and transducer are presented. It can be seen that clip is suitable when its dimensions are compared with malleus bone and transducer.

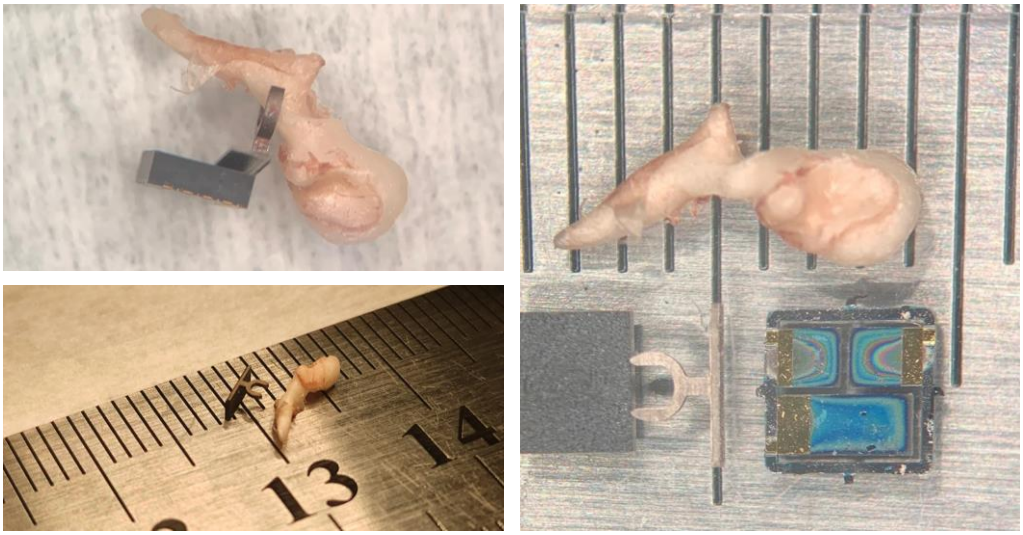

Figure 2.20. Clips, malleus bone and transducer close-up images

2.2.4.1 Vibration Results of The Incus

During the examination of the results following factors should be considered:

- Human to human, ossicles and middle ear characteristics differ, meaning different compliances, which results in different vibration characteristics. That is why multiple cadavers are required for commenting results, or at least we should know input vibration amplitude in umbo; then, by relating to it we can comment on transmissibility.
- Age, room temperature, the freshness of cadaver, setup technique and loadings affect the vibration characteristics.

In our experiment, around 25 mg mass loading effect should be observed but according to literature 20-30 mg has not much significant impact on the vibration amplitude, especially in low frequencies, which we conducted the experiment in that

range. The effect of mass loading on the ossicle chain vibration characteristics is examined by Gan et. al [65]. In their research, they placed two implants with masses of 37.5 mg and 22 mg in incudostapedial joint and observed the effect. For bones with an implant mass of 37.5 mg, the maximum decline of 5dB in stapes displacement was seen at 1500 Hz or 6000 Hz. Maximum loss of 3 dB at 1500 Hz was caused by implant mass of 22.5 mg in the bones. Over the frequency range of 1000 to 8000 Hz, the average impact of the lighter implant on stapes displacement was reduced by 2.6 dB. In Figure 2.21, the clip configuration at the experiment is shown. The accelerometer is glued to clips, and the overall attachment mechanism is placed on the short incus process.

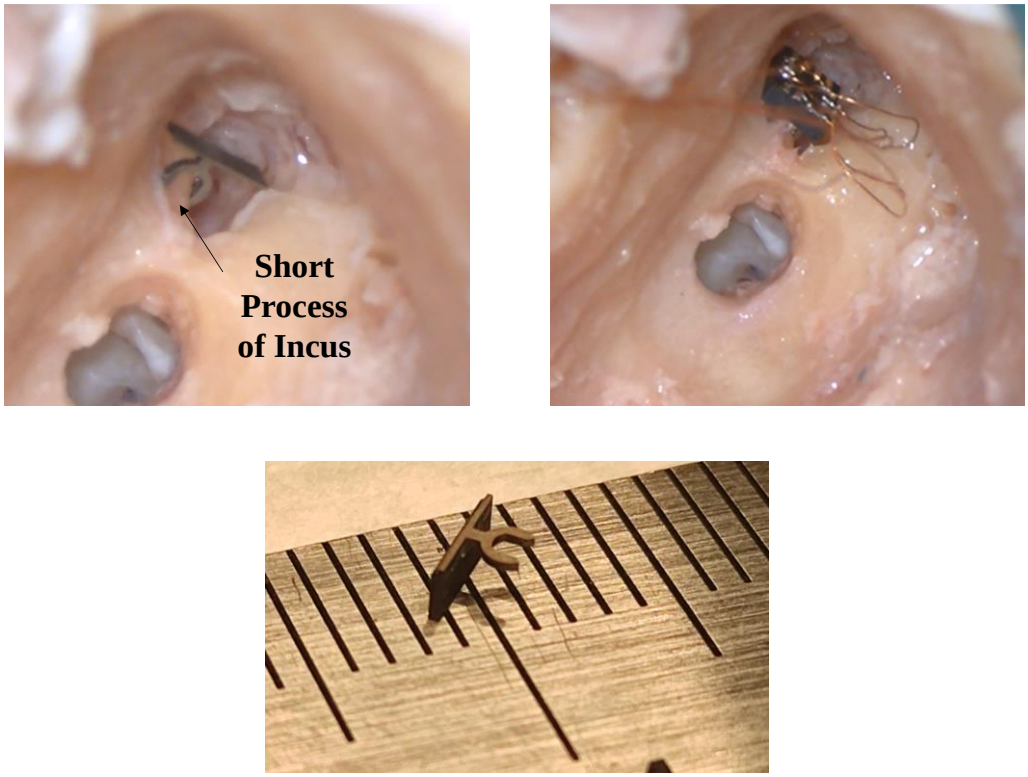

Figure 2.21. Attachment system. Left: Design at incus short process Middle: Together with accelerometer. Right: Manufactured design for the experiment

Umbo and Ossicles Vibration Characteristics Data from Literature

In Figure 2.22, umbo displacement data is presented for 80dB and 90dB [48], [66]. Based on the presented data in Figure 2.22 and in Figure 2.13 correlations regarding the incus vibration are conducted.

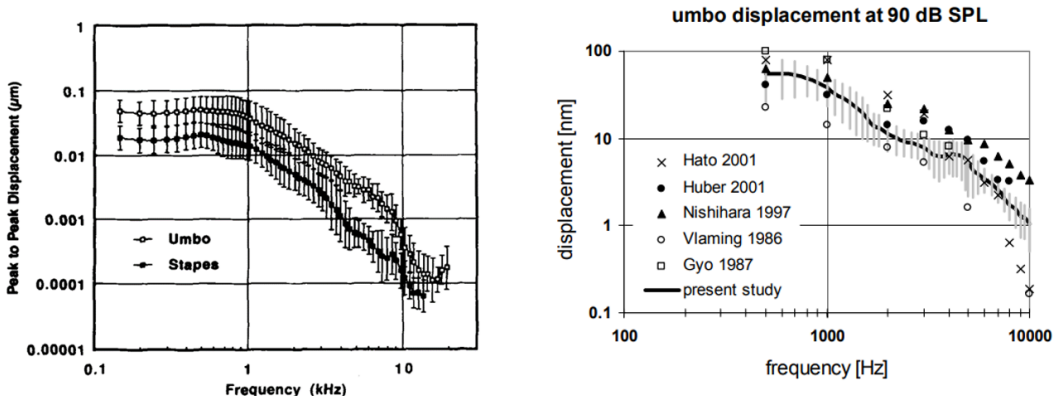

Figure 2.22. Left: Mean peak-to-peak displacement of the umbo and stapes at 80 dB SPL input at the TM in 15 human temporal bones [48] Right: Umbo displacement data at 90 dB SPL [66]

By using data presented in Figure 2.22, we can make the data at Table 2.7 for 500 Hz and 750 Hz (these two-frequency selected for compatibility with the experiment) by changing displacement values to g-values.

Table 2.7 Umbo Displacement Characteristics for 500 Hz and 750 Hz

Frequency (Hz)	**SPL (dB)**	**Displacement (nm)**	**Acceleration (mg)**
500 Hz	90	~60-100	~61.2-101.9
750 Hz	80	~40-70	~40.8-71.36

By using data presented at Table 2.7 on umbo displacements and correlate it with incus by using Figure 2.12, we can obtain the data in Table 2.8 for 500 Hz and 750 Hz by converting displacement values to g-values.

Table 2.8 Incus Displacement Characteristics from Literature

Frequency (Hz)	**SPL (dB)**	**Displacement (nm)**	**Acceleration (mg)**
500 Hz	90	~24-40	~24.2-40.3
750 Hz	80	~16-28	~16.1-28.2

In Table 2.9, incus vibration amplitude data from experiment tis presented in terms of both displacement and acceleration.

Table 2.9 Incus Displacement Characteristics from Experiment

Frequency (Hz)	**SPL (dB)**	**Displacement (nm)**	**Acceleration (mg)**
500 Hz	90	~25-27	~26-27
750 Hz	80	~16-18	~17-18

Change in dB and displacement is provided with below equation (4). Control displacement represents the displacement without any mass loading effect.

$$\Delta dB = 20 \log\left(\frac{d_{exp}}{d_{control}}\right) \qquad (4)$$

By using equation (4), we can check whether or not we are in the range of literature as follows:

- For 500 Hz → $d_{exp} = 25nm$
  - → $\Delta dB = -3db \;\; according\ to\ literature$ [65]
  - → $Then, we\ found\ d_{control}\ as\ around\ 35.2\ nm$
- For 750 Hz → $d_{exp} = 17nm$
  - → $\Delta dB = -3db \;\; according\ to\ literature$ [65]
  - → $Then, we\ found\ d_{control}\ as\ around\ 24\ nm$

Both of the found control data are in the expected range. Moreover, in Figure 2.23,for 80 dB experiment results are compared with data of [47] and [60] by correlating umbo data (by assuming there is around 2 times difference between vibration amplitudes of umbo and incus). In addition, the FEM model and the experimental data verified each other, as can be seen in Figure 2.23. Although there is correlation, it is known that vibration amplitude for incus can vary from cadaver to cadaver up to 10 times. Thus, it can be said that we are in a coherent region with literature.

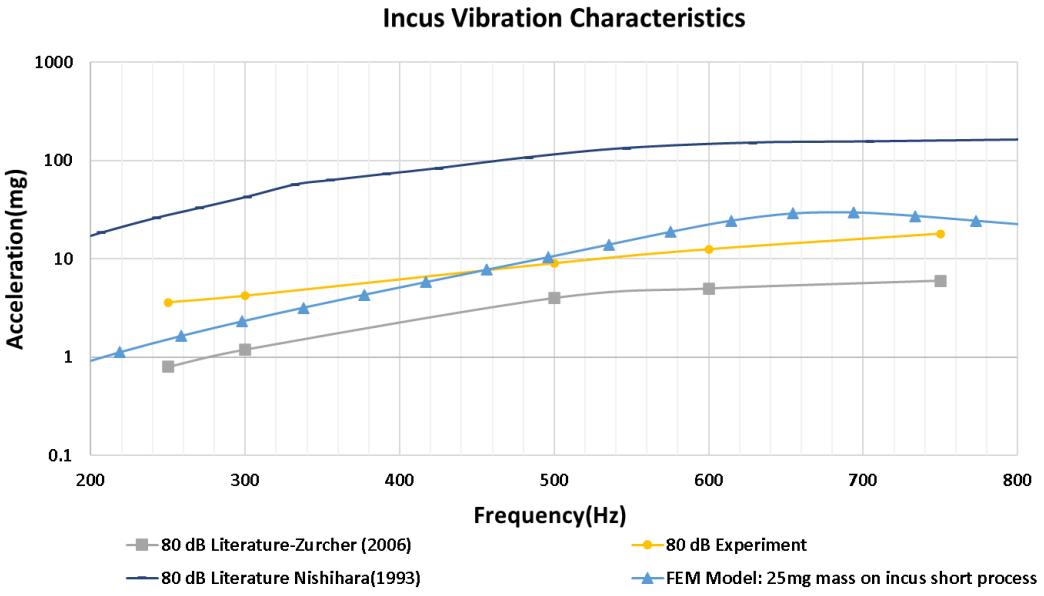

Figure 2.23. Comparison of experiment data with literature and FEM model

At this point, it is not possible to make any definitive comments because the input displacement data is not known; thus, everything is obtained by correlation. However, it could be said that:

- ✓ Collected experimental data is consistent with the data in the literature.
- ✓ Mass loading effect is consistent with the literature correlations.

2.2.4.2 Integration to The Malleus Bone

As explained before, an increase in the amplitude of the vibrations is expected due to the removal of the incus bone. Thus, in order to capture that increase, one of the possible locations for the clips is decided to be the neck part of the malleus bone.
In Figure 2.24, the clip at the malleus bone in the cadaver experiment is presented. During the cadaver experiment, it is observed that clip is rigidly attached to the neck part of the bone with a slight pushing force. In addition, dimensions of the attachment system and bones are coherent with each other. Herewith, it is seen that in terms of rigidness and dimensions, designed clip is well-suited to the malleus bone.

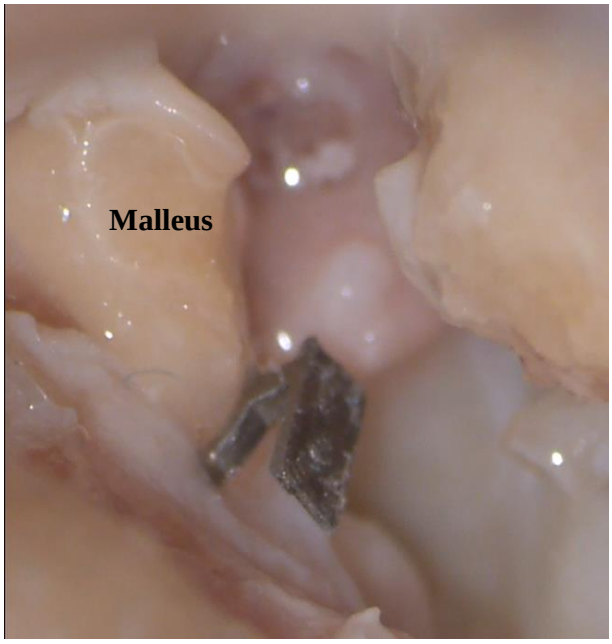

Figure 2.24. Malleus integration of the clips at cadaver experiment

2.3 Summary

In this chapter, as the beginning, a model of the middle ear is constructed. Firstly, tympanic membrane is drawn at Fusion 360; then, membrane is assembled with ossicles. After assembly of the membrane and ossicles, the model is exported into ANSYS and parameter calibrated FEM simulations are conducted in order to fit the model to experimental data in literature. By examining the model and literature, the most suitable location for the sensor placement is examined. Malleus and incus are selected as the most suitable locations for the placement of the sensor. After location selection, possible attachment designs are modeled. A coupler in which one end is fixed to the ossicles and another end can be fixed to the sensor is designed. Three material possibilities are examined, and Titanium Gr-5 is decided as the most suitable material in terms of machining, durability, mass, and stiffness. Lastly, FEM model of the middle ear and attachment mechanism is experimentally verified with a cadaver experiment. Collected data of the incus from the cadaver experiment is fit into the created FEM model. Results are consistent with the FEM model and the experimental data from the literature. Secondly, the attachment mechanism is examined in terms of dimensions, rigidness and mass. It is observed that coupler mechanism can fit into the constrained volume around the incus or malleus, and it wraps the incus and malleus in a rigid way. Moreover, overall vibration characteristics is not affected from the mass of the coupler and any mechanical filtering due to the coupler is not observed. To sum up, the designed coupler is suitable in terms of mass, dimensions and resonance frequency.

CHAPTER 3

Multi-Mode Multi-Channel Thin Film Piezoelectric Sensor Design and Modelling

As stated previously, main aim of this research is designing an efficient hearing sensor which filters the incoming sound mechanically without consuming energy. Thus, piezoelectric based vibration sensors are good choice for this purpose.

In this chapter, multi-mode thin film piezoelectric sensor is proposed, and its advantages are examined. Model is integrated into the cochlear implants as a sensor which mechanically filter the incoming sound.

3.1 Requirements and Limitations

Due to the nature of the human ear, some restrictions occur while designing a fully implantable sensor. First of all, middle ear has a very limited volume; thus, first limitation comes from volume. Design should satisfy dimensional constraints. Secondly, whole hearing chain can be modelled as discrete mass-spring-damper system because actually, every system can be approximated to behave like a mass-spring-damper system. Thus, hearing chain has its own stiffness and damping characteristics. Adding an outer component to the system means overall stiffness-mass-damping characteristics of the system will change. It is well-known that mass-loading lowers the vibration amplitude of the ossicle chain [65]. Thus, mass of the sensor should be also considered while designing the sensor. Except these two limitations, there are also two main requirements. One of them is amplitude of the stimulation signal. In order to provide the hearing via piezoelectric sensor, output of the sensor should be processed via an interface circuit, and then, this processed signal is used for stimulating the auditory nerves, where hearing occurs. Therefore, the output of the sensor should provide enough amplitude to stimulate the circuit. The

final requirement is the operating frequency range of the sensor. In a healthy human being, hearing occurs between 20Hz and 20kHz but most of the syllables are distributed in a specific range. Thus, a useful operating frequency range should be set for the sensor.

3.1.1 Limitation I: Dimensions of The Sensor

Sensor is designed to be placed on the ossicles whether on the incus or malleus neck. Between the external ear and the internal ear lies the tympanic cavity. In Figure 3.1, dimensions of the middle ear are presented [67]. The vertical diameter of this small, uneven region is around 18 mm, the anteroposterior diameter is around 10 mm, and the transverse diameter is around 3 to 5 mm [67], [68]. The volume of the tympanic cavity changes around 452 mm^3 to 640 mm^3 according to the infant or adult human [67], [68]. Moreover, according to the study of Zurcher et.al [60] after the incus removal, there is almost 10 times increase observed in the amplitude of vibration in addition to the volume increase in the middle ear. In consequence of these limitations, 5mm to 5mm sensor footprint in terms of dimensions is seen as feasible for placing in malleus neck in case of the incus removal, or placing to the incus without spoiling the ossicle chain.

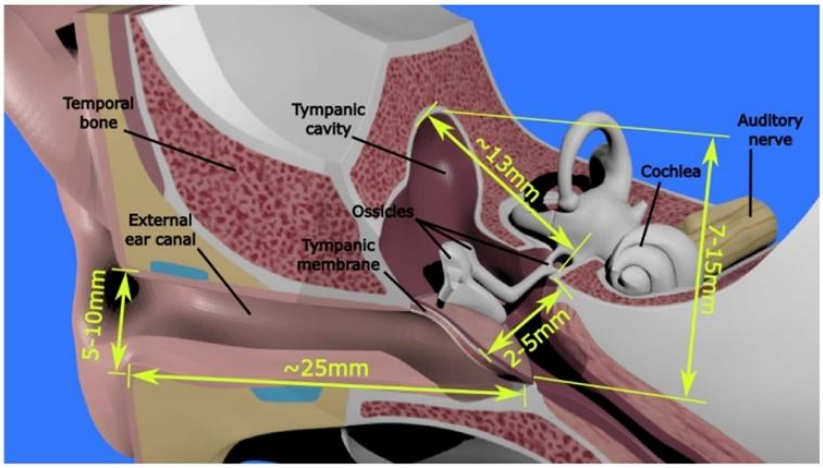

Figure 3.1. Dimensions of the middle ear [67]

3.1.2 Limitation II: Mass of The Sensor

When whole auditory system is modelled as mass-spring-damper system, it is seen that adding an outer part, in this case coupler and sensor, means adding an extra mass-spring-damper element, which affects the overall vibration characteristics of the system. In study of Gan et.al [65], mass loading effect on the ossicle chain is examined via using two implants with masses 37.5mg (Model 1) and 22.5mg (Model 2) respectively in 17 fresh-frozen temporal bones. In Figure 3.2, change in amplitude of the stapes displacement in terms of dB due to mass loading effect of implants are presented in between 250 Hz and 8000Hz. According to the results, maximum drop is seen as 5 dB for implant model 1(37.5mg) at the frequency range of 1500Hz and 6kHz; and for implant model 2 (22.5mg) maximum drop in stapes amplitude is observed as average 2.6 dB between 1500 Hz and 8000Hz. For both implants, it is observed that there is no significant difference in amplitude at low frequencies, between 250Hz and 750Hz. Under the light of all of these experiments, overall mass loading limitation for the sensor is taken as 25mg.

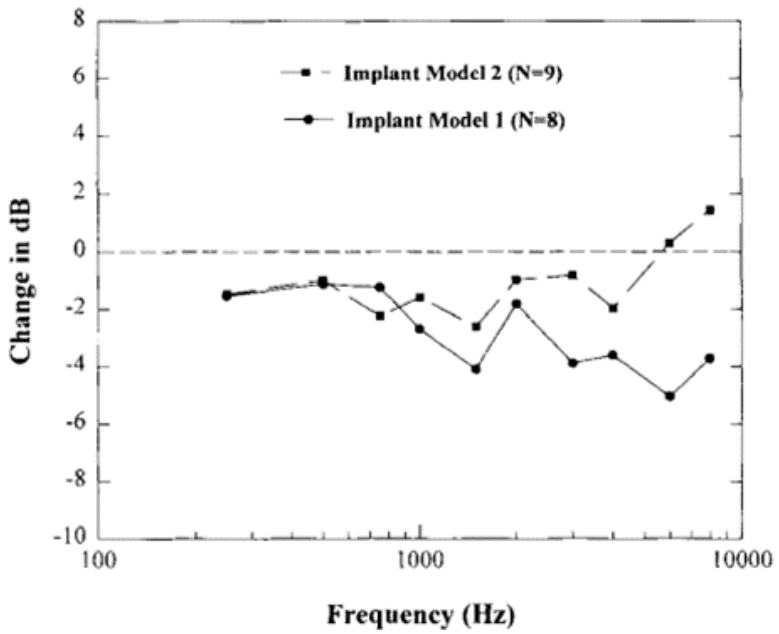

Figure 3.2. Change in dB due to mass loading effect of implant model 1 (37.5mg) and model 2 (22.5mg) [65]

3.1.3 Requirement I: Base Amplitude of The Stimulation Signal

In the proposed FICI mechanism FLAMENCO [69], the overall concept is explained as follows. When the acoustic sound waves vibrate the tympanic membrane, acoustical wave vibration is transformed into mechanical vibration, and this mechanical vibration is collected by piezoelectric transducer. The piezoelectric transducer generates output voltage which is amplified by the interface circuit. Then, the amplified signal is transmitted to the auditory nerves, and hearing occurs. As a consequence, the designed sensor should give enough output in order to stimulate the interface circuits. The threshold for the stimulation of the circuit is defined as 100μV based on the studies of Hasan Uluşan [30].

3.1.4 Requirement II: Operating Frequency Range

The audible range of a healthy human ear lies between 20Hz and 20kHz. The upper and lower limits of the audible sound pressure levels of the healthy human ear lies between 20μPa and 20Pa which corresponds to 0 dB SPL and 140 dB SPL respectively in logarithmic scale.

Although the most ideal case for a hearing sensor is mimicking the natural characteristics of the ear, it is not succeeded yet. Thus, the range in which most of the syllables lie is chosen as design parameter for sensor.

For the men and women fundamental frequency of the complex speech tone, which is also named as pitch, is between 85Hz to155Hz, and 165 to 255 Hz respectively [70]. Also, in non-tonal languages such as Western languages, between 250Hz and 8kHz are the most important range in terms of intelligibility [71]. In Figure 3.3, graph of the equal loudness contour is presented. It demonstrates how various frequencies are perceived in relation to one another. It shows that the ear is more sensitive to the frequency ranges of about 250Hz to 8 kHz compared to lower and higher frequencies.

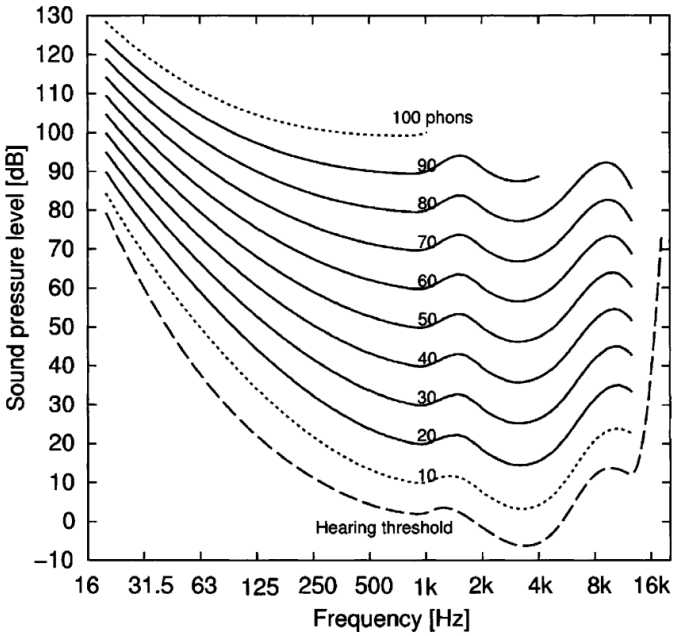

Figure 3.3. Equal loudness contour [72]

In Figure 3.4, the operating frequency ranges of the two commercial cochlear implants are illustrated. For the devices of the MED-EL operating frequency range is taken in between 70Hz and 8500Hz; while in the devices of the Nucleus this range lies between 188 Hz and 7938 Hz, and, they have 12 and 22 electrode contacts respectively [73].

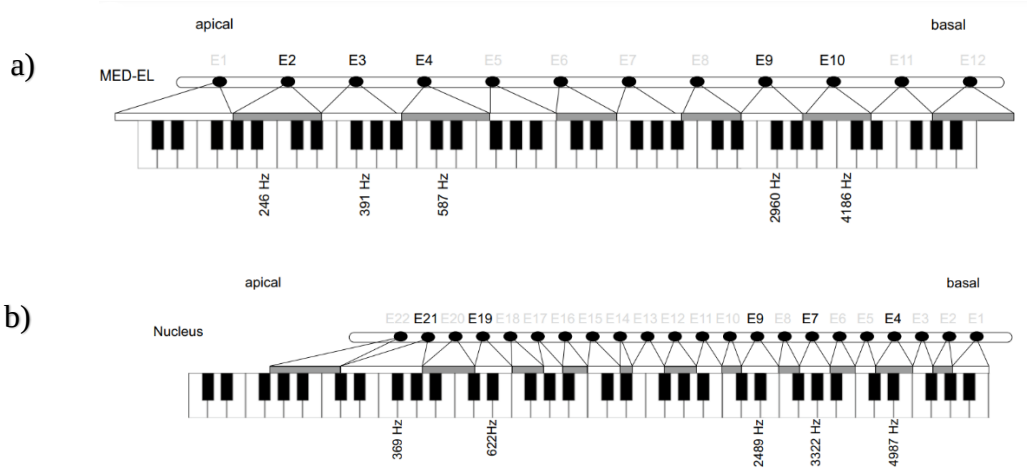

Figure 3.4. a) Operating frequency range of MED-EL device together with electrode contacts b) Operating frequency range of Nucleus device together with electrode contacts [73]

As a consequence, for the design of the sensor operating frequency range is taken in as 300Hz to 6kHz by considering the frequency of the highest level of intelligibility and ranges of commercial products.

3.2 Sensor Design and Design Parameters

Main aim of this research is proposing a new and improved approach to the previously designed transducers [28]-[29], [74]. The design of the sensor is composed of two main parameters, one of them is the material selection, and the other is geometry. Both of the parameters should be adjusted and optimized in a way to fulfil the requirements by also following the limitations.

3.2.1 Material Selection

In material selection, the main requirements from such material are enabling working on complex geometries and arrays while providing high output in terms of voltage. In previous years, Beker et.al worked with bulk PZT as harvester and sensor in order to eliminate the need of microphone, sound processor, battery, and transmitter [74]. Although it is a good approach, one cantilever has a footprint of 4.25x4x0.6mm^3. Thus, it is not feasible unless bulk cantilevers would become small enough to work in an array sense. After this approach, İlik et.al [29] presented thin film pulsed laser deposited (PLD) PZT based array of cantilevers as a piezoelectric transducer. Main aim of choosing PLD PZT is to be able to work on the small size of beams in an array configuration; thus, desired mechanical filtering can be obtained. After the validation of the performance of PLD PZT as an active layer of sensor with the coherent trade-off between dimensions and output voltage, Yüksel et.al [28], showed that it can be used as an array of 8 cantilevers. Moreover, he validated his results with in-vivo experiments. Thus, in the light of the previous studies in BioMEMS group, PLD PZT is chosen as the material.

Lead zirconate titanate in the form of Pb ($Zr_{0.52}Ti_{0.48}$) O_3 or in other words PZT is one of the most popular materials due to its superior ferroelectric and piezoelectric properties. However, in order to integrate it in MEMS and working in small, complex geometries, thin film form is needed. Thus, the properties of the thin film PZT are critical while working on whether a sensor or an actuator. In this research, desired coefficient of PLD PZT is transverse coefficients (e_{31}). 1µm PLD PZT deposition of the wafers is done at MESA+ Nano Lab's cleanroom (University of Twente, The Netherlands). PZT films were deposited on silicon wafers. Ti/Pt which forms bottom electrode layer was used as an adhesive layer. Piezoelectric properties due to the polarization are provided from the MESA+. Figures of merit and effective transverse piezoelectric coefficient calculations are presented in equations (5,6) [75], [76]. $e_{31,f}$ represents the effective transverse piezoelectric coefficient, $\varepsilon_{33,f}$ and ε_0 represent the effective relative dielectric constant of the thin film PZT, and the vacuum dielectric constant which has a value of 8.854×10^{-12} F/m respectively. In equation (6), z_i is used for identifying the center of the layer from the selected origin, A_i is the cross-sectional area of the layer, w and t are the width and thickness of the layer, s is the mechanical compliance, E is the young's modulus, L is the length of the cantilever, n is the total number of layers, δ_T is tip displacement, and V_{ac} is the applied sinusoidal ac-voltage. Subscript "p" is used to indicate that parameters are for piezoelectric film.

$$FOM = \frac{e_{31,f}^2}{\varepsilon_{33,f}\varepsilon_0} \tag{5}$$

$$e_{31,f} = \frac{\sum_n^i E_i A_i \left(\left(\frac{t_i^2}{12}\right) + z_i^2\right)}{E_p z_p w_p (s_{11,p} + s_{12,p})} \frac{2\delta_T}{L^2 V_{ac}} \tag{6}$$

In Figure 3.5a, piezoelectric coefficients and wafer position relation is presented [77]. Although the transverse piezoelectric coefficient shows a little deviation, in

general, it also follows a trend. This slight deviation's reason can be explained with more vacancies at the wafer center. The quality and crystallinity of the coated wafers can be commented by examining the X-Ray diffraction patterns of the thin layers which are presented in Figure 3.5b. In XRD, 4 orientations are examined which are (001), (110), (111) and (002) respectively for each peak at Figure 3.5b, and, from the graph, it is observed thin film has good uniformity and crystallinity.

a)

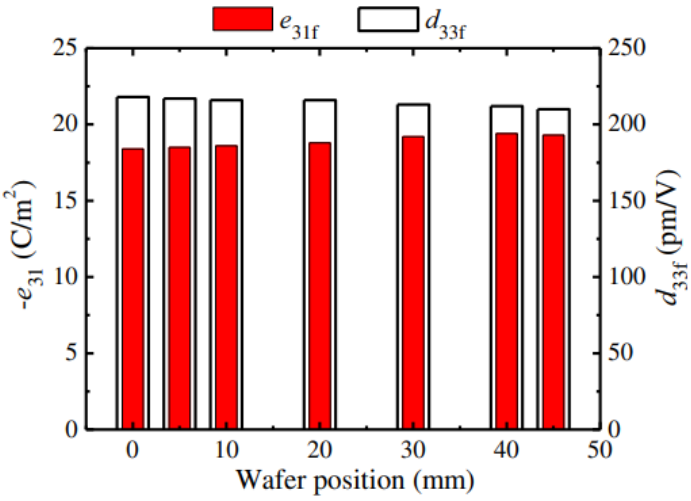

b)

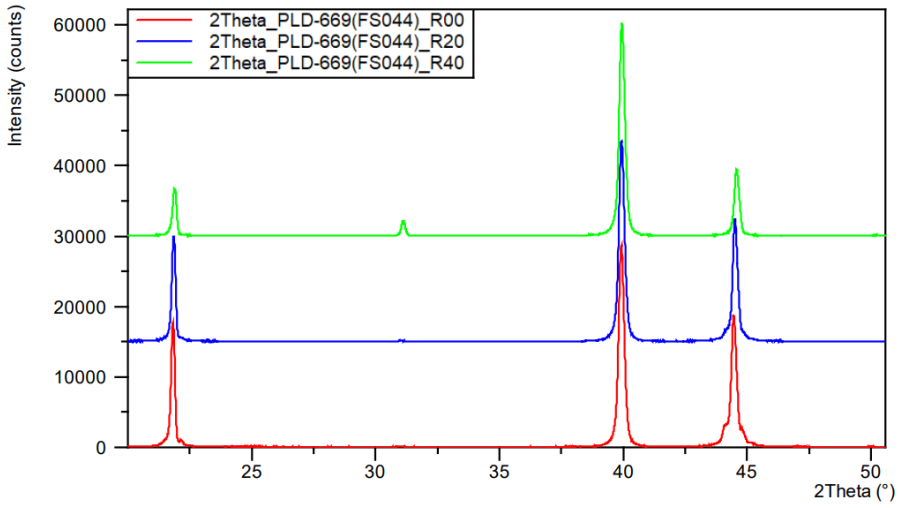

Figure 3.5. a) Piezoelectric coefficients and position of 4-inch PLD PZT deposited SOI wafer [77] b) XRD pattern of PLD PZT provided by MESA+

The main properties of the 1μm thin film pulsed laser deposited PZT is presented in Table 3.1. Some of the presented properties are calculated according to the above presented equations, and the remaining ones are provided by the MESA+ and obtained experimentally. Remnant polarization is presented as three data which are according to wafer position of 0mm (wafer center), 20mm, and 40mm respectively.

Table 3.1 Properties of Thin Film PLD PZT

Density	7600 kg/m^3
Poisson's Ratio	0.279
Youngs Modulus	103 GPa
$\varepsilon_{33,f}$	2500
ε_0	8.854x10^{-12} F/m
$e_{31,f}$	-20.4 C/m^2
Remnant Polarization (P_r)	10.2/7.6/5.2 μC/cm^2

3.2.2 Proposed Design I: M-Shape Multi-Mode Piezoelectric Transducer

In this section, a design which will widen the audible frequency range by providing the minimum of 100μV and also in terms of footprint which is not exceededing 5mm by 5mm is tried to be modeled.

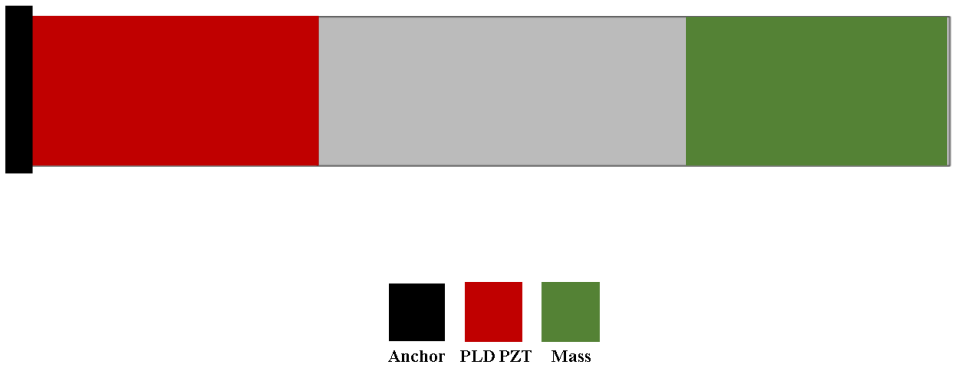

Figure 3.6. Single-regular cantilever illustration

The regular single cantilevers can be used in an efficient way to provide mechanical filtering to the incoming sound which is previously performed by Yüksel et. al [29] in a multi-channel configuration at a 5mm-by-5mm footprint. Simplified analytical modeling of the single beam can be executed [78]. In order to calculate the natural frequency of the beam, effective stiffness and effective mass of the beam should be calculated. The cantilever beam is composed of multi-layers such as PZT, silicon, electrode, and insulation layers. Thus, neutral axis of the composite beam is calculated according to the equation (7).

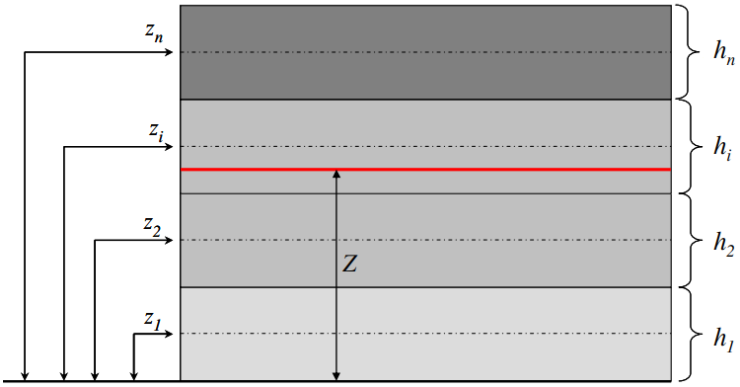

Figure 3.7. Multi-layered composite beam structure [78]

$$Z = \frac{\sum_{i=1}^{n} Y_i h_i (\sum_{j=1}^{i} h_j - (\frac{h_i}{2}))}{\sum_{i=1}^{n} Y_i h_i} \qquad (7)$$

Second moment of inertia of a beam is calculated according to the equation. (8) in which is adjusted according to each layer included by based on the parallel axis theorem.

$$\bar{I}_i = \frac{w_i h_i^3}{12} + A_i \bar{z}_i^2 \qquad (8)$$

$$\bar{z}_i = z_i - Z$$

Then, total and effective stiffness of the beam is calculated as in equation (9). Beam length and mass length are presented as l and l_m respectively.

$$k_T = \frac{3}{l^3}\sum_{i=1}^{n} Y_i \bar{I}_i \tag{9}$$

$$(k_T)_{eff} = k_T \times (1 + \frac{3l}{4l_m})^{-1}$$

After finding effective mass, natural frequency of the cantilever can be calculated according to the eqn. (10).

$$m_{eff} = \frac{4m}{3} \times \frac{l_m}{l} \tag{10}$$

$$f = \frac{1}{2\pi}\sqrt{\frac{k_{eff}}{m_{eff}}}$$

After resonance frequency of the cantilever is found, piezoelectric modeling is conducted. Main piezoelectric constitutive equations are described in below equations. (11). ζ_i, s_{ij}^E, T_i,E_i, D_i and d_{ij} are presented the strain, compliance, stress, electric field, electric displacement, and piezoelectric constant. Dielectric permittivity of the vacuum and material are denoted with ε_0 and ε_{33} .

$$\begin{aligned}
\zeta_1 &= s_{11}^E T_1 + s_{12}^E T_2 + s_{13}^E T_3 + d_{31}^E E_3 \\
\zeta_2 &= s_{12}^E T_1 + s_{11}^E T_2 + s_{13}^E T_3 + d_{31}^E E_3 \\
\zeta_3 &= s_{13}^E (T_1 + T_2) + s_{33}^E T_3 + d_{31}^E E_3 \\
D_3 &= d_{31}(T_1 + T_2) + d_{33} T_3 + \varepsilon_0 \varepsilon_{33}^T E_3
\end{aligned} \tag{11}$$

Based on the above-described equations, electric displacement can be defined as a function of strain as follows:

$$D_3 = \left(\frac{d_{31}}{s_{11}^E + s_{12}^E}\right)(\zeta_1 + \zeta_2) = e_{31}(\zeta_1 + \zeta_2) \tag{12}$$

In this research, thin film piezo material is preferred; thus, it can be assumed that strains are uniform throughout the thin film. Longitudinal and transverse strains are related to each other with the Poison's ratio; and electric displacement can be rewritten based on this relationship as shown in equation (13).

$$\upsilon_b = \frac{\zeta_2}{\zeta_1} \qquad (13)$$

$$D_3 = e_{31}(1-\upsilon_b)\,\zeta_1(x)$$

$\zeta_1(x)$ is the strain distribution function and it can be expressed as:

$$\zeta_1(x) = \frac{3h_b}{l_b}\left(\frac{2l_b + l_m - 2x}{4l_b^2 + 9l_b l_m + 6l_m^2}\right)\delta_m \qquad (14)$$

in which h_b, l_b and l_m are denoted as beam thickness, beam length, and mass length respectively. δ_m represents tip mass displacement at the fundamental mode and x describes the position on the beam.

Under the assumption of constant stress and strain components, open circuit voltage can be expressed as in equation (15) based on the relations explained above.

$$V_{oc} = \frac{-e_{31}}{\varepsilon_0 \varepsilon_{33}^T}\left(\frac{t_p}{l_b}\right)(1-\upsilon_b)\int_0^{l_b}\zeta_1(x)dx \qquad (15)$$

where t_p represents piezoelectric film thickness. Electromechanical coupling is another important parameter that defines the amount of energy conversion between mechanical energy and electrical energy. It can be defined as in equation (16) with a related to w_{oc} and w_{sc}, open-circuit and short-circuit resonance frequencies respectively.

$$K^2 = \frac{w_{oc}^2 - w_{sc}^2}{w_{sc}^2} \qquad (16)$$

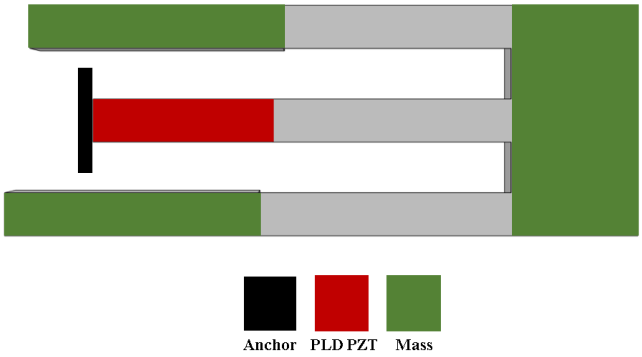

Figure 3.8. M-Shape Cantilever Illustration

Multi-mode cantilevers are a good option because of obtaining more than one resonance while remaining the same dimensions with single cantilevers; thus, with multi-mode designs, wider bandwidth can be covered. Wu.et.al (2015) [79] proposed an M-shape harvester from aluminum cantilevers and copper masses together with PVDF piezoelectric material. Their proposed device is not MEMS based and cantilevers lengths and widths are up to 110 mm and 40 mm respectively. In Figure 3.9, open circuit voltage results of the PVDF covered cantilevers are presented. It can be seen that due to the three consecutive resonances without significant drop meaningful voltage output is obtained.

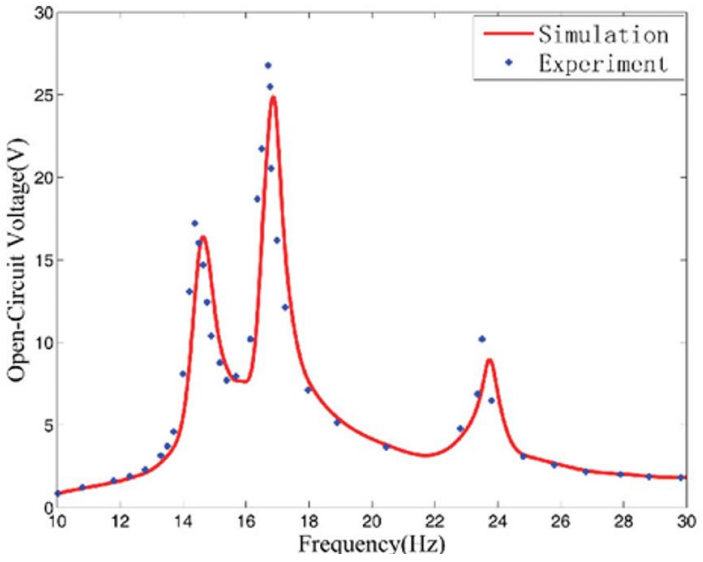

Figure 3.9. Open circuit voltage results of M-shaped multi-mode Piezoelectric cantilever [79]

Lumped parameter model for the M-shaped cantilever can be constructed. Wu et. al (2015) [79] performed extraction of mass and stiffness matrices under circumstances of same Youngs modulus, neglecting the distributed mass of the beam. Tip masses are denoted as m_1, m_2, and m_3 with the condition of $m_2=m_3$, and it is assumed that width of the anchored beam(w_1) is twice of the other two beams($w_2=w_3$).

$$M = \begin{bmatrix} m_1 & 0 & 0 \\ 0 & m_2 & 0 \\ 0 & 0 & m_3 \end{bmatrix} = m_1 \begin{bmatrix} 1 & 0 & 0 \\ 0 & \alpha & 0 \\ 0 & 0 & \alpha \end{bmatrix} \tag{17}$$

$$K = \frac{3EI}{\left(1-3\beta+\frac{15}{4}\beta^2+2\beta^3\right)\left(1-3\gamma+\frac{15}{4}\gamma^2+2\gamma^3\right)L_1^3} \times$$

$$\begin{bmatrix} 4(1-3\beta+3\beta^2+\beta^3)(1-3\gamma+3\gamma^2+\gamma^3)-(1-\frac{3}{2}\beta)^2(1-\frac{3}{2}\gamma)^2 & \left(\frac{3}{2}\beta-1\right)\left(1-3\gamma+\frac{15}{4}\gamma^2+2\gamma^3\right) & (\frac{3}{2}\gamma-1)(1-3\beta+\frac{15}{4}\beta^2+2\beta^3) \\ (\frac{3}{2}\beta-1)(1-3\gamma+\frac{15}{4}\gamma^2+2\lambda^3) & (1-3\gamma+\frac{15}{4}\gamma^2+2\lambda^3) & 0 \\ (\frac{3}{2}\gamma-1)(1-3\beta+\frac{15}{4}\beta^2+2\beta^3) & 0 & (1-3\beta+\frac{15}{4}\beta^2+2\beta^3) \end{bmatrix}$$

By using above presented equations, eigenfunction can be described. Eigenvalues and first three resonances can be obtained via defined eigenfunction.

$$|K-\omega^2 M| = 0 \tag{18}$$

$$\omega_1^2 = 4\pi^2 f_1^2 = \frac{3EI}{m_1 L_1^3} f_1(\alpha,\beta,\gamma)$$

$$\omega_2^2 = 4\pi^2 f_2^2 = \frac{3EI}{m_1 L_1^3} f_2(\alpha,\beta,\gamma)$$

$$\omega_3^2 = 4\pi^2 f_3^2 = \frac{3EI}{m_1 L_1^3} f_3(\alpha,\beta,\gamma)$$

Dimensionless parameters of α, β and γ are defined as proof mass ratio (m_2/m_1 or m_3/m_1), first longitudinal ratio (L_2/L_1), and second longitudinal ratio (L_3/L_1) respectively; and f_1, f_2, and f_3 are the functions which are used for defining first three resonance frequencies of the multi-mode, multi-degree of freedom m-shape design.

To the best of our knowledge, there is no MEMS-based application of this shape studied in the literature. Due to its previously listed advantages, it is decided that M-shape design can be integrated into this research for obtaining multiple resonances and increasing the covered frequency range.

3.2.3 FEM Modelling and Optimization of the Design Parameters

The validation of the design over a single regular cantilever and lumped modeling of the multi-mode design is conducted in the previous seciton. In this section, an adaptation of the design as hearing sensor for fully implantable cochlear implant system is performed together with FEM modelling in COMSOL, optimization of the resonances and dimensions.

The finite element method (FEM) is a numerical approach for simulating physical phenomena through discretizing the physical system into finite elements. It offers characteristics that are basic, concise, and result oriented. It is an approximation approach that separates a complicated problem area, or domain, into many little, smaller components (the finite elements) whose function can be explained using fairly simple formulas. In this methodology various FEM tools can be used but for this research due to its developed piezo module and its available interface between different environments COMSOL is preferred.

The goal of the design is to model a piezoelectric sensor that operates at the frequency range of 300Hz and 6kHz while providing a minimum of 100μV output. As previously stated for this purpose multi-mode, multi-dof M-shaped cantilevers are proposed. In order to integrate them into the 5mm×5mm area, dimensional optimization should be performed with a compromise between fabrication limits and resonance frequencies. Design parameters and parameters to be optimized are presented in Table 3.2 and in Figure 3.10 respectively.

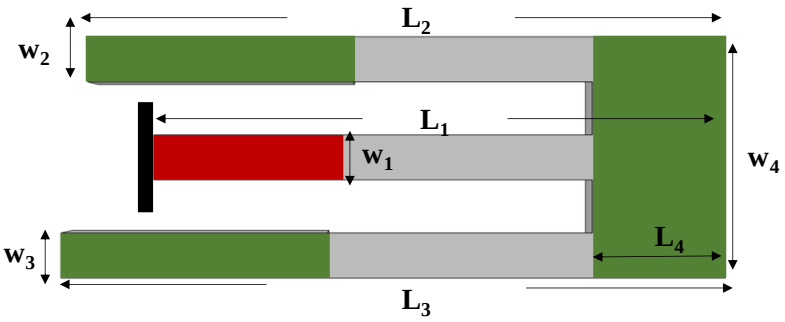

Figure 3.10. Dimensional parameters to be optimized

Table 3.2 Design Parameters

Input Parameters		**Optimized Parameters**	**Controlled Outputs**
Material	Silicon PLD PZT	Length of the beams	Resonance frequencies
		Width of the beams	
Beam Thickness	15 µm	Width of the spacings between the beams	Output voltage
		Width of the proof masses	
Mass Thickness	500 µm	Length of the proof masses	Critical stress points
		Length of the PZT layer	

As an input parameter, material selection is previously explained; hence, as piezo material PLD PZT is decided due to its superior and suitable properties for this research. The base beam material is silicon which is the most widely used MEMS material. Among these parameters, device and handle layer thicknesses are also previously set as 15µm and 500µm. After providing input parameters to the FEM software, COMSOL, dimensional tuning according to the desired output ranges is conducted. Followed logical scheme for FEM model is presented in Figure 3.11.

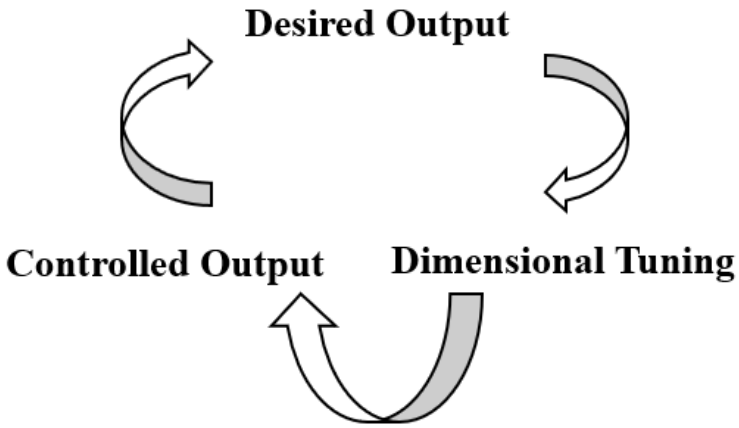

Figure 3.11. Logical scheme of the FEM simulations

After the parameters were defined, the initial design was drawn, and material assignments were conducted. It is assumed that silicon behaves as an isotropic linear elastic material. For both materials, PLD PZT and silicon, damping value is decided according to the pre-studies of the BioMEMS group [28], [29], [74] and pre-optimized fabrication flow. Under these circumstances, assumptions used during FEM simulations are as follows:

- Material damping model is taken as isotropic, and value of the damping is decided as 0.0007.
- Electrical damping is neglected.
- Connected load was ideal ($R_{load} = \infty$).

One of the most important aspects of getting correct results from a FEM model is meshing. To correctly discretize stress gradients, the mesh components must take into consideration a variety of factors. Because the designs are better sampled over the physical domains, the finer the mesh size, the more precise the solution. The trade-off is between higher accuracy and longer computational times. A metric for a good meshing is the mesh element quality. It is a dimensionless quantity between 0 and 1 which first one represents spoiled element and latter one represents perfectly regular element.

For the meshing of the design, two methodology is followed for two material domains of silicon and PZT. For the silicon domains, thicknesses are larger than the

PZT domains. Also most critical part of the design is PZT; hence, instead of extremely fine meshes and refinement, a little coarser model can be preferred at the bulk silicon parts. Therefore, in silicon domains, 12032 tetrahedral elements are preferred with average element quality of 0.5421. For 1μm PLD PZT domain, 675 triangular prism elements are preferred with average element quality of 0.8522. During the meshing of the PZT domain, the first surface of the domain is meshed with free triangular prism elements with extremely fine element size which has minimum element size of 500Å and maximum element size of 50μm. Then, surface is turned into a volume composed of 5 layers with swept-distribution mesh model. The detailed mesh model is presented in Figure 3.12.

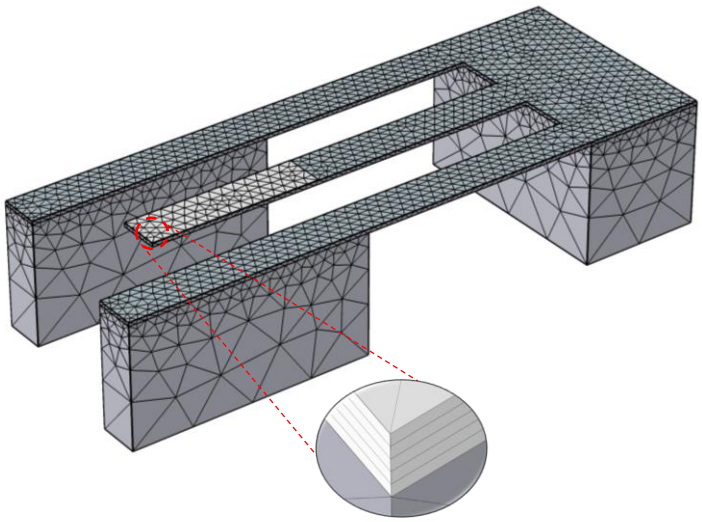

Figure 3.12. Meshed model of the M-shape design with zoomed in PLD PZT layer

COMSOL simulation is composed of three main physics which are solid mechanics module, electrostatics module, and piezoelectric module. Based on these modules, two analyses are conducted in the scope of this research which are eigenfrequency analysis and frequency response function, FRF, analysis. At first, with eigenfrequency analysis, resonances of the beams are found; and, then with FRF, output voltage under excitation force on the beam around resonance is examined.

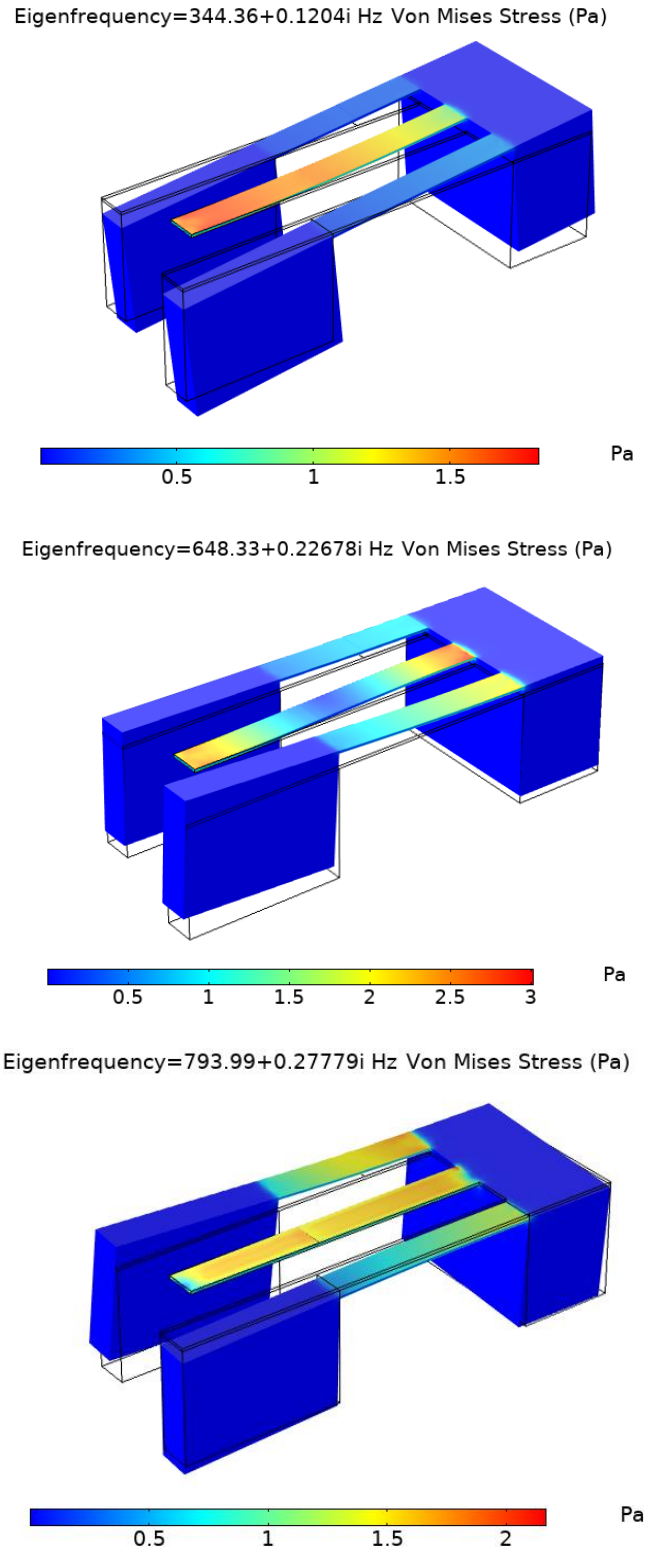

Figure 3.13. Von Mises stress distribution for the first three bending modes of the M-shape cantilever

The excitation force for the FRF analysis is decided according to the mechanical characteristics and response of the middle ear. Due to the nature of the middle ear, it behaves like a lever mechanism and up to 20dB amplification can occur inside the ear. However, this amplification amount is not constant or linear; it changes with respect to frequency of the incoming sound. According to the Zurcher et. al [80] study at human temporal bones, umbo displacement in terms of g is presented in Figure 3.14. In their research, medial wall is removed while reaching umbo with surgical operation. It is known that mechanical characteristics of the middle ear slightly differ due to the surgical operation; however, it is assumed that this does not change characteristics significantly. Thus, for the sake of this research, any kind of surgical effects on mechanical characteristics of the ossicle chain is neglected. From Figure 3.14, 0.1g is equivalent to approximately 90- 100dB at 1kHz and due to the characteristics of the curve, it corresponds much lower SPL levels above 1kHz. Thus, excitation force is taken as 0.1g in FRF analysis at COMSOL.

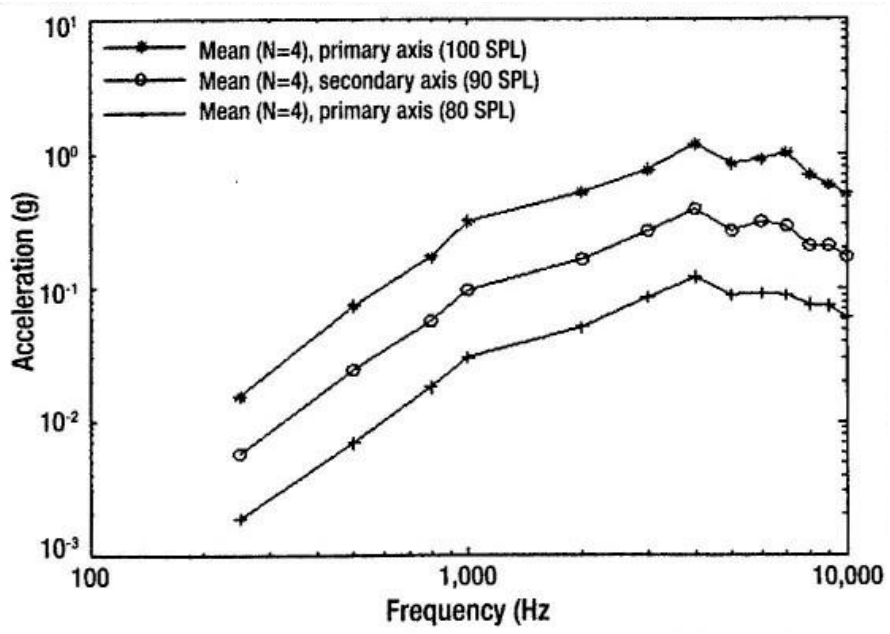

Figure 3.14. Umbo axis representation and responses of the umbo under SPL of 80 dB and 100 dB [80]

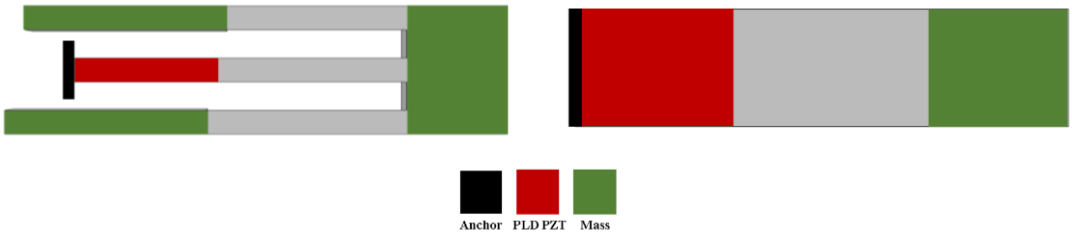

Figure 3.15. M-shape and regular single cantilever illustration

As a first thing, the validation of the design is done by comparing the FRF results for the two cantilevers of the same size, one M-shape and one regular. The M-shape design which has modes at 354Hz, 657Hz, and 847Hz compared with a single cantilever which has a mode at 600Hz. Both designs have a 1mm width and lengths are 2.65 mm for M-shape and 2.7mm for the single regular beam. In Figure 3.16, FRF responses of the M-shape and regular cantilever are presented. From Figure 3.16, it can be observed that with M-shape design wider range can be covered compared to the regular single beam configuration with the same dimensions.

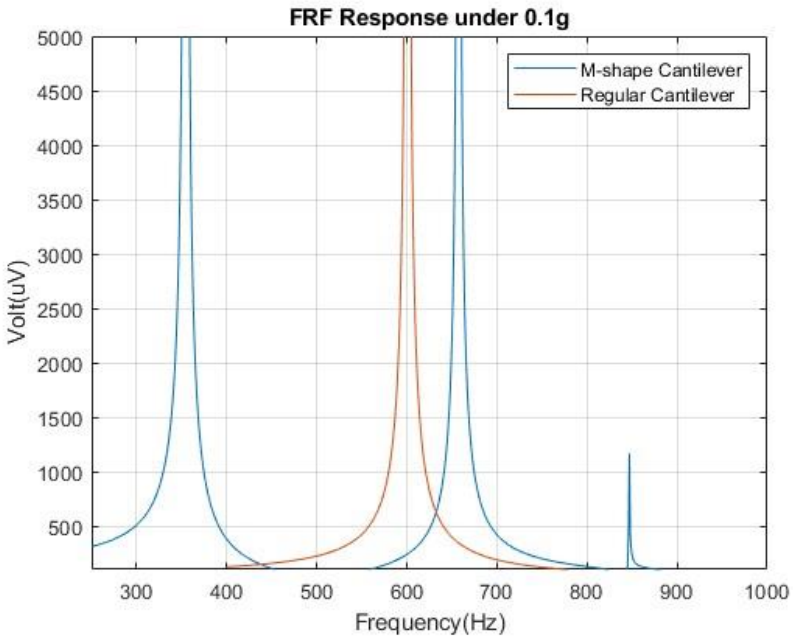

Figure 3.16. FRF results comparison of the two designs

After multiple trials, it is seen that above 2500 Hz, M-shape designs are not as advantageous as the range of 300Hz and 2500 Hz. In terms of both dimensions and resonance tuning, the second and third modes of the designs do not fall within this range. Hence, it is decided to cover range of 2500Hz and 6kHz with single regular cantilevers. After deciding to work with the regular thin film sputtered PZT cantilevers, it is tried to optimize the output of them. In order to maximize the output voltage, one PZT layer is divided into two equal layers and serially connected which is presented in Figure 3.17. FRF results of them are presented in Figure 3.18. It can be seen that with this configuration, output voltage is almost doubled.

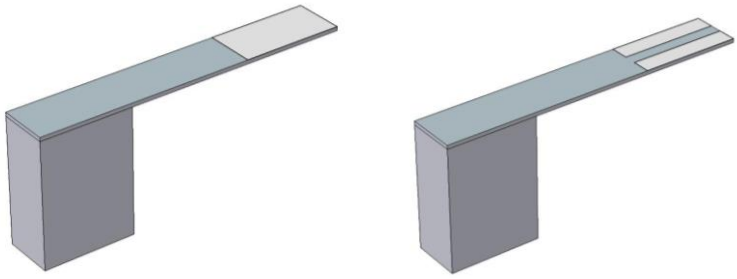

Figure 3.17. At left single PZT layer regular cantilever; at right double PZT layer regular cantilever

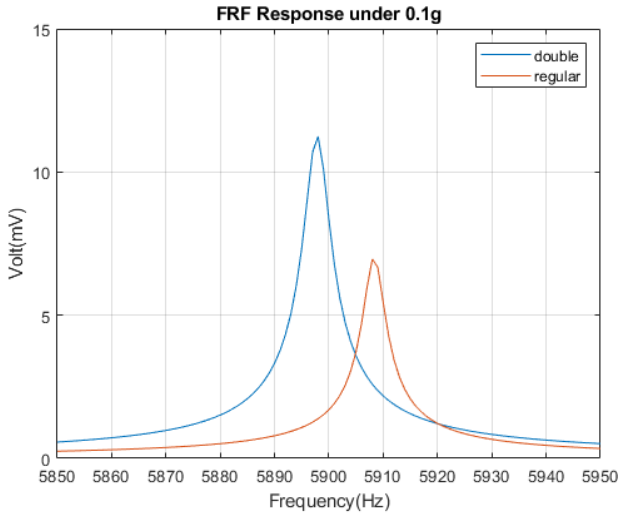

Figure 3.18.FRF results of regular single cantilever and double layer on

The same meshing methodology is followed for regular single dof with double layer and single layer PZT, and multi-dof M-shape. As explained, in order to optimize the output voltage at high frequencies, PZT layers on the regular-single cantilevers are divided into two and PZT layers are serially connected which is presented in Figure 3.19a with zoomed-up meshed views and stress distribution on the beam is shown in Figure 3.19b.

a)

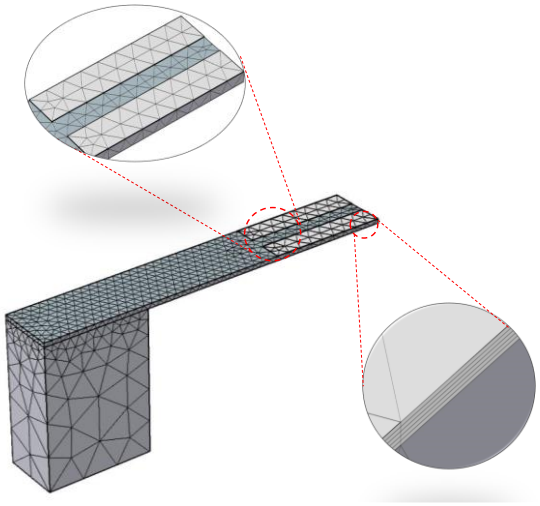

b)

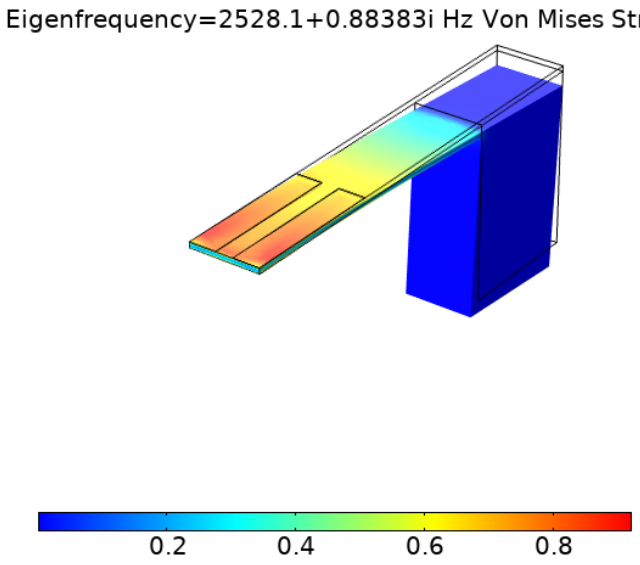

Figure 3.19. Regular-single cantilever with two serially connected PZT layer. a) Top closed view for serially connected PZT layers; bottom closed view for swept meshed PZT layer b) Von Mises stress distribution for the first bending mode

3.2.4 Final Design Parameters

In previous chapters, requirements, criteria, followed optimization, and design methodology is explained. Hence, it is decided that the optimized number of cantilevers in order to cover the decided audible range of 300Hz and 6 kHz is composed of 4 M-shape multi-mode cantilevers which are used for covering up to 2500 Hz and 11 single regular cantilevers for covering between 2500 Hz and 6kHz. Smallest width size of the beams is 137.5µm and largest width of the design is 200µm. Overall footprint of the design is 4.62mm to 4.20mm. It weighs 3.62 mg without the frame. The layout of the device is presented in Figure 3.20.

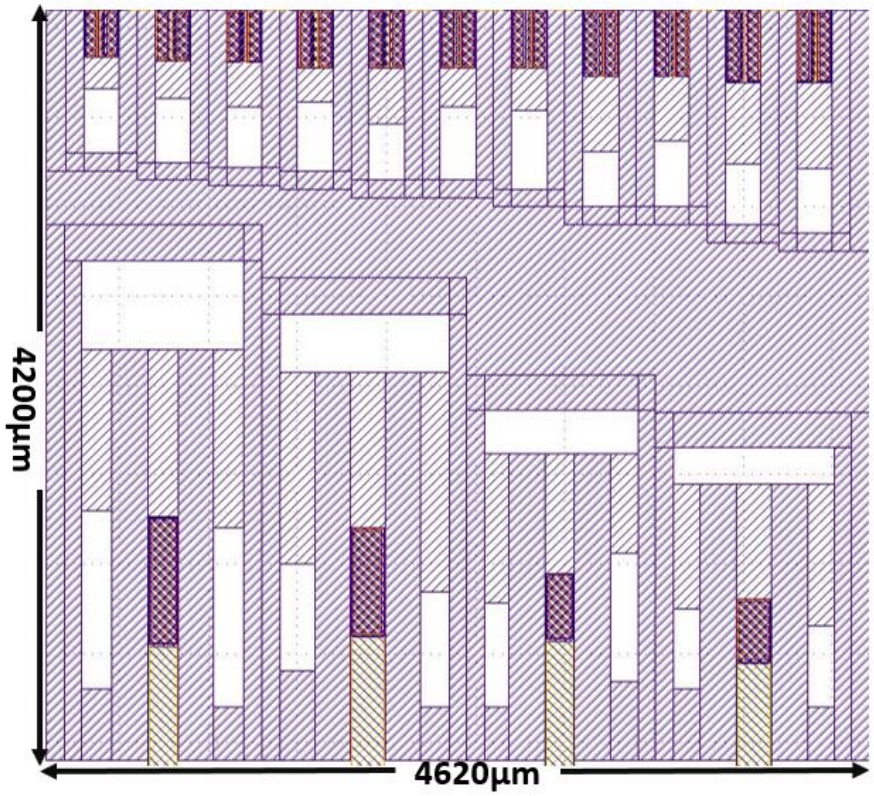

Figure 3.20. Layout of the M-shape device

3.3 Summary

In this chapter, a MEMS-based piezoelectric sensor for fully implantable cochlear implants is developed. Firstly, requirements and criteria are examined. Material selections are conducted. As piezoelectric material, 1μm pulsed laser deposited PZT is preferred. Device thickness and handle layer thickness are decided as 15μm and 500μm respectively. After all, designs are modeled in order to cover the range of 300Hz and 6kHz. Multi-mode designs are selected because of their advantages of bringing multi-resonances at the same footprint compared to single-mode ones. For the studied frequency range, it is observed that M-shape cantilevers are advantageous at low frequencies; thus, high frequencies (above 2.5kHz) are covered with regular cantilevers. In order to increase the performance of the regular cantilevers, double PZT layers are used in a serial connection. To sum up, M-shape cantilevers combined with serially connected regular cantilevers are decided as the final model after FEM simulations. Resonances and responses of the cantilevers are tuned via the FEM software, COMSOL.

CHAPTER 4

Fabrication of Thin Film Multi-Mode Sensor

In the previous chapter, multi-mode design possibilities and finalized shapes of the design are discussed. Based on the decided parameters and finalized design features, fabrication of the devices is executed. For this purpose, first of all layout of the devices is drawn. Then based on the layouts, fabrication process is started after the photomasks are ready. In Figure 4.1, wafer image after front side DRIE is presented.

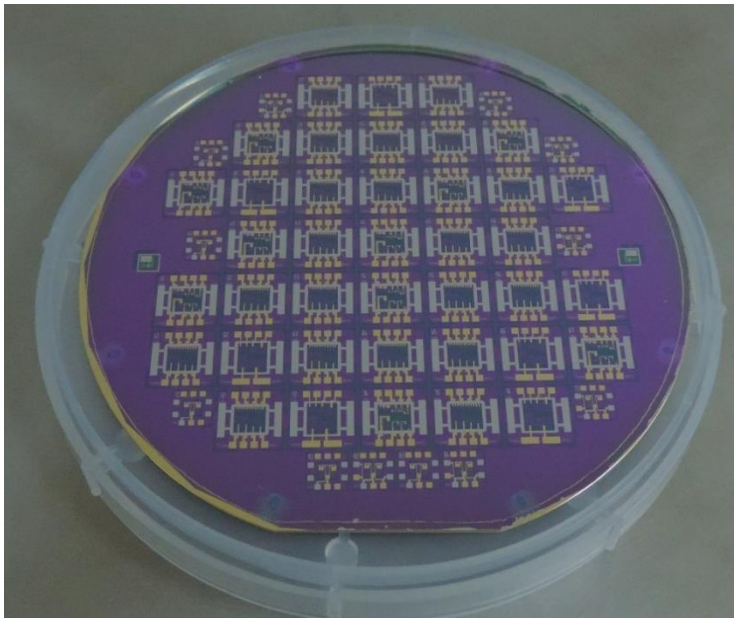

Figure 4.1. Wafer after front side DRIE

As material selection, pulsed laser deposited thin film PZT is preferred on a 4-inch SOI wafer which has a 15μm device layer and 500μm handle layer with a 1μm buried oxide. Process flow is composed of 6 masks which includes bottom electrode patterning, top electrode patterning, PZT patterning, isolation layer patterning, beam, and mass formation. The main challenge of the fabrication of this design is small features compared to previously fabricated designs in BioMEMS group. The minimum beam width is about 137.5μm. There is 2.5μm spacing margin between

bottom electrode and PZT layer, PZT layer and top electrode; and there is 7.5µm spacing between insulation layer and top electrode layer. Thus, most critical tolerance is 7.5µm due to prevent short circuit possibility; however, for accurate fabrication tolerance limitation is taken as 2.5µm. In Figure 4.2 fabrication flow of the sensors is presented step by step. In this chapter, detailed fabrication flow and explanation of each step is explained.

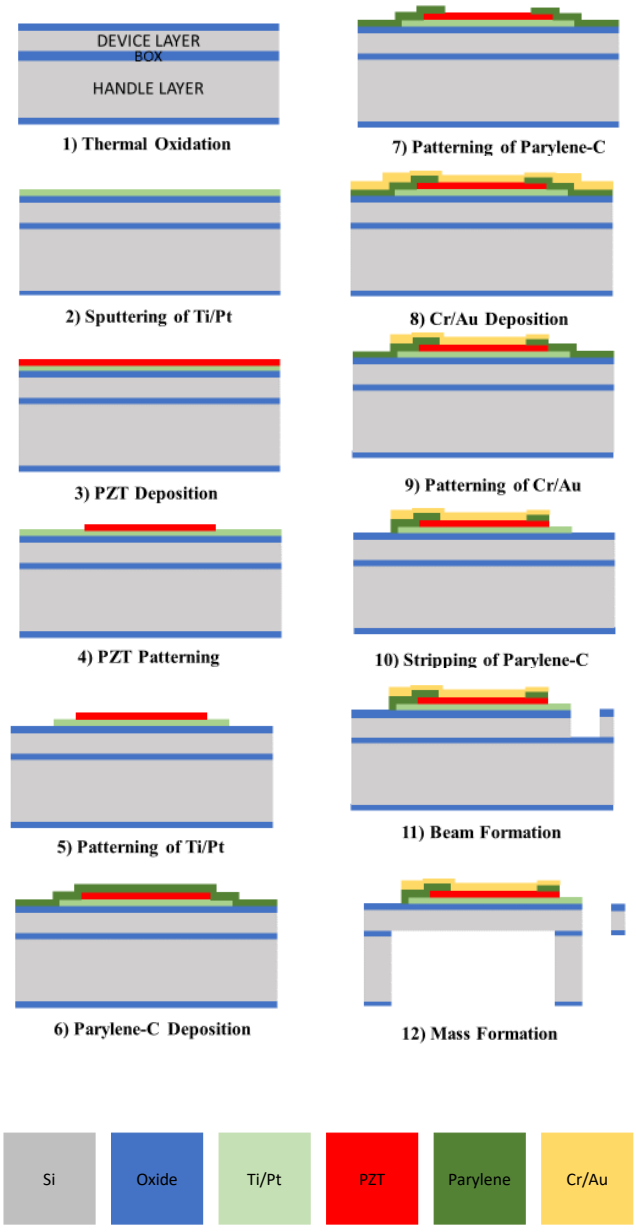

Figure 4.2. Fabrication Flow

4.1 Thermal Oxidation

An isolation layer, in this case thermal oxide, is applied to the top and bottom sides of the 4-inch SOI wafer. Porosity of the PECVD oxide is almost 5 times higher than the thermal oxide layer; moreover, surface roughness of the thermally grown oxide layer is better than PECVD oxide layer [81]. Therefore, 500 nm thermally grown oxide layer is deposited in order to prevent any connection between conductive silicon layer and electrodes, i.e., provide isolation between silicon and electrodes.

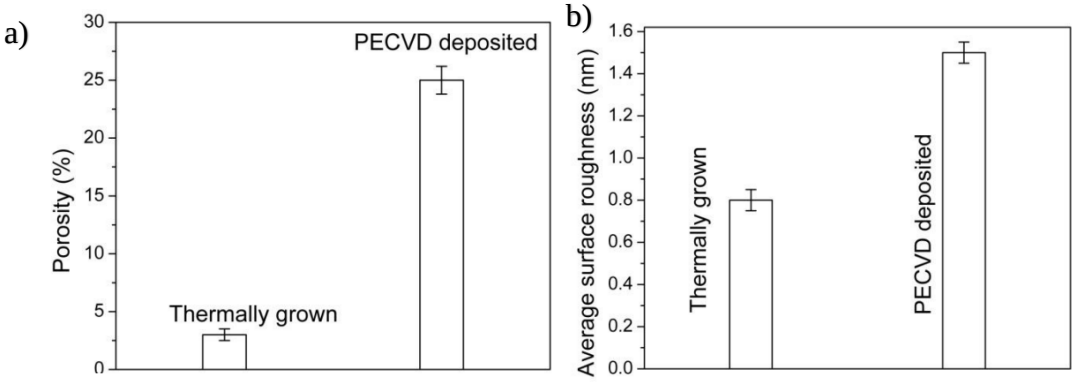

Figure 4.3. a) Porosity percentages of thermally grown and PECVD oxides [81]
b) Average surface roughness of thermally grown and PECVD oxides [81]

4.2 Sputtering of Bottom Electrode Layer

After oxide layer for insulation, bottom electrode of the sensor is formed. As bottom electrode layer, 100nm platinum (Pt) is selected due to its durability up to high temperatures and its inert nature in the oxygen-based environment. Addition to the platinum, 10nm titanium (Ti) is used for providing adhesive layer for platinum. Ti/Pt based bottom electrode also creates a good base layer for pulsed laser deposited thin film PZT. In order to create the bottom electrode layer, sputtering methodology of the microfabrication is followed.

4.3 Thin Film PZT Deposition and Patterning

As piezoelectric layer, 1μm thickness thin film pulsed laser deposited lead zirconate titanate (PZT) is preferred. The deposition is conducted by MESA+ Nano Lab's cleanroom (University of Twente, The Netherlands) at SOLMATE's PLD area. Details of the PZT layer is explained in previous chapter at the material selection part.

After the deposition of the PZT layer is completed, patterning of the PZT layer; thus, first lithography process is started. Following steps are conducted:

- First of all, dehydration at the hot plate is conducted for 5minutes.
- Photoresist of SPR 220-3 is spin coated at 3000 rpm.
- Soft bake of the resist is done at the hot plate for 3.5 minutes. At 115°C.
- UV expose of the wafer is done for 4.5 seconds under soft contact with clear field mask.
- Development is conducted with MF-24A solution for 50 seconds.
- Finally, hard bake is done for 45 minutes at 120°C.

After lithography of the wafer is done, patterning of the PZT layer is done. For this purpose, PZT etchant and PZT cleaning solutions are used. According to the provided recipe from Solmates BV, etch of the PZT is completed. At the final step, in order to clean any residue descum-oxygen plasma for 3 minutes is conducted. In Figure 4.4, images of the devices after PZT patterning are presented.

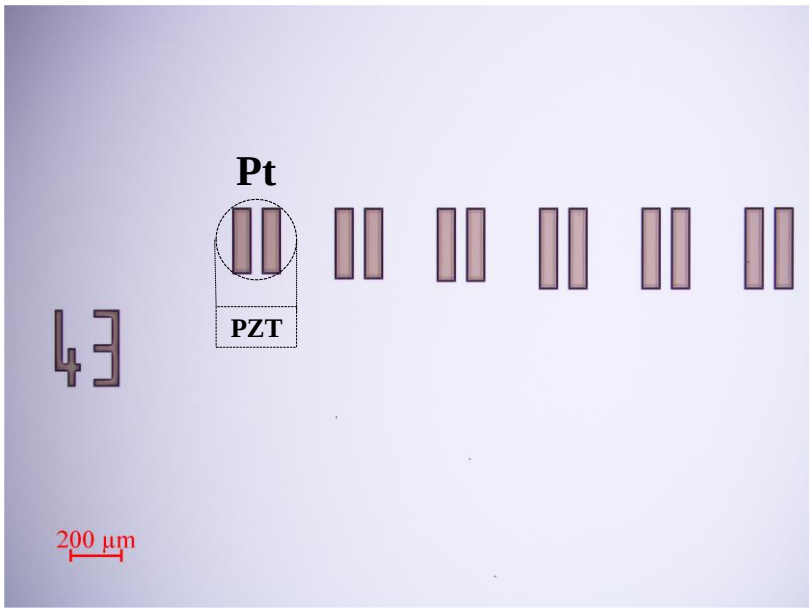

Figure 4.4. Image of the wafer after PZT patterning under microscope.

4.4 Patterning of Bottom Electrode

After PZT patterning, second lithography of the fabrication is done for bottom electrode. Following steps are conducted:

- First of all, dehydration at the hot plate is conducted for 5minutes.
- 7 µm thickness positive photoresist of SPR 220-7 is spin coated at 3000 rpm.
- Soft bake of the resist is done at the hot plate for 3.5 minutes at 115°C.
- UV expose of the wafer is done for 25 seconds under soft contact with clear field mask.
- Development is conducted with MF-24A solution for 75 seconds.
- Finally, hard bake is done for 45 minutes at 120°C.

Patterning of bottom electrode is previously studied and optimized by Koyuncuoglu et.al [82]. In this step, relatively thicker resist is preferred in order to protect the PZT layer during the etching of the Pt/Ti layer. After the lithography completed, patterning process is started. In this process, first of all inverse sputtering is done in order to facilitate wet etch. Then, wet etching of the Pt and Ti layers are conducted.

- In order to etch the Pt layer, Aqua Regia solution is prepared, and it is heated up to 60°C.
- Pt etching is taking about 3 minutes; after completing the Pt etch, wafer is rinsed and dried.
- Secondly, Ti etch is started. In order to etch Ti, H_2O_2: HF: DI water solution is prepared.
- Etch of the Ti is lasted for about 50 seconds. Then, wafer is rinsed and dried.

As final step to this part, residues are purified with descum-oxygen plasma for 2 minutes. In Figure 4.5, images of the devices after Pt/Ti patterning are presented.

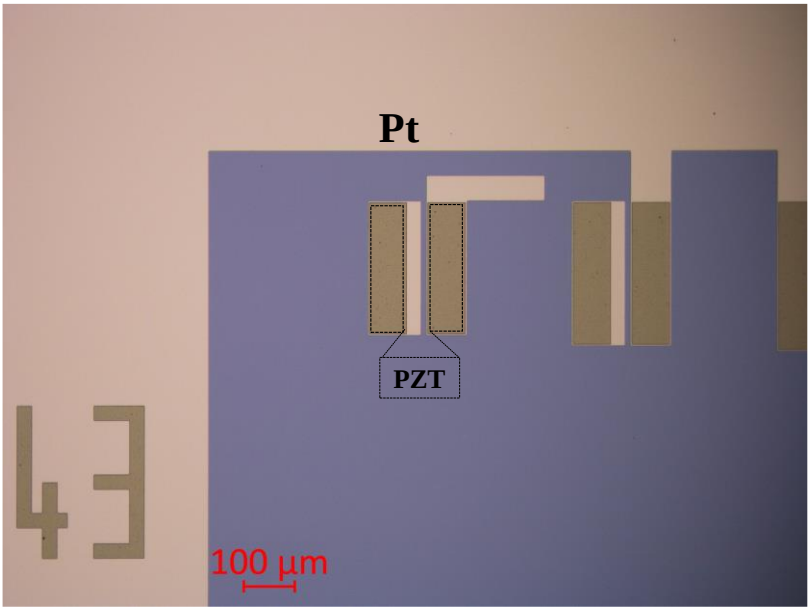

Figure 4.5. Image of the wafer after Pt/Ti patterning under microscope.

4.5 Parylene-C Deposition and Patterning

In previous steps, bottom electrode and PZT layer deposition and patterning is explained. After them, an insulation layer should be deposited before top electrode deposited in order to prevent any possibility of short circuit. Various possibilities as an insulation layer can be preferred such as SiO_2, Si_3N_4 or Parylene-C. Among

them Parylene-C comes forward due to its biocompatible nature; thus, it is preferred as an insulation layer.

For deposition of the Parylene-C, SCS PDS2010 device is used. In order to obtain 1μm of insulation layer, 2.28g Parylene-C dimer is used.

After deposition of the insulation layer, third lithography process of the fabrication is started. Steps are as follows:

- Dehydration at the hot plate is conducted for 10minutes at 95°C.
- Positive photoresist of SPR 220-3 is spin coated at 2000 rpm.
- Soft bake of the resist is done at the hot plate for 5 minutes at 95°C.
- UV expose of the wafer is done for 4.5 seconds under soft contact with dark field mask.
- Development is conducted with MF-24A solution for 40 seconds.
- Finally, hard bake is done for 45 minutes at 95°C.

Before etching of the parylene, descum-oxygen plasma is conducted for 3 minutes to both side of the wafer in order to clean if any residue left. In order to etch and pattern the parylene openings, reactive ion etching (RIE) is preferred. RIE is an anisotropic etching technique that eliminates material in precise directions to create geometric features including sharp edges, smooth surfaces, and deep voids. During the etching process, a patterned resist layer serves as a mask for an underlying substrate such as silicon.

During the RIE etching process, firstly, O_2 cleaning and parylene conditioning is conducted with dummy wafer in order to prepare the environment in the chamber. After preparation, wafer is etched with parylene etch recipe.

At the final step of parylene deposition and patterning step, descum-oxygen plasma is conducted. In Figure 4.6, images of the devices after parylene openings are presented.

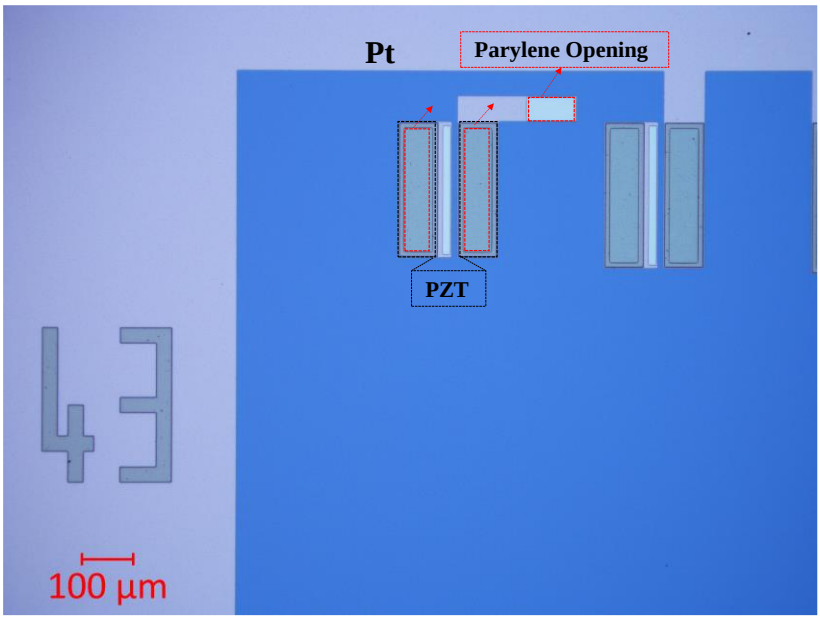

Figure 4.6. Image of the wafer after Parylene patterning under microscope.

4.6 Deposition and Patterning of Top Electrode Layer

As top electrode layer, gold is 400nm gold (Au) is preferred with 40nm chromium (Cr) layer. Cr is used as an adhesion layer for the gold. Relatively thicker metal layer is preferred in top electrode layer. It is the top layer of the overall device; thus, a thicker Au layer than Pt is preferred in order to eliminate the possibility of damage.

In order to deposit the Au/Cr layer sputtering is preferred which is one of the physical vapor deposition techniques (PVD). After deposition of the top electrode layer, fourth lithography of the fabrication is conducted which one's steps are as follows:

- Dehydration of the wafer is conducted at the hot plate at 95°C.
- As a resist (positive), SPR 220-3 is preferred, and it is spin coated at 2000 rpm.
- Soft bake is conducted for 5 minutes at 95°C.
- UV expose of the wafer and mask is conducted at soft contact mode for 4.5 seconds.
- Development about 45 seconds is done with developer solution of MF-24A

- In the final step, hard bake is conducted at 95°C about 45 minutes.

After the hard bake, etching of the top layer is started. For this purpose, before any etch process, descum-oxygen plasma is conducted for 3 minutes to both side of the wafer in order to clean the wafer from any residuals. Then, Au/Cr etching is conducted. For the etching of the top electrode layer wet etchants are preferred. Firstly, Au is etched about 45 seconds in Au etchant; then, again descum-oxygen plasma is conducted for 2 minutes. Secondly, Cr is etched about 30 seconds in Cr etchant; then, again descum-oxygen plasma is conducted for 2 minutes. Finally, due to the rapid diffusion rate of the Au, one more time wafers are immersed into the Au etchant for about 5 seconds, then they are rinsed and dried, and the process is finished. In Figure 4.7, images of the devices after Au/Cr patterning are presented.

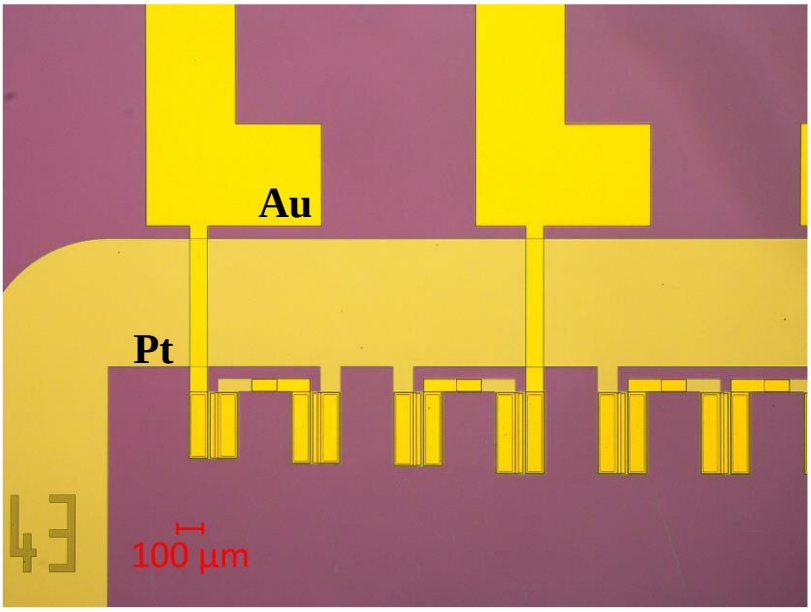

Figure 4.7. Image of the wafer after Au/Cr patterning under microscope.

For wafers with complete top electrode patterning, the remaining parylene on the surface is etched by using top electrode patterns as a mask. Dry etching type process of reactive ion etching (RIE) is preferred for this purpose. Finally, descum-oxygen

plasma is conducted for 3minutes; and the top, bottom, and insulation layer deposition and patterning are completed.

4.7 Front Side Deep Reactive Ion Etching Process: Beam Formation

The top, bottom, insulation, and PZT layer formation and patterning have been completed and the wafers are ready to be processed for beam and mass formation. First, the beam formation process is done. For this purpose, the fifth lithography of the fabrication is conducted as follows:

- Dehydration of the wafers for 5 minutes at 95°C is done.
- Positive resist of SPR 220-3 is spin coated at 2000 rpm.
- Soft bake of the wafers are done at 95°C for 5 minutes.
- UV expose of the wafer and the dark field mask is done at the soft contact mode for 4.5 seconds.
- Development of the wafers are done with MF-24A for 45 seconds.
- Hard bake of the wafers is conducted for 45 minutes at 95°C.

After the lithography process, top thermal oxide etching is conducted with RIE. Then, front side deep reactive ion etching (DRIE) process is started to form beams. Deep RIE is used for this process to form beams with 15μm device layer. The surfaces of the wafers are checked whether any oxide residue is remained or not with Dektak profilometer.

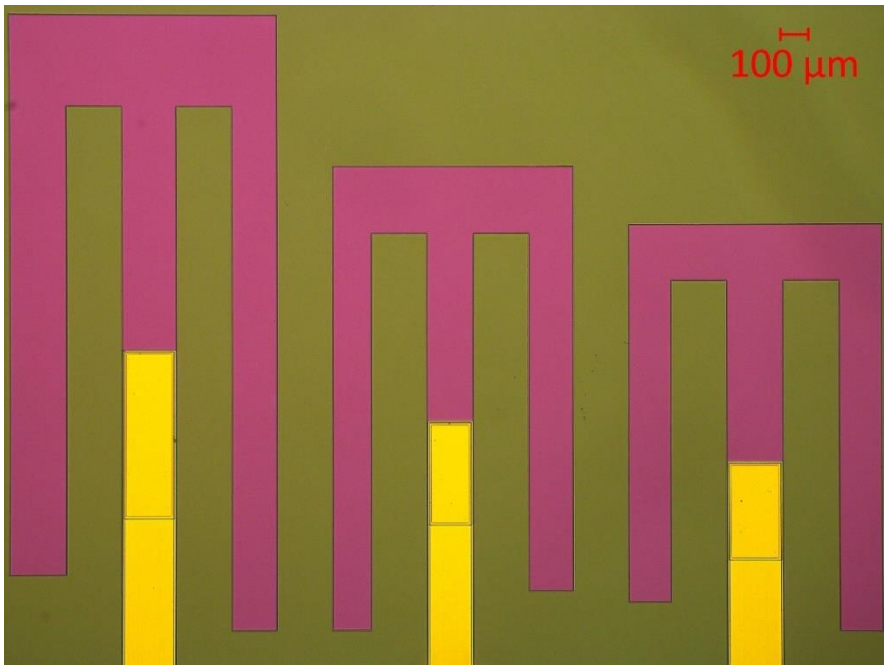

Figure 4.8. Image of the wafer after front side DRIE under microscope

4.8 Back Side Deep Reactive Ion Etching Process: Mass Formation

Final steps of the fabrication are bottom thermal oxide etching, tip mass formation and buried oxide etching with that order. First of all, sixth and final lithography of the fabrication is conducted for back side DRIE. The steps of the final lithography are as follows:

- First of all, dehydration of the wafer at the hot plate at 95°C for 5 minutes is conducted.
- Primer is coated to the front side and then spray coating is done to the front side in order to protect the front side of the wafer during the back side DRIE.
- Hard bake is done at 95°C for 45 minutes.
- Secondly, back side is spin coated with positive resist of SPR 220-3 at 2000 rpm.
- Soft bake is done at the hot plate at 95°C for 5 minutes.

- Then, UV expose of the wafer and the mask (dark field) is done at the soft contact mode for 4.5 seconds.
- Development is conducted at the MF-24A solution for 40 seconds.
- Finally, hard bake is done for 45 minutes at 95°C.

After the lithography process is completed, bottom thermal oxide is etched at the RIE. Then, the handle layer is etched about 500μm from the backside with DRIE according to the patterns by bonding the wafer to the alumina wafer with crystal bond in order to protect the dies that are released. At the final step, buried oxide between cantilevers is etched with RIE. In Figure 4.9, SEM images of the M-shape devices for m-shape cantilevers and serially connected single cantilevers are presented. From the figure, electrode layers, beam and masses of the device can be clearly observed.

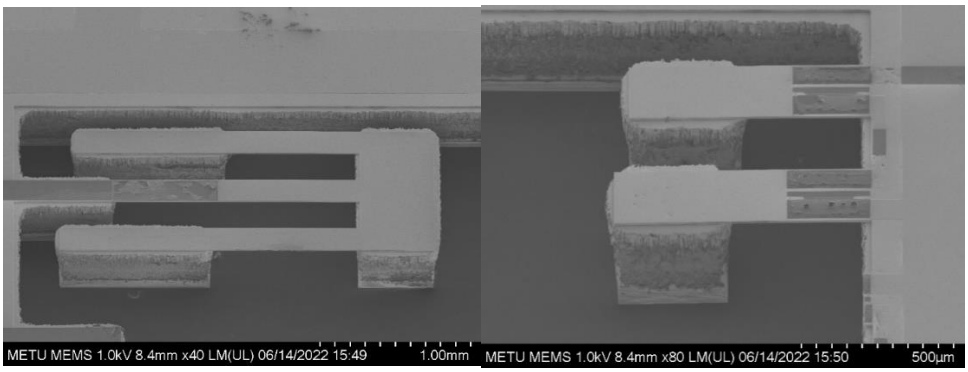

Figure 4.9. SEM images of the M-shape devices. Left: SEM image of the M-shape cantilever; Right: Serially connected single cantilevers

Fabrication is completed with the above explained process. Then, cleaning and dicing of the wafers are conducted. First of all, wafer is separated from alumina wafer. In order to do this, wafer should put into the solvent (such as water, NMP or DMSO) and should be heated up to around ~80°C-90°C. For this purpose, instead of water which has a boiling point of 100°C, dimethyl sulfoxide (DMSO) is preferred which has a boiling point of 189°C. The aim of using DMSO instead of water is to prevent any damage due to the bubble formation during boiling. After wafer is separated from alumina wafer, it is cleaned with acetone and isopropyl alcohol (IPA). Finally, the dried wafer is separated into the dies.

In Figure 4.10, fabricated devices are presented with and without outer frame. Frame can be easily extracted with razors and diamond cutters. After the outer frame is cut out, device has a footprint of 4.6mm×4.2mm×0.5mm which is suitable for the middle ear.

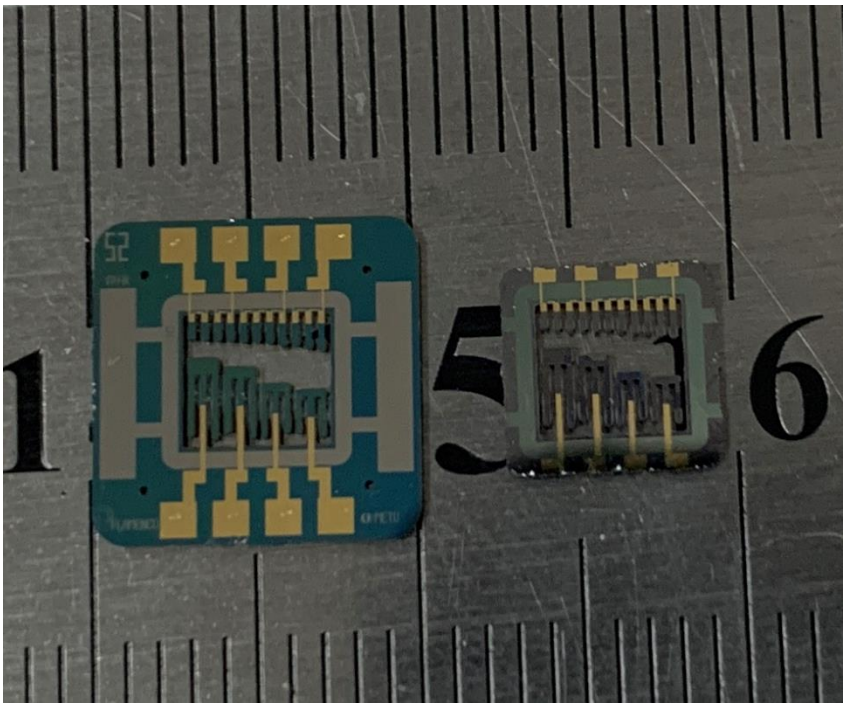

Figure 4.10. Fabricated M-shape devices. Left: With outer frame Right: Without frame

4.9 Summary

In this chapter, fabrication of the devices is explained. Fabrication process of the devices are composed of 6 photolithographic masks. With each mask and patterning, new layer of the device is formed. In devices as bottom electrode layer Ti/Pt; as top electrode layer Cr/Au and as an insulation layer parylene is preferred. Devices are separated with DMSO which has a higher boiling point; thus, damage of bubbles is prevented.

CHAPTER 5

Experimental Verification of The Models

In previous chapters, analytical and FEM modeling of the cantilevers are presented. All design parameters are optimized according to the simulations. Models' verifications are done with experiments. First of all, short-capacitance tests are conducted to verify if there is a signal or not. Secondly, electrical characterization of the devices is done with LCR meter and resonances frequencies are defined. After completing the electrical characterization with LCR, mechanical characterization and piezoelectric responses are examined with shaker table.

5.1 Short Capacitance Test

Initial characterization of the piezoelectric sensors is conducted with a multimeter. Firstly, selected chip is placed into the holder specifically designed for 5mm×5mm devices. Holder is presented in Figure 5.1. Device is placed into the middle part and electrical connections are done with pogo pins which are a type of spring-loaded pin. Overall resonance frequency of the holder mechanism is calculated as around 8kHz which is suitable and out of range of the working range of the sensor; thus, any mechanical filtering effect due to holder is prevented.

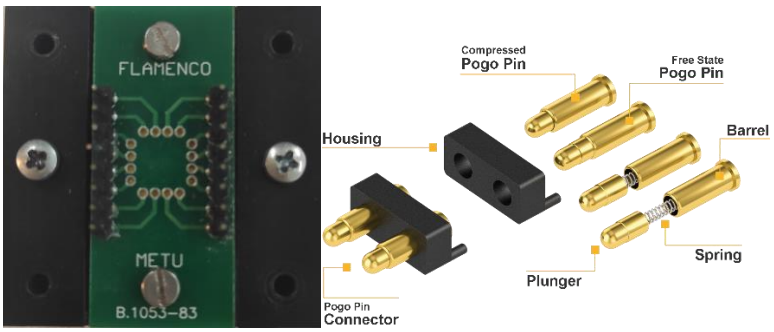

Figure 5.1. Sensor holder

After placing the chip into the holder, via the thin probes of the multimeter, each channels capacitance is checked and whether there is any signal or not can be checked. This test is an initial characterization test before deciding any resonant point or amplitude of the signal, it gives an initial idea about whether the devices are working or not. In Figure 5.2, setup of the experiment is presented.

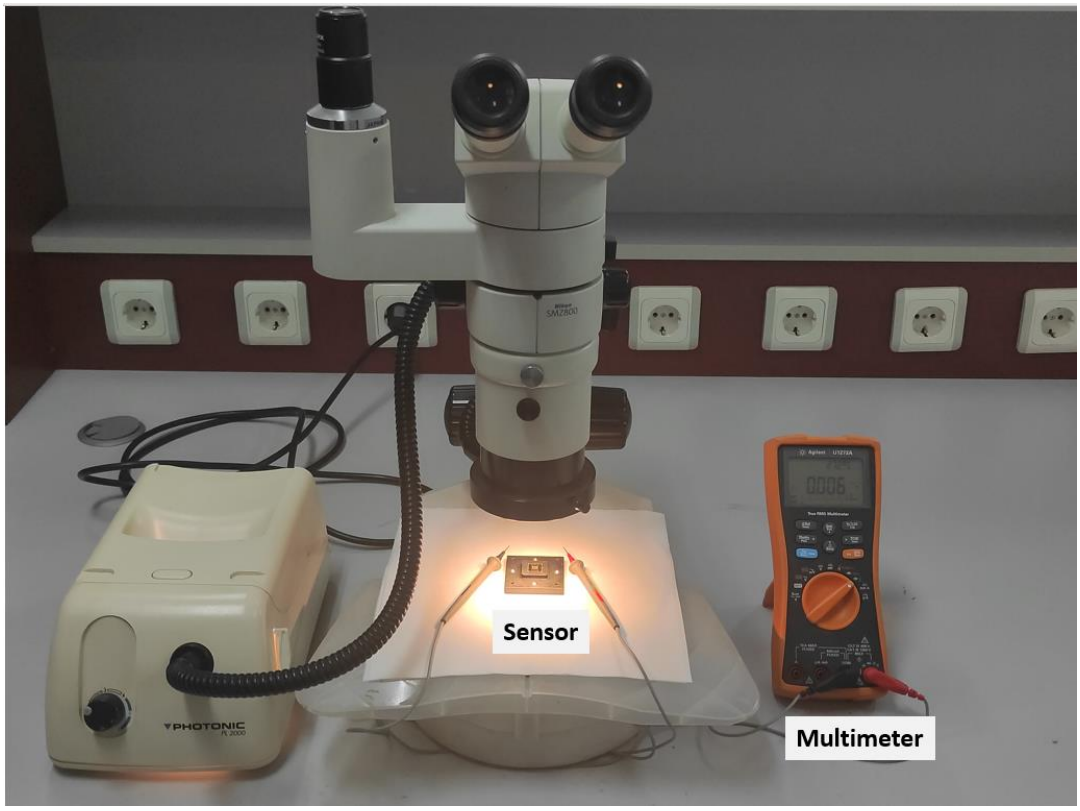

Figure 5.2. Short-capacitance test setup

5.2 Resonance Characterization with LCR Meter

After validation of the working channels is conducted, resonance characteristics of the devices are examined with LCR-meter. Typically, an AC voltage source is used to evaluate the device under test (DUT). The meter monitors the voltage across the DUT as well as the current flowing through it. The meter can determine the magnitude of the impedance based on the ratio of these. The phase angle between voltage and current is also monitored; when combined with the impedance, the

equivalent capacitance or inductance, as well as resistance, of the DUT, is calculated. In Figure 5.3, LCR experiment setup is presented.

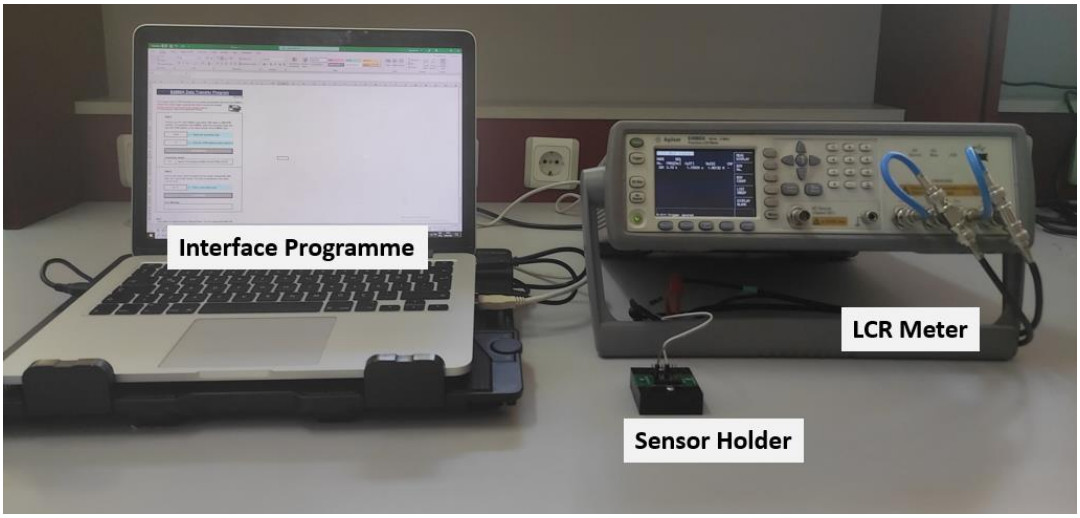

Figure 5.3. Resonance characterization experiment setup

For this experiment, 300mV AC voltage is provided and it is assumed that CR measurements have the elements in parallel. Thus, parallel capacitance and parallel resistance values of the cantilevers are obtained. Measured data is transferred to the Excel macro and can be examined via it. In Figure 5.4, LCR results for the second channel of the M-shape devices are presented. From the figure multi-mode characteristics of the cantilevers can be observed by examining the multiple resonance peaks.

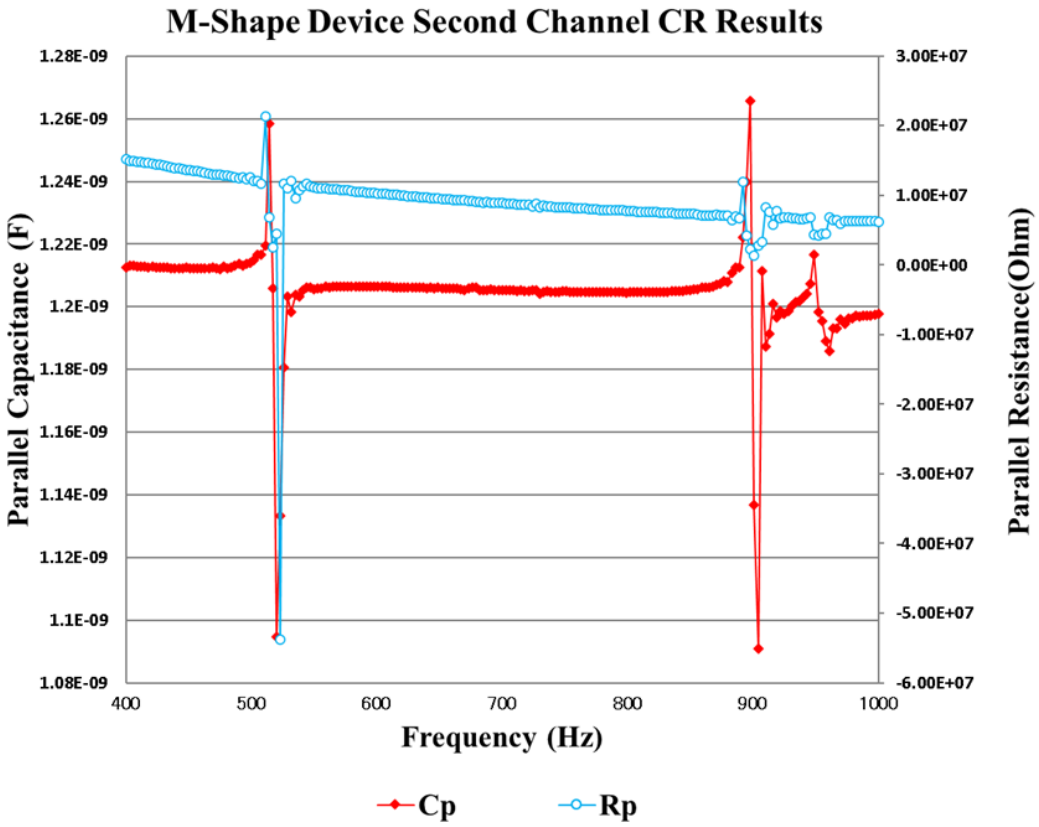

Figure 5.4. Resonance characterization of the second channel of the M-shape device.

5.3 Piezoelectric Sensor Performance Characterization at Shaker Table

In previous parts, resonance characterization and electrical characterization of the multi-mode piezoelectric sensor is explained. After verification of resonance frequencies, performance of the sensor can be examined around the resonances for each cantilever. For this purpose, a setup which can be given mechanical input and in which output can be read as a voltage should be arranged. In Figure 5.5, experimental setup used for performance characterization of the sensor is presented. Experimental setup is composed of shaker table, an accelerometer, controller, amplifier, DAQ, and interface programs of Vibration View and LabView.

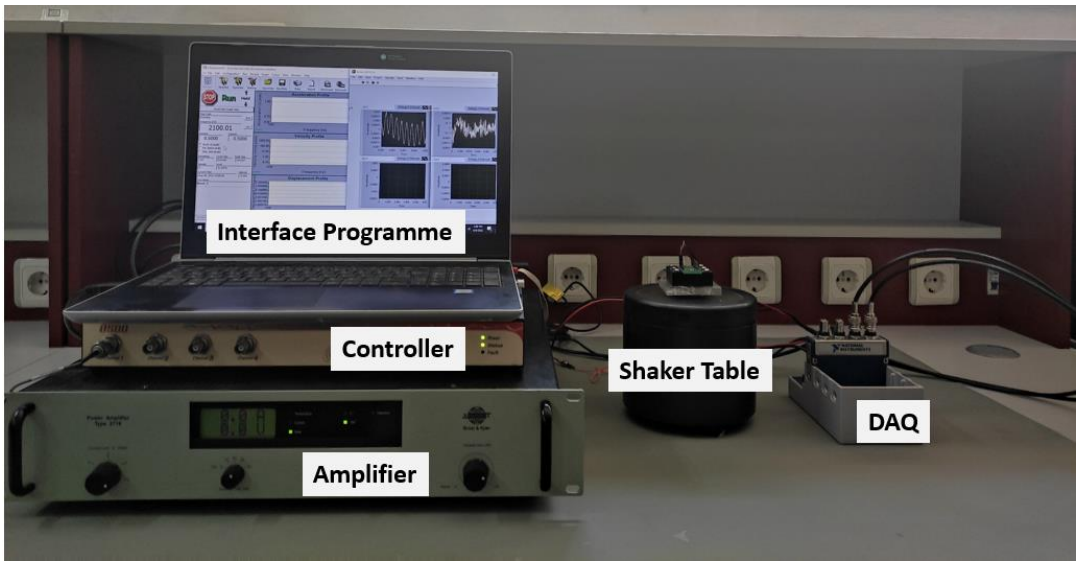

Figure 5.5. Setup configuration of the shaker table experiment

Experiment is executed as follows. Firstly, sensor is placed into the holder and with jumper wires connections are taken from the desired channel. Afterwards, acceleration input is controlled by the interface software of the controller, Vibration View, and the amplifier. Given input is controlled with a closed loop system. From the accelerometer, which is glued on top of the base on the shaker table in which holder is placed, given vibration amplitude data is sent to the interface software, and given control data deviates about 0.1%-0.01%; thus, it can be said that given input is quite stable for conducting a precise experiment. Finally, the output of the sensor is collected with DAQ and sent to the second interface software of the system which is LabView. From LabView, FRF response of the output of the sensor can be obtained as an Excel file. This procedure is followed for each channel for the desired frequency range and desired input acceleration level.

For the coherency between characteristics of the ossicle chain, which is explained in previous chapters, as an acceleration input amplitude 0.1g is decided in simulations. Thus, 0.1g is also preferred acceleration level for this setup in order to make logical comparisons about performance of the sensor based on the simulations and experiments.

In Figure 5.6, experimental and simulation results of the device are presented. For stimulation of the interface circuits, sensor should provide minimum of 100μV signal as explained before. From figures, it can be said that obtained results agree well with the simulation results and all of the channels provide a higher signal than the amplitude of the minimum stimulation signal. Moreover, from figures, multi-mode effect of the cantilevers can also be observed. Each channel is represented with legends and color coding.

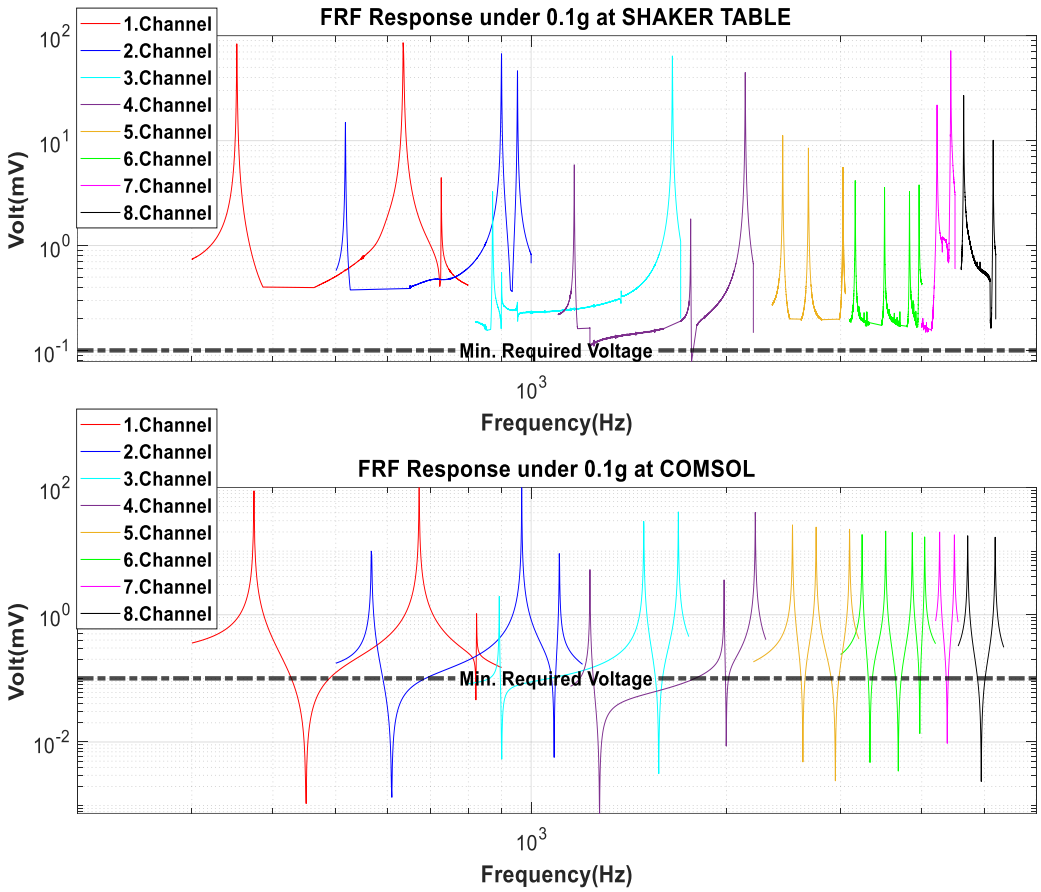

Figure 5.6. FRF results of the M-shape device under 0.1g. Top: Experimental results; Bottom: Simulation results

In Figure 5.7, channel by channel FRF results is presented together with FEM simulations. From Figure 5.7, it is observed that general response of the channels is in agreement with simulations with small deviations.

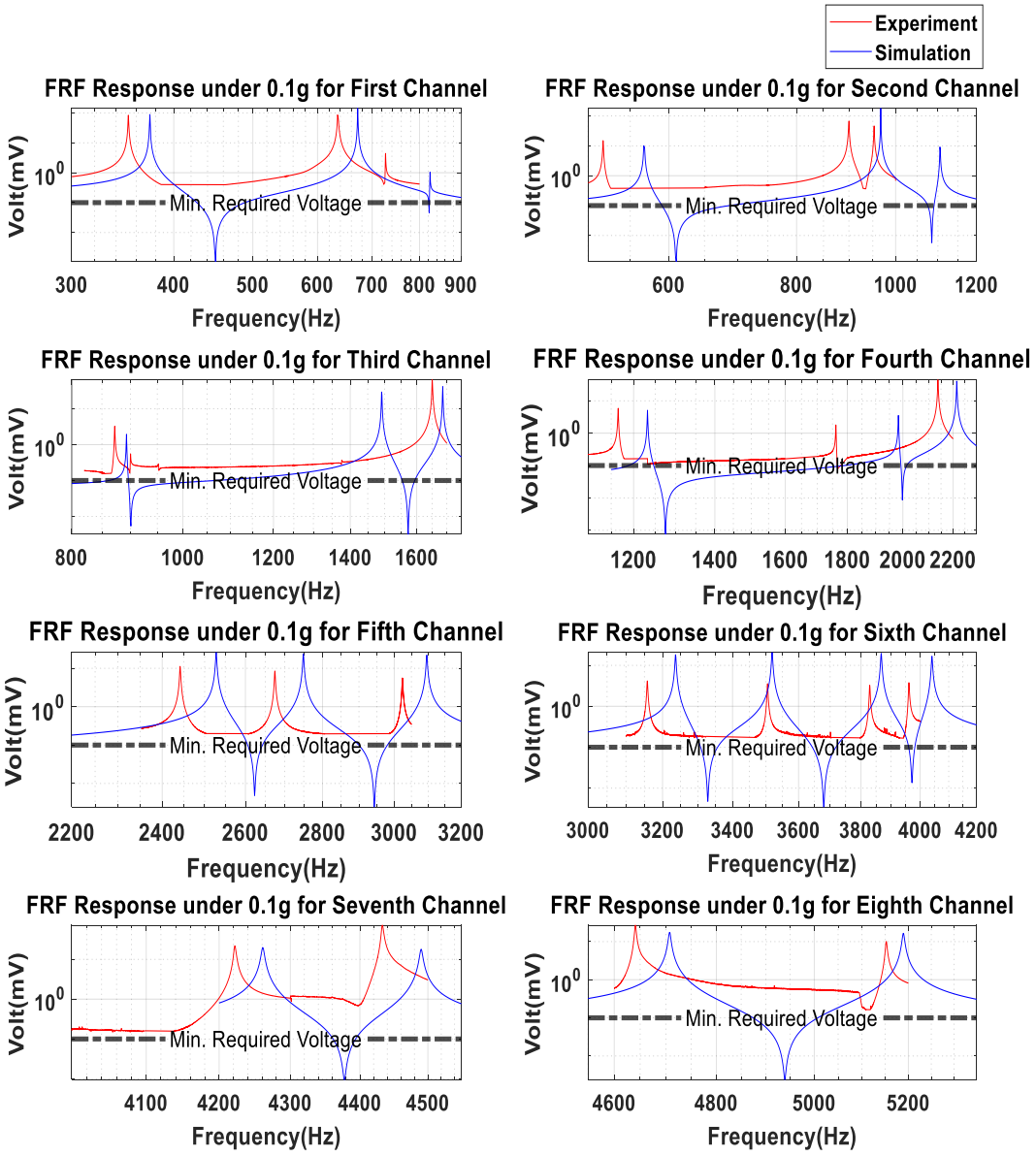

Figure 5.7. Channel by channel FRF results of M-shape devices

Possible reasons for the deviations can be explained by the fabrication and unpredictable damping effects. First of all, the fabrication process of the devices brings so much thermal and mechanical stress due to the nature of the processes.

Hence, the gases and chemicals used in the processes can react with each other and may affect the overall characteristics of the beam under vibration. Secondly, predicting the damping of such a design is especially difficult when the micrometer scale of the system is considered along with the nature of the microfabrication processes causing changes in the system. Also, the effect of the environmental damping during the experiment, such as air damping or damping due to experimental setup, can also not known exactly. Thus, all of these parameters result in deviation in the responses of the cantilevers. Deviation of the resonance frequencies to the lower values is due to the last step of the fabrication process, backside DRIE in which mass formation and release of the beams are conducted. Excess silicon around the masses from this step results in deviations at the resonance frequency locations.

All resonances and piezoelectric voltage values are presented with simulation results in Table 5.1. The maximum deviation of the resonance frequency location from the simulation is %11.7 which is quite a well-agreement, %88.3, between experimental results and FEM simulations. For piezoelectric voltage values, the deviation can vary from low to moderate due to the unpredictable damping effects. First of all, 22 of the 23 resonance frequencies can be clearly observed. For the third channel, one of the resonance frequencies fell behind and its vibration characteristics are slightly different than expected. Although all 23 resonance peaks can be observed from the figures, the second mode of the third channel is neglected in Table 5.1. This different characteristic of the third channel is monitored at all chips on the wafer; thus, it can be said that the reason for this may could some possible fabrication effects.

Table 5.1. FRF results of the M-shape device under 0.1g acceleration level

Channel Number	Experiment		Simulation	
	Frequency (Hz)	**Voltage (mV_{pp})**	**Frequency (Hz)**	**Voltage (mV_{pp})**
1	351	94.4	373	90.0
	635	138.1	672	140.0
	726	4.9	823	1.0
2	517	16.1	567	10.0
	899	74.4	967	170.0
	952	51.1	1105	10.0
3	900	2.1	893	3.0
	1650	69.5	1491	28.0
			1685	40.0
4	1165	6.4	1233	5.0
	1761	6.3	1984	5.0
	2137	39.3	2216	40.0
5	2441	11.2	2528	22.0
	2674	8.5	2753	20.0
	3023	5.6	3099	18.0
6	3157	3.1	3235	16.0
	3504	2.2	3524	19.0
	3828	4.7	3873	16.0
	3960	5.2	4047	13.5
7	4240	9.8	4261	14.5
	4432	5.3	4490	13.5
8	4638	33.1	4707	13.0
	5152	5.8	5189	12.0

The deviations in the resonance frequencies are again quite small and the results are close to each other for all chips. For piezoelectric voltage responses deviations are moderate, and its maximum differ +/- 20 mV for one device to another. In general, deviations of the responses are small for higher frequencies in which single regular cantilevers are used. The maximum deviations in the responses are observed in M-shapes due to their recessed and small geometric structure, which is more vulnerable production processes. To sum up, it can be said that the general experimental responses of the chips on the wafer are both well-coherent with each other and FEM simulations; and, M-shape sensor can sense whole range of 300Hz and 6kHz at 0.1g.

5.3.1 Piezoelectric Sensor Acoustic Performance Characterization

In previous part, performance of the sensor is validated with shaker table experiment under 0.1g acceleration. In this part, characterization of the sensor is tried to examine under acoustical input. As explained before, this sensor is tried to develop for cochlear implants; thus, it is placed at the middle ear and the real input is the vibration of the ossicles or membrane under sound. Therefore, in this characterization, sensor is placed onto the artificial tympanic membrane, and controlled acoustic input is given to the membrane.

Artificial tympanic membrane is previously studied by Ashrafi [83], and her model is verified experimentally. She designed also an acoustic holder in which membrane can be placed. Membrane characteristics is controlled by arranging pre-stress on it and the overall model together with the acoustic holder and membrane is adjusted in a way that characteristics resembles the real membrane. In this experiment, the sensor is placed on the artificial membrane. Thus, in order to take electrical connections from the sensor, a parylene carrier and ZIF connector are used which are previously studied and fabricated by Soydan [84] for his packaging studies of the sensor. In Figure 5.8, the acoustic holder together with the sensor and its connections via parylene carrier and ZIF connector are presented.

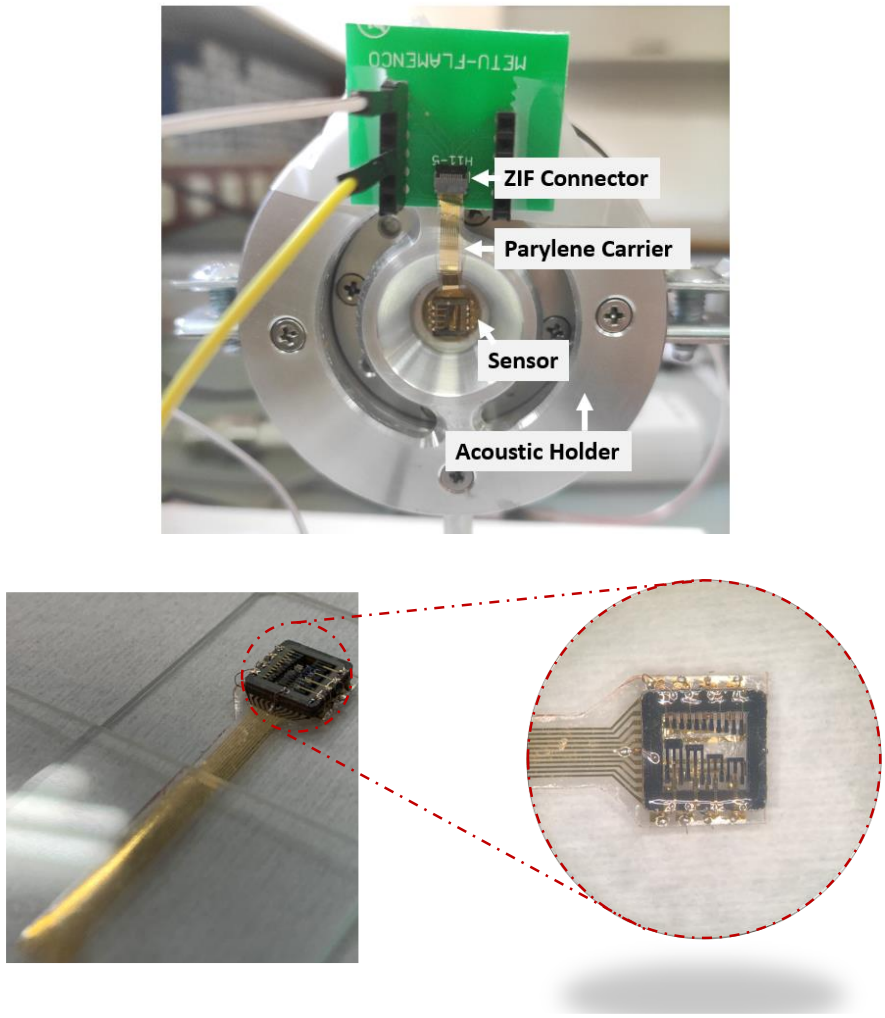

Figure 5.8. Acoustic holder with sensor and parylene carrier

General representation of the acoustic test setup is presented in Figure 5.9. A signal generator together with amplifier is used for providing the signal to the earphone and probe microphones. Given input is controlled with dB meter. ER2 earphone is placed at one side of the membrane and it transforms the provided signal into an acoustic signal. The membrane vibrates due to the acoustic input from the earphone. The membrane under the acoustic input vibrates the sensor. The output of the sensor is collected with DAQ and signals are saved with interface programme of LabVIEW.

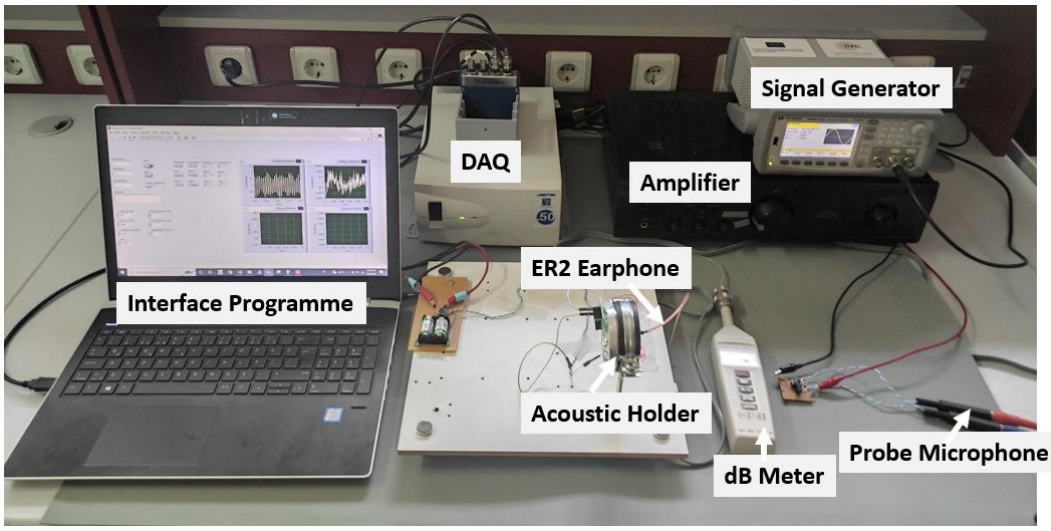

Figure 5.9. Acoustic test setup

The experiment is conducted from 50 dB SPL to 100 dB SPL with an interval of 10dB. Results of the experiment are presented in Figure 5.10. All modes are observed in acoustic characterization. Responses of cantilevers are observed at all SPL levels. Higher than 100dB or lower than 50dB sound pressure levels can also be observed; however, setup upper limitation is around 100dB, and measuring under 50dB is required extremely quiet environments in order to conduct a healthy experiment.

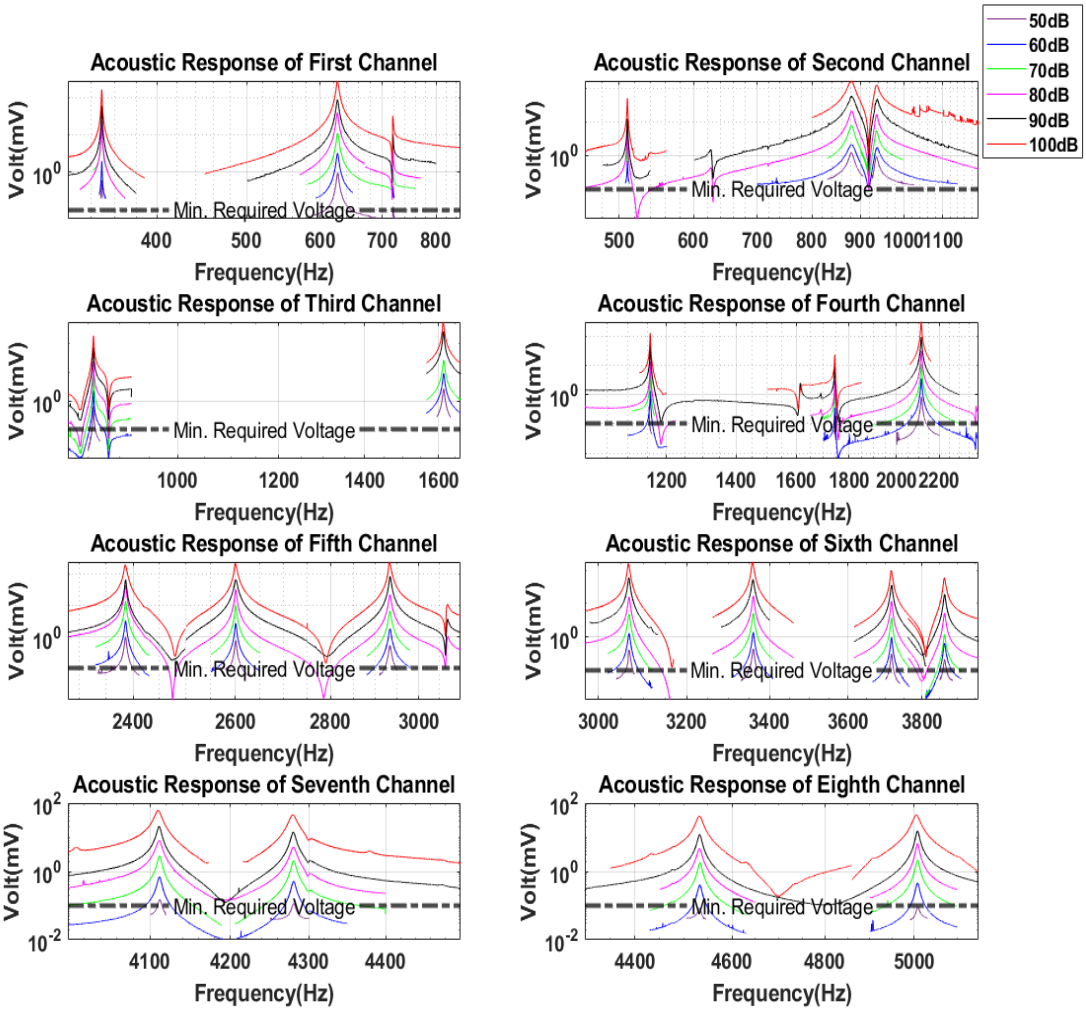

Figure 5.10. Acoustic responses of the device from 50dB SPL to 100dB

In Table 5.2, results of each channel at resonance are presented. Based on the results, it can be observed that even 60dB, all channels provide enough output. Moreover, even 50dB, except few channels, minimum stimulation signal value of 100µV can be seen. Therefore, it can be said that designed sensor can even sense low SPL values, and at higher SPL levels sensor can sense almost all range of 300Hz and 6kHz.

Table 5.2 Acoustic experiment results

Channel Number	Frequency (Hz)	Output Voltage (mV_{pp})					
		100dB	**90dB**	**80dB**	**70dB**	**60dB**	**50dB**
1	348	162.55	60.19	24.40	6.89	1.98	0.61
	626	278.48	86.94	39.18	11.17	3.18	0.95
	718	31.96	10.10	3.66	1.26	0.41	0.12
2	510	50.50	12.41	5.46	1.76	0.69	0.37
	880	167.48	59.83	21.16	7.91	2.10	1.21
	936	125.05	49.18	16.71	5.49	1.71	0.91
3	858	178.83	71.35	23.03	7.49	2.24	0.62
	1613	546.16	252.57	69.70	26.09	8.99	2.63
4	1157	127.81	49.98	13.33	5.90	1.35	0.40
	1743	23.26	10.54	3.07	1.63	0.36	0.10
	2112	310.43	92.08	31.75	10.86	3.60	0.84
5	2384	194.62	65.95	44.11	13.84	3.31	1.02
	2599	215.08	65.34	32.75	10.11	2.69	0.78
	2931	239.68	83.49	21.85	6.74	1.84	0.54
6	3066	157.48	59.08	15.80	4.82	1.28	0.41
	3356	178.43	52.54	16.99	5.17	1.37	0.44
	3715	100.63	36.09	11.79	3.73	0.97	0.31
	3862	59.77	18.94	5.08	1.19	0.65	0.21
7	4109	60.21	20.67	7.88	2.82	0.69	0.15
	4279	45.18	14.01	5.08	2.08	0.51	0.12
8	4532	41.22	12.05	4.65	1.79	0.41	0.09
	5005	44.28	15.31	6.52	2.13	0.46	0.09

5.4 Comparison and Discussion of Multi-Mode M-Shape Design

In this research, main aim is designing a sensor in which whole interval of 300Hz and 6kHz can be covered. For this purpose, 8-channel regular cantilever-based sensor was studied by Yüksel [85] previously. Although his results were promising, bandwidth was narrow. Therefore, alternative designs are examined in this thesis; and, M-shape design is selected as one of the most suitable choice for increasing the performance of the sensor. In Figure 5.11, two designs are presented side-by-side.

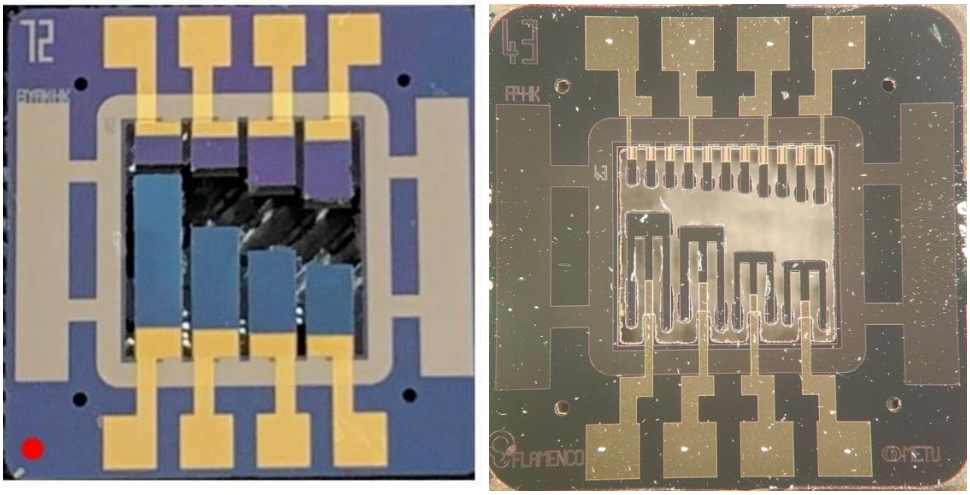

Figure 5.11. Left: 8-channel regular cantilever based piezoelectric sensor [85]
Right: Multi-mode piezoelectric sensor

The previous multi-channel design has a volume of $5\times5\times0.6mm^3$ and it weighs about 4.8mg. The current multi-mode, multi-channel design has a volume of $4.6\times4.2\times0.5mm^3$ and a mass of 3.62mg without the frame. In Figure 5.12, acoustic responses of two designs at 90dB are presented channel by channel. There is a great improvement in the bandwidth of the piezoelectric sensor between the two designs. The covered frequency interval is improved about 5 times with the current design. Also, peak-to-peak voltage amplitudes show a significant increase. Between the two designs, the observed maximum peak-to-peak voltage amplitude is increased 15.5 times, from 16.27 mVpp to 252.57 mVpp for 90dB.

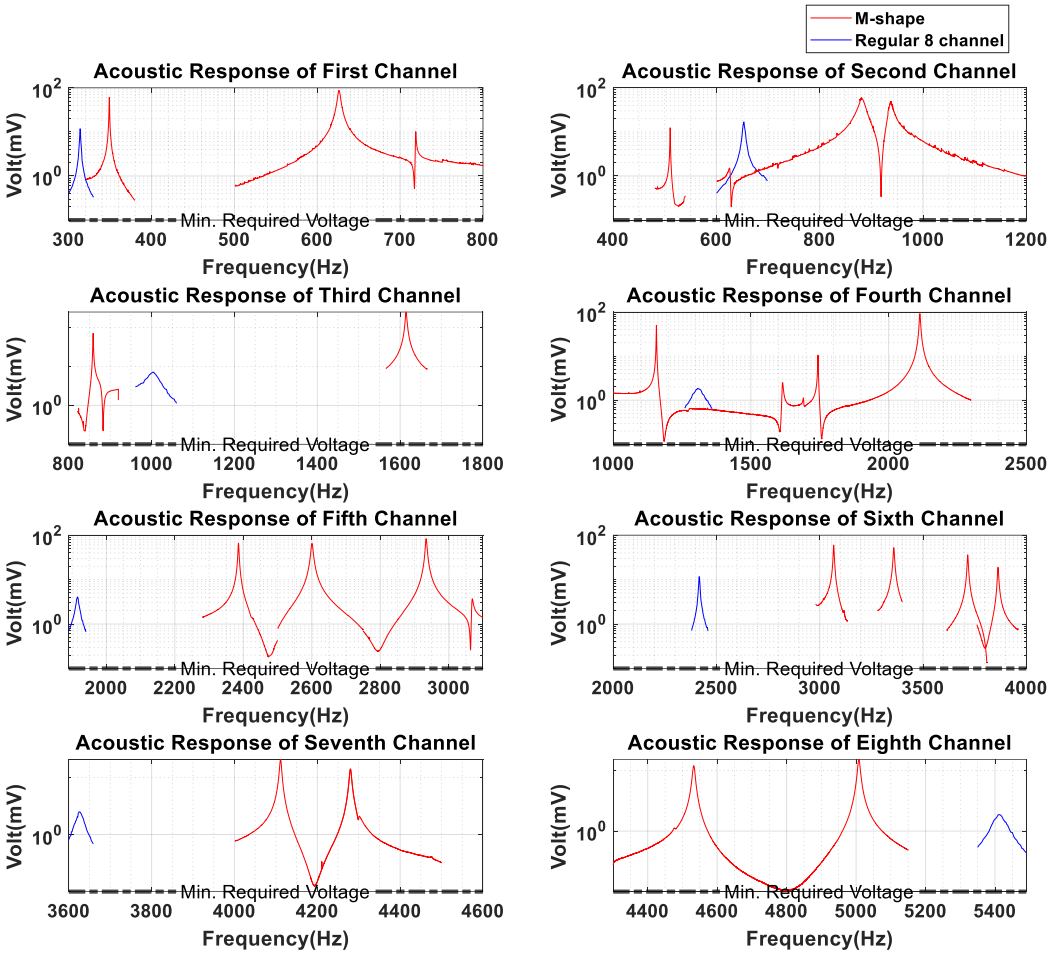

Figure 5.12. Channel by channel previous and current design acoustic responses at 90dB

In Figure 5.13, the overall response of the devices is presented for the whole interval at 90dB. From this Figure, performance difference between the two designs can be clearly observed. Multi-mode, multi-channel sensor design succeeds to improve the bandwidth up to about 5 times. Also, it is %25 lighter than the previous design, and its volume is smaller than the previous design about %35.

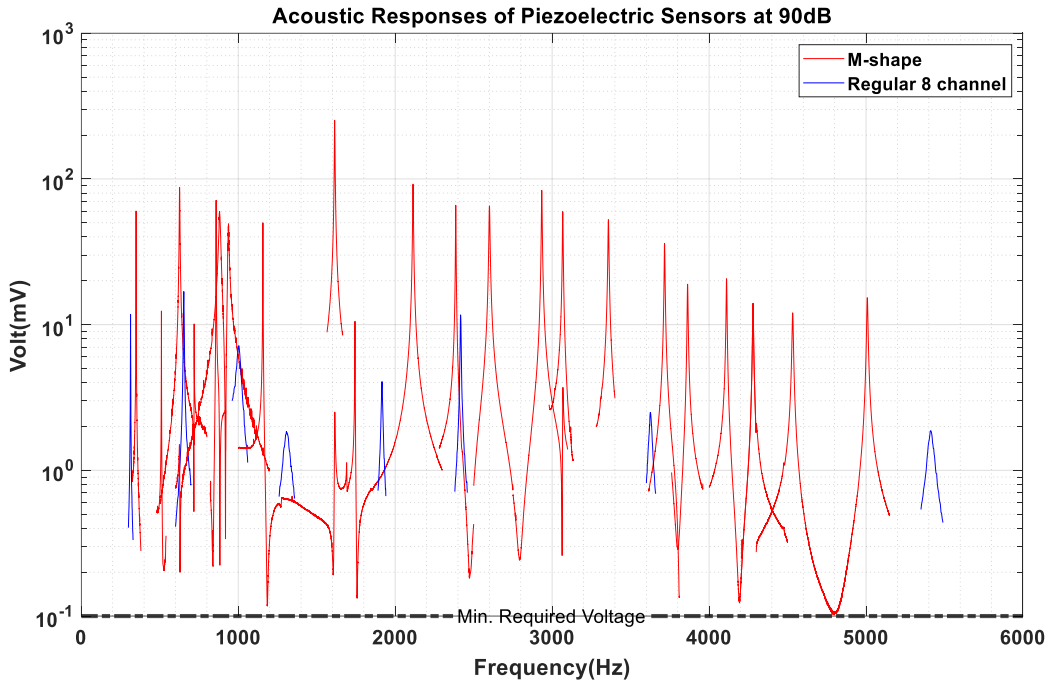

Figure 5.13. Acoustic responses of the M-shape design and previous regular 8 channel design at 90dB

5.5 Summary

This chapter conducts electrical, mechanical, and acoustical characterization of the sensor. First of all, a short capacitance experiment is conducted and the electrodes of the sensor are checked. Later, resonance characterization of the devices is performed with an LCR meter. As the third experiment, sensor's performance over frequency domain is examined with a shaker table at 0.1g acceleration level with a sinusoidal frequency sweep input signal. In this experiment, 138.1 mV_{pp} is observed. Moreover, it is observed that the sensor can sense the whole frequency range for 0.1g acceleration input signal. The last experiment was done under auditory input and with the artificial tympanic membrane in order to create a more resemble environment to the middle ear and observe the more realistic behavior of the sensor. From this experiment, maximum responses of 546.16 mV_{pp}, 252.57 mV_{pp}, and 69.70 mV_{pp} are monitored, respectively for 100dB, 90dB, and 80 dB. Finally, multi-mode

device is compared with the previous design. It is seen that bandwidth is increased about 5 times with the current multi-mode design which is lighter and smaller than the previous one. In addition to this, there is about a 15 times increase between peak-to-peak voltage values.

CHAPTER 6

Alternative Design Approaches

In this chapter, alternative design approaches to M-shape multi-mode sensor design are examined. Possible design configurations are modeled and simulated. FRF responses of the devices are examined. Experimental verification of the fabricated devices is done.

6.1 Alternative Design: P-Shape

Multi-mode designs are widely examined for broadening bandwidth and output range. Spiral-based designs are one of the popular multi-mode design possibilities. Nabavi et. al (2017) [86] proposed thin film AlN symmetric-spiral shaped MEMS-based piezoelectric harvester. According to his results which are presented in Figure 6.1. The suggested wideband energy harvester's form in each mode is shown. The energy harvester has a distinct shape in each mode, which aids in driving the harvester in various modes to generate the broadband aspect.

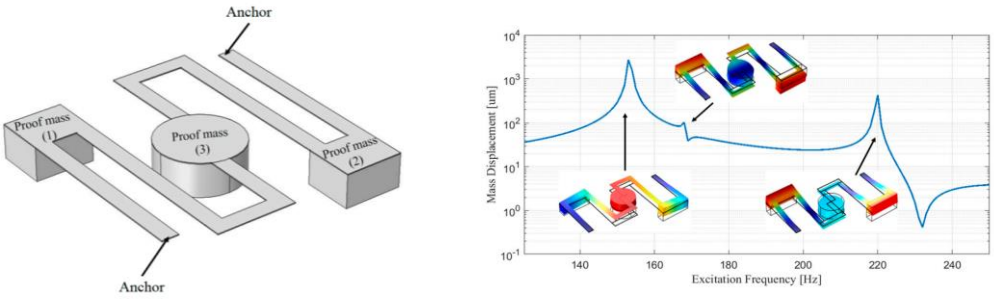

Figure 6.1. Symmetrical multi-mode piezoelectric energy harvester FRF results in terms of displacement [86]

One of the other research projects about spiral designs belong to Udvardi et al. (2017) [87] in which they implemented the design as fully implantable hearing system. In Figure 6.2, their layout and shaker table results for 1g are presented. They tried to fulfill the microphones duty with MEMS-based cantilever arrays with AlN as piezo layer. They proposed 12 channel system. Also, they put just one big mass into the middle of the spiral. Their one spiral cantilever has a footprint of 2mm to 2mm which is not small enough to place in ear; thus, they claimed that with a compact packaging dimensional constraints for the ear can be satisfied.

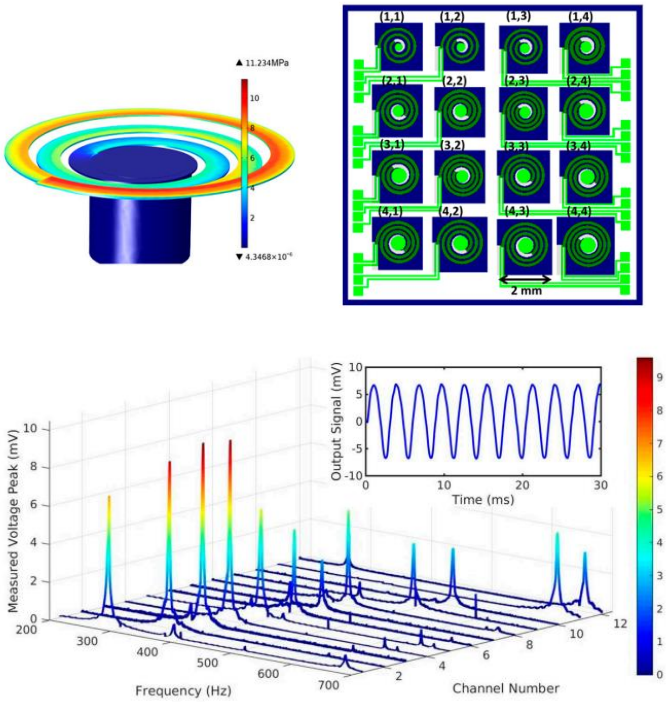

Figure 6.2. Top: Spiral shaped one-dof cantilever and its array configuration
Bottom: Shaker table results of the device under 1g [87]

Inspired from previous studies, an alternative solution is proposed in this section. The proposed design is presented in Figure 6.3. Initial idea for the design is modelling a 3 turn, 3 mass design with 3 PZT layer with features around 200μm and implementing models in an array configuration. Although theoretically stress distributions did not exceed yield points of neither PZT nor silicon; in terms of optimized fabrication, 3 turn devices is not feasible due to excessive thermal and

mechanical stress during fabrication which makes the devices fragile and makes it harder to release them without excessive buckling and damage. Therefore, the model is updated as 2 turns, 2 masses with 2 PZT layers under the limits of fabrication and stress considerations.

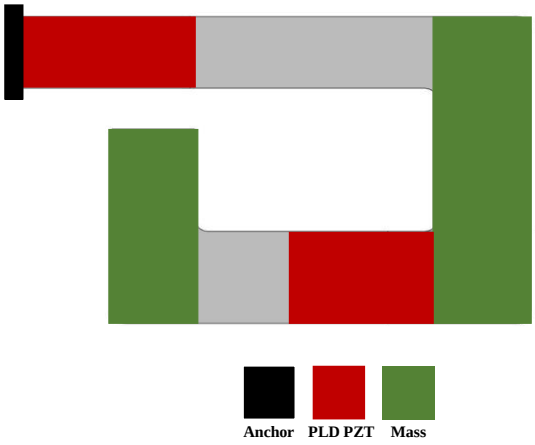

Figure 6.3. P-shaped multi-mode design

Cross-calibration methodology is followed for further examination. It is obtained that for high frequencies double-serially connected PZT layer sputtered single cantilevers are much efficient than multi-dof P-shape cantilevers.

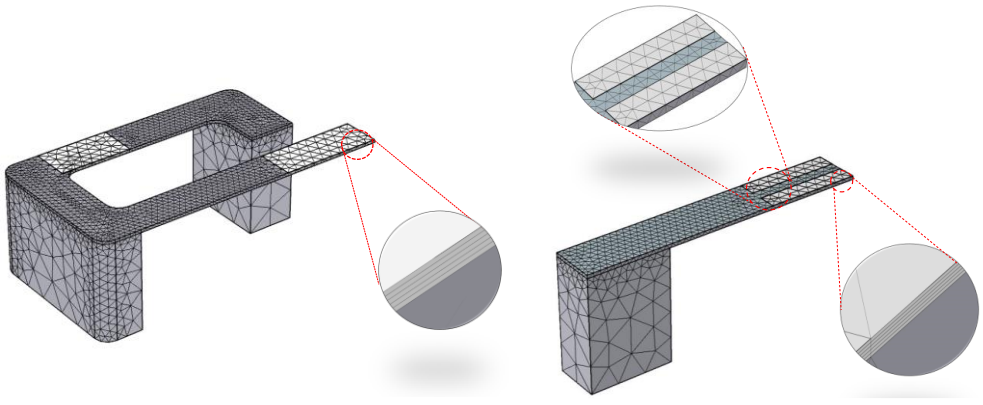

Figure 6.4. Meshed images of the P-shape cantilever and double PZT regular cantilever with zoomed views of PZT layers

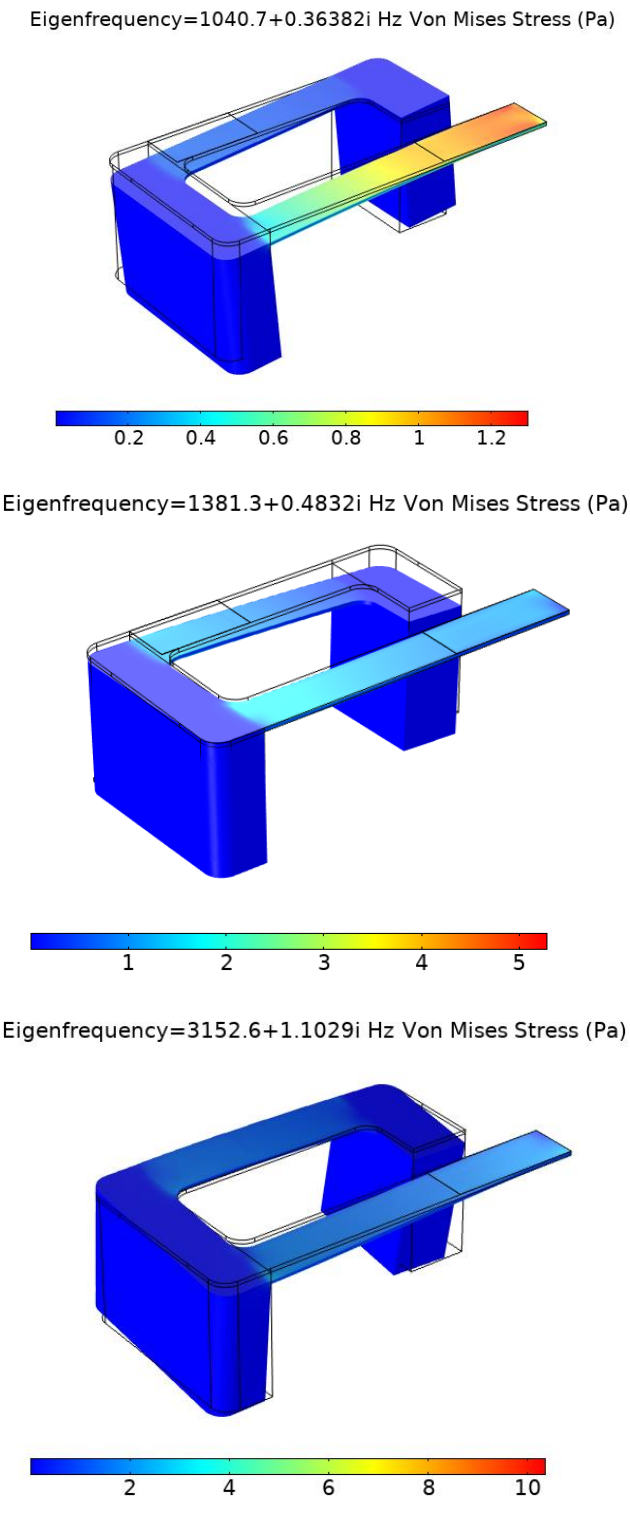

Figure 6.5. Von Mises stress distribution for the first three mode of P-shape cantilever

6.1.1 Final Design Parameters

According to the requirements and limitations, the multi-mode P-shaped design is finalized. Resonance frequencies and amplitude of output voltage are tuned with cross-calibration by arranging dimensions. It is decided that 6 multi-mode P-shape designs together with 4 regular single cantilevers can cover a major part of the range of 300Hz and 6kHz. The smallest width size of the beams is 150μm and the largest width of the design is 600μm. The overall footprint of the design is 4.80mm to 4.25mm. It weighs 3.57 mg without the frame. The layout of the device is presented in Figure 6.6.

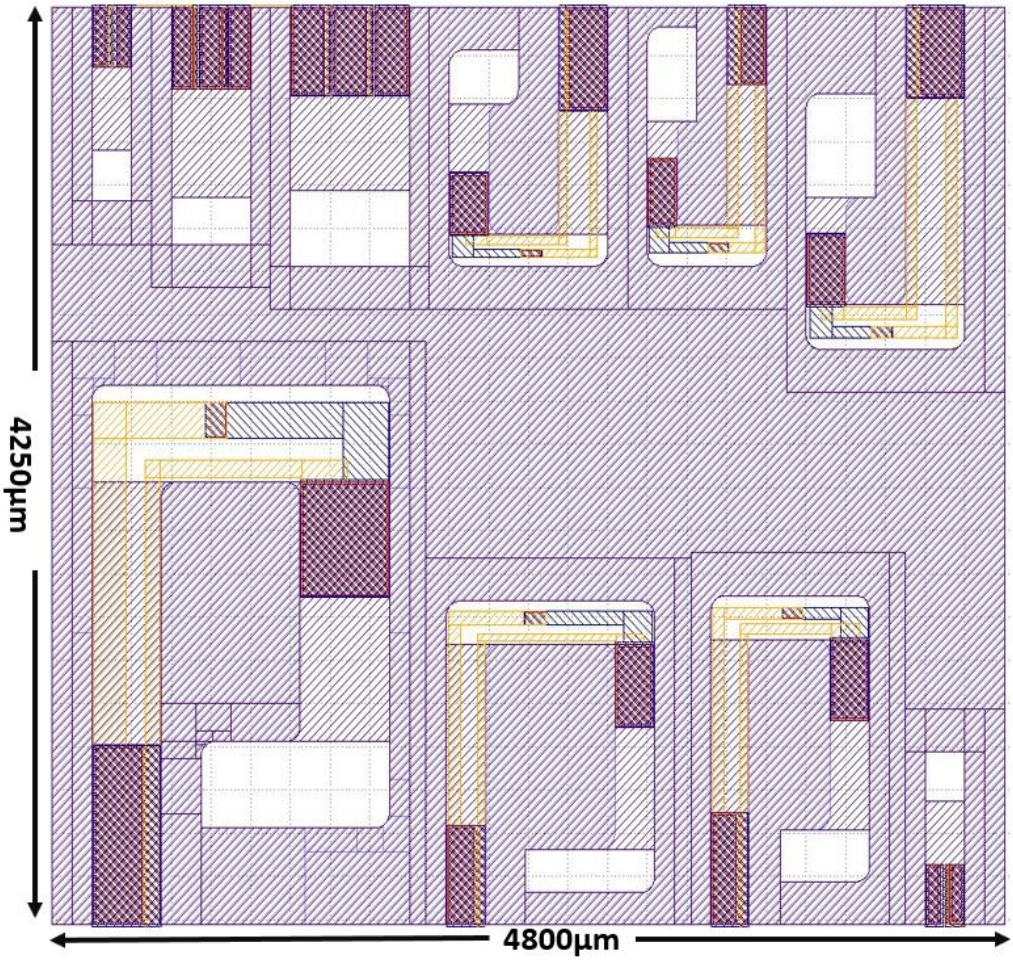

Figure 6.6. Layout of the P-shape device

6.1.2 Fabrication and Experimental Verification

Same fabrication methodology is followed for all devices which is previously explained. Fabricated devices are separated into individual chips. After whole fabrication and separating process are completed, each devices experimental characterization is conducted in order to observe their performance. In Figure 6.7, the fabricated device is presented under a microscope.

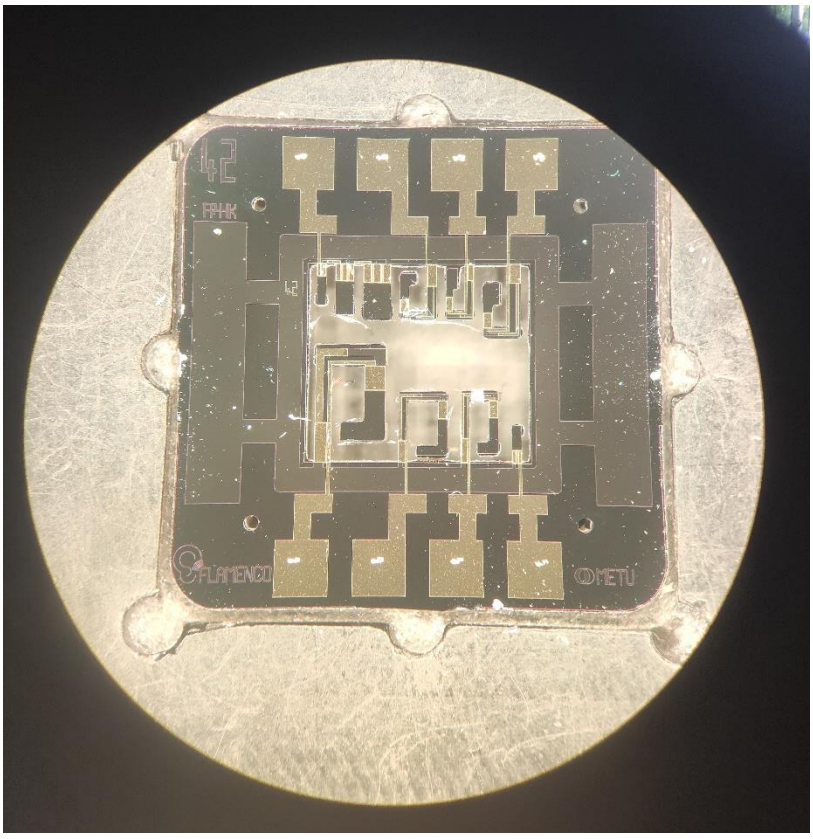

Figure 6.7. Fabricated P-shape device under microscope

Experimental characterization is started with short-capacitance test. After the capacitances of the devices are checked, the second experiment is conducted for resonance characterization with LCR meter. In Figure 6.8, results of the resonance characterization of the second channel are presented. From Figure 6.8, three resonances of the multi-mode P-shape device can be clearly observed.

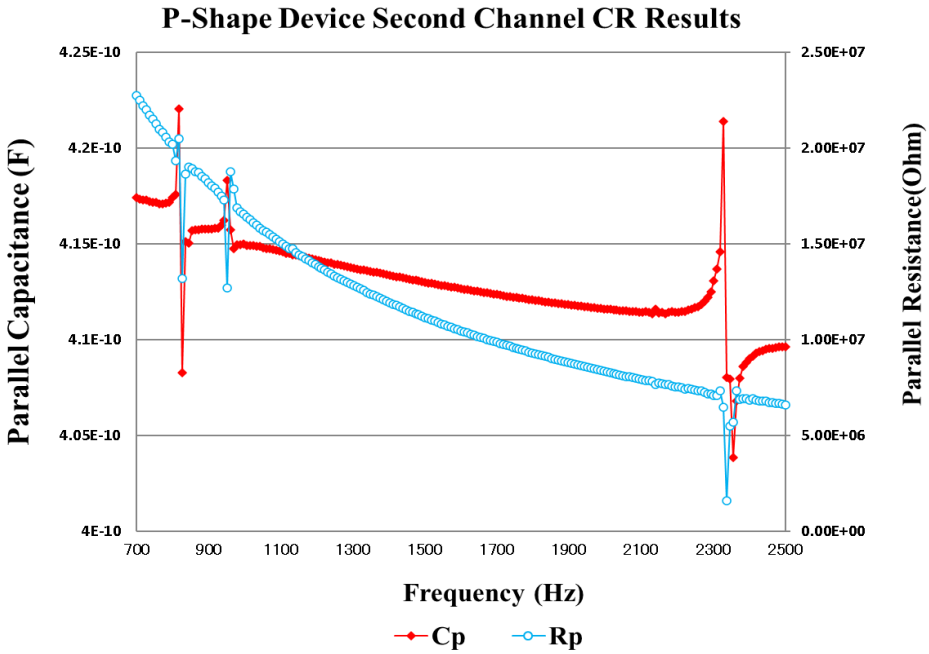

Figure 6.8. Resonance characterization of the second channel of P-shape device

In Figure 6.9, shaker table results for the P-shape devices at 0.1g are presented. Channels are defined by color coding. In Figure 6.10, the response of each channel is presented at 0.1g. This multi-mode design aims to cover the interval of 300Hz-6kHz with 10 beams with 22 consecutive resonances. From Figure 6.9and Figure 6.10, it is seen that 20 peaks can be observed. Responses of channels are consistent with simulations.

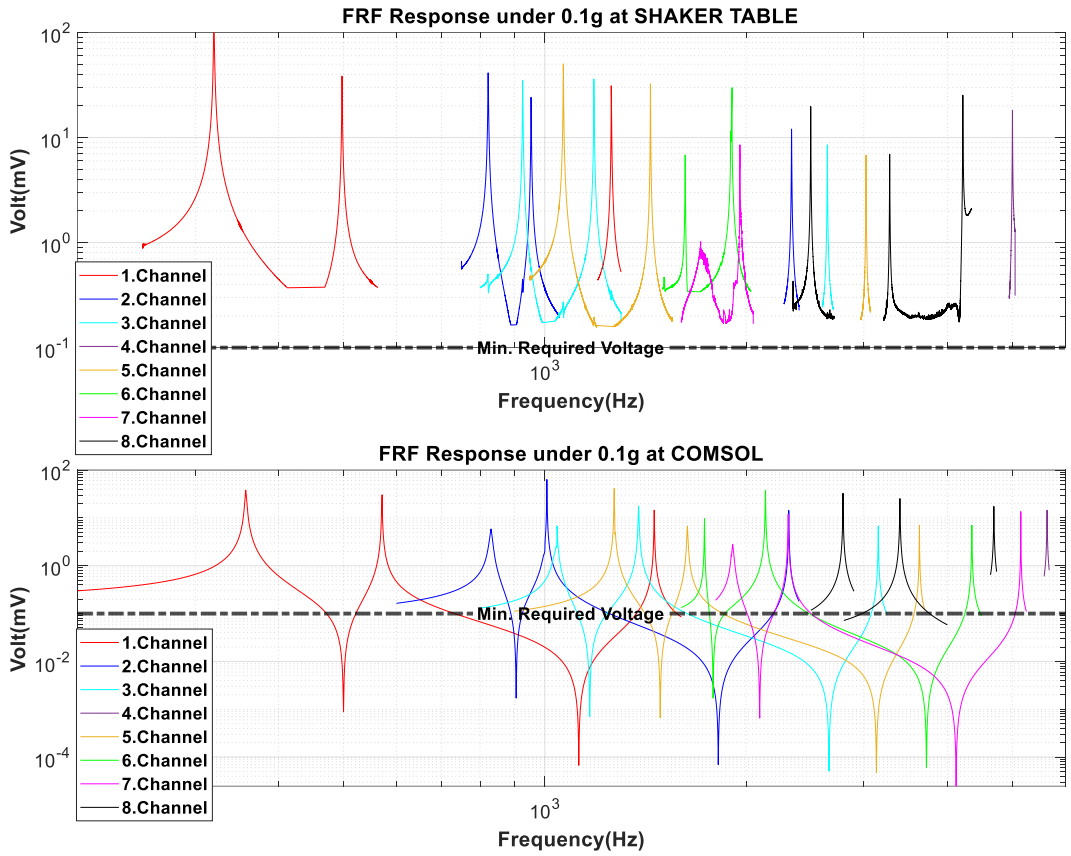

Figure 6.9. FRF results of the P-shape device under 0.1g. Top: Experimental results; Bottom: Simulation results

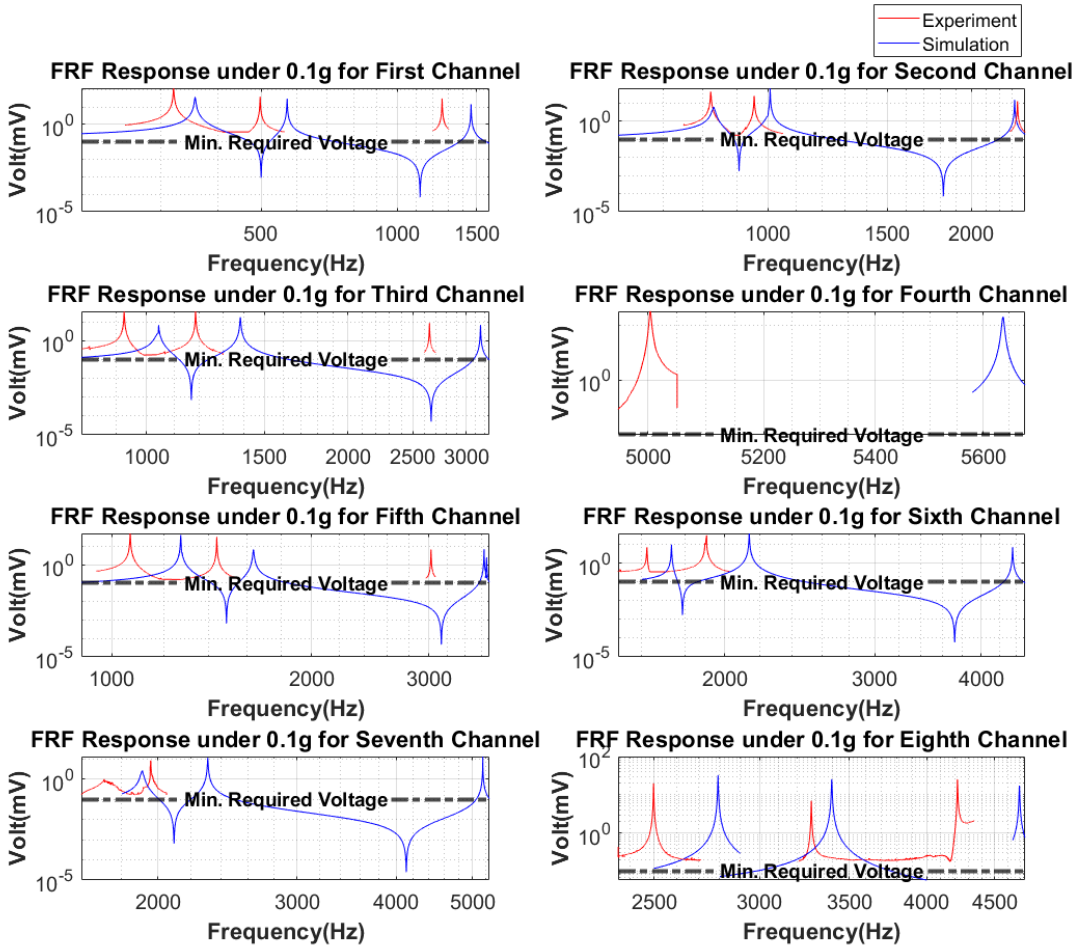

Figure 6.10. Channel by channel FRF results of P-shape devices

In Table 6.1, FRF results of the P-shape devices are presented for simulation and shaker table experiment. Resonance frequencies are in agreement with FEM simulations with a matching value of around 82.5%. The deviations are mostly due to defects from microfabrication processes. Voltage responses of the devices can deviate due to damping as explained in previous chapters. Moreover, in 2 channels one of the modes could not be observed. This may happen because of defects due to fabrication or problems due to experimental setup. However, the P-shape devices' general response is satisfactory when considering the covered range between 300Hz and 6kHz.

Table 6.1 FRF results of the P-shape device under 0.1g

Channel Number	Experiment		Simulation	
	Frequency (Hz)	Voltage (mV_{pp})	Frequency (Hz)	Voltage (mV_{pp})
1	319	120.45	356	160
	493	38.42	569	20
	1256	31.06	1451	11
2	822	41.3	830	50
	953	24.15	991	14
	2338	12.05	2264	7.5
3	926	34.87	1040	50
	1183	35.99	1377	32
	2645	8.53	3139	5.4
4	5004	18.18	5634	14
5	1065	50.25	1269	60
	1438	32.41	1658	14
	3022	6.81	3664	4.6
6	1621	6.83	1726	16
	1905	29.86	2108	32
	-	-	4270	5
7	1710	1.00	1908	28
	1958	8.56	2309	13
	-	-	5127	4.3
8	2498	19.75	2760	50
	3278	6.88	3611	28
	4218	25.29	4691	17

6.2 Comparison and Discussion of Multi-Mode Designs

In this research, two multi-mode designs are presented in an array configuration together with serially connected regular cantilevers with double PZT layer. Both of the designs aim to cover the interval of 300Hz and 6kHz by filtering the incoming sound mechanically.

M-shape devices are composed of 4 multi-mode M-shape cantilevers together with 11 serially connected, double PZT layer regular cantilevers. It covers the range with 23 consecutive frequencies. P-shape devices are composed of 6 multi-mode P-shape

cantilevers together with 4 serially connected, multi PZT layer regular cantilevers. It covers the range with 22 consecutive frequencies. In Figure 6.11, experimental FRF results of the two multi-mode designs are presented. From plots, it can be observed that both designs have good responses and almost cover whole range at 0.1g. However, P-shape designs frequencies are denser around 1 kHz, and it has lower coverage at low and high frequencies. On the other hand, in M-shape devices low and high frequencies are also be covered successfully, and, there are no gaps at the interval of 300Hz and 6kHz.

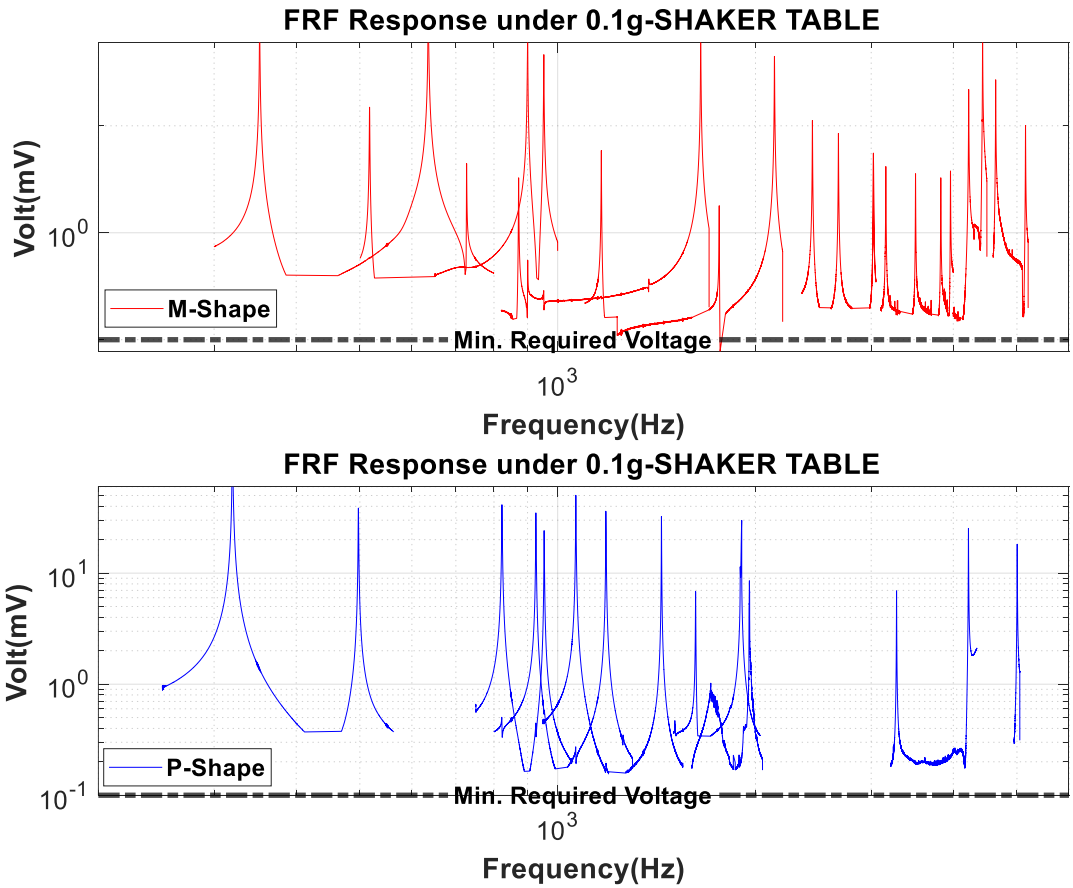

Figure 6.11. M-Shape and P-Shape devices FRF results under 0.1g at shaker table

Both multi-mode designs are successful and, they are promising not just for only acoustic sensor implications but also for other applications. However, for the purpose

of this research, M-shape design is more successful to cover the whole frequency range in a small footprint.

6.3 Summary

In this chapter, an alternative design possibility is examined for covering wider bandwidth. Different geometrical structures are examined and a multi-mode P-shape design is selected as an alternative. Design is implemented as a sensor configuration with serially connected regular cantilevers. The microfabrication flow of the device is the same as M-shape devices and consists of 6 photolithographic masks. Initial experimental testing of the devices is conducted with a multimeter and later experiments with, LCR meter and shaker table are performed. According to the responses from shaker table at 0.1g, maximum of 120 mV_{pp} is observed. Also, it is examined that sensor can almost sense whole interval of 300Hz and 6kHz at 0.1g. To sum up, P-shape devices may also be a good sensor alternative for FICI applications.

CHAPTER 7

CONCLUSION AND FUTURE WORK

In this research, a novel MEMS-based piezoelectric sensor is developed for fully implantable cochlear implants. Aim of the sensor is mechanically filtering the incoming sound and mimicking the cochlea; thus, a healthy hearing can occur. The analysis starts with middle ear modeling to understand vibration characteristics and dimensional constraints. Possible attachment mechanisms and locations for the sensor are studied, modeled, and tested. Two novel designs are proposed as a sensor. FEM simulations and experimental characterizations of the designs are conducted.

Accomplished tasks under this research can be summarized in two part. In the first part, the following tasks were achieved.

- Ossicle chain together with the tympanic membrane is modeled. FEM simulations of the middle ear model are conducted at ANSYS. Two main simulation algorithms are followed. Parameters are cross-calibrated in order to fit the model to the literature data.
- Possible locations for the sensor are examined based on the volume and vibration characteristics of the middle ear. Most suitable locations are decided as malleus and incus.
- Attachment mechanisms are examined. Biocompatible materials are studied; possible models are designed and simulated. Stress analysis of the mechanism is examined under mass loading of the sensor and impact and harmonic forces.
- Created middle ear FEM model is verified with vibration amplitude data of the incus short process from cadaver experiment.
- Designed attachment mechanism and location is verified with cadaver experiment.

After completing the middle ear modeling and attachment mechanism design, in the second part, piezoelectric sensor design and characterization is studied. Achieved tasks can be summarized as follows:

- Requirements and limitations are decided.
- Based on these criteria, novel sensor designs are examined in which intervals of 300Hz and 6kHz can be sensed. The main bottlenecks of the designs are volume limitations and interface circuit stimulation signal of 100μV. Thus, sensor which has a maximum footprint of 5mm to 5mm and provides minimum of 100μV is tried to developed.
- Multi-mode M-shape cantilevers combined with serially connected regular cantilevers are designed. As far as the known literature, this study is the first study to implement such a multi-mode M-shape design in a MEMS device.
- Resonances and output responses of the devices are arranged by cross-calibration with FEM simulations on COMSOL.
- Six mask fabrication of the sensor is conducted.
- Mechanical performance characterization of the sensor is examined at the shaker table for 0.1g. It is observed that whole desired interval of 300Hz and 6kHz is covered. Also, a maximum response of 138.1 mV_{pp} is observed at 0.1g.
- Acoustic performance characterization of the sensor is examined. Maximum responses of 546.16 mVpp, 252.57mVpp, and 69.70 mVpp for 100 dB, 90 dB, and 80 dB are recorded, respectively.
- Acoustic results of the M-shape multi-mode, multi-channel design are compared with the previous multi-channel design. The current design is 25% lighter and 35% smaller than the previous design. It is observed that bandwidth is increased around five times with the current design, and it also successfully covers most of the interval between 300Hz and 6kHz even at low sound pressure levels.
- An alternative multi-mode design which has a footprint of 4.80 mm to 4.25mm; and can sense the interval of 300Hz and 6 kHz is examined. After

literature research and multiple design trials, P-shape multi-mode cantilevers together with serially connected regular cantilevers are modeled. Parameters of the model are tuned by arranging the dimensions of the layers at COMSOL.

- The performance of the fabricated P-shape sensor is examined under 0.1g at the shaker table. A maximum voltage of 120 mVpp is seen. Additionally, shaker table experiments show that the sensor can perform almost at the entire frequency range between 300Hz and 6kHz for 0.1g acceleration input.
- Performances of the two multi-mode designs, M-shape and P-shape, are compared. It is observed that both of the designs are very promising. However, the P-shape design can sense around 1kHz range better than lower and higher frequency intervals whereas the M-shape design shows more continuous sensing; thus, it can be said that the M-shape design is better for sensing the interval of 300Hz and 6kHz.
- Feasibilty of multi-mode designs is verified.
- Lower limitation of the fabrication in terms of dimensions is verified. It is shown small and recessed beams with widths of 137.5 μm can be fabricated and they can show very good performance.

To sum up, two novel designs are proposed to cover the whole range of 300Hz and 6kHz at 0.1g; and also have a footprint of less than 5mm to 5mm. Proposed designs aim to solve the main drawbacks of cochlear implants by providing healthy sensing.

Although some good results are achieved from this research, there are some points should be further worked on:

- Constructed middle ear model should be further developed by considering the characteristics of the ossicles in more detail.
- Acoustical coupling of the middle ear model should be conducted.
- Sensor can be coupled to the middle ear model in order to observe the overall effect.

- Long-term stress results should be examined in order to predict the average life expectancy of the sensor.
- Acoustic experiments on P-shape design should be done in order to observe the performance of the device under sound.
- In-vitro and in-vivo experiments of the devices should be performed to observe the sensor's performance.
- Packaging of the device should be considered.
- Machine learning-based optimizations such as genetic algorithm and particle swarm optimization, can be used for further development of the devices before the next fabrication.

REFERENCES

[1] Albert Folch, *Introduction to BioMEMS*. CRC Press, 2013.

[2] "Out the Impacts on BioMEMS-yole," [Online]. Available: http://www.yole.fr/iso_upload/News/2020/PR_STATUS_BIOMEMS_INDUSTRY_MarketUpdate_YOLEGROUP_June2020.pdf. [Accessed 22 April 2022]."

[3] "'World Health Organization-Deafness and Hearing Loss,' [Online]. Available: https://www.who.int/news-room/fact-sheets/detail/deafness-and-hearing-loss. [Accessed 27 April 2022]."

[4] T. M. Önerci and Z. Önerci Altunay, "Ear," in *Diagnosis in Otorhinolaryngology: An Illustrated Guide*, T. M. Önerci and Z. Önerci Altunay, Eds. Cham: Springer International Publishing, 2021, pp. 1–84.

[5] L. Chittka and A. Brockmann, "Perception Space—The Final Frontier," *PLoS Biology*, vol. 3, no. 4, p. e137, Apr. 2005.

[6] L. L. Cunningham and D. L. Tucci, "Hearing Loss in Adults," *New England Journal of Medicine*, vol. 377, no. 25, pp. 2465–2473, Dec. 2017.

[7] T. O. Willcox and G. J. Artz, "AUDITORY SYSTEM DISORDERS," in *Neurology and Clinical Neuroscience*, Elsevier, 2007, pp. 329–335.

[8] J. B. Snow Jr, *Ballenger's manual of otorhinolaryngology head and neck surgery*. PMPH-USA, 2002.

[9] A. Forge and J. Schacht, "Aminoglycoside Antibiotics," *Audiology and Neurotology*, vol. 5, no. 1, pp. 3–22, 2000.

[10] P. Duggal and M. Sarkar, "Audiologic monitoring of multi-drug resistant tuberculosis patients on aminoglycoside treatment with long term follow-up," *BMC Ear, Nose and Throat Disorders*, vol. 7, no. 1, p. 5, Dec. 2007.

[11] A. C. Garinis *et al.*, "The cumulative effects of intravenous antibiotic treatments on hearing in patients with cystic fibrosis," *Journal of Cystic Fibrosis*, vol. 16, no. 3, pp. 401–409, May 2017.

[12] G. Al-Malky, S. J. Dawson, T. Sirimanna, E. Bagkeris, and R. Suri, "High-frequency audiometry reveals high prevalence of aminoglycoside ototoxicity in children with cystic fibrosis," *Journal of Cystic Fibrosis*, vol. 14, no. 2, pp. 248–254, Mar. 2015.

[13] R. D. Frisina *et al.*, “Comprehensive Audiometric Analysis of Hearing Impairment and Tinnitus After Cisplatin-Based Chemotherapy in Survivors of Adult-Onset Cancer,” *Journal of Clinical Oncology*, vol. 34, no. 23, pp. 2712–2720, Aug. 2016.

[14] E. A. R. Theunissen *et al.*, “Long-term hearing loss after chemoradiation in patients with head and neck cancer,” *The Laryngoscope*, vol. 124, no. 12, pp. 2720–2725, Dec. 2014.

[15] T. Mijovic, A. Zeitouni, and I. Colmegna, “Autoimmune sensorineural hearing loss: the otology-rheumatology interface,” *Rheumatology*, vol. 52, no. 5, pp. 780–789, May 2013.

[16] “‘Hearing aids - NIDCD.’ [Online]. Available: https://www.nidcd.nih.gov/sites/default/files/Documents/health/hearing/nidcd-hearing-aids.pdf. [Accessed: 03-Jul-2022].”

[17] J. R. Wyatt, J. K. Niparko, M. L. Rothman, and G. deLissovoy, “Cost effectiveness of the multichannel cochlear implant,” *The American journal of otology*, vol. 16, no. 1, pp. 52–62, 1995. [Online]. Available: http://europepmc.org/abstract/MED/8579178

[18] J. E. Saunders, H. W. Francis, and P. H. Skarzynski, “Measuring Success,” *Otology & Neurotology*, vol. 37, no. 2, pp. e135–e140, Feb. 2016.

[19] B. S. Wilson and M. F. Dorman, “Cochlear implants: A remarkable past and a brilliant future,” *Hearing Research*, vol. 242, no. 1–2, pp. 3–21, Aug. 2008.

[20] L. Tang, C. B. Thompson, J. H. Clark, K. M. Ceh, J. D. Yeagle, and H. W. Francis, “Rehabilitation and Psychosocial Determinants of Cochlear Implant Outcomes in Older Adults,” *Ear & Hearing*, vol. 38, no. 6, pp. 663–671, Nov. 2017.

[21] “‘Cochlear implants - NIDCD.’ [Online]. Available: https://www.nidcd.nih.gov/sites/default/files/Documents/health/hearing/CochlearImplants.pdf. [Accessed: 05-Jul-2022]. .”

[22] M. Tisch, “Implantable Hearing Devices,” *GMS Current Topics in Otorhinolaryngology, Head and Neck Surgery*, vol. 16, Dec. 2017.

[23] M. Yip, R. Jin, H. H. Nakajima, K. M. Stankovic, and A. P. Chandrakasan, “A Fully-Implantable Cochlear Implant SoC With Piezoelectric Middle-Ear Sensor and Arbitrary Waveform Neural Stimulation,” *IEEE Journal of Solid-State Circuits*, vol. 50, no. 1, pp. 214–229, 2015.

[24] V. Svatos, J. Pekarek, D. Dusek, J. Zak, Z. Hadas, and J. Prasek, “Design and Fabrication of Fully Implantable MEMS Cochlea,” *Procedia Engineering*, vol. 100, pp. 1224–1231, 2015.

[25] A. Heredia *et al.*, “Thin film membrane based on a-SiGe: B and MEMS technology for application in cochlear implants,” *Journal of Non-Crystalline Solids*, vol. 358, no. 17, pp. 2331–2335, 2012.

[26] J. Jang *et al.*, “A microelectromechanical system artificial basilar membrane based on a piezoelectric cantilever array and its characterization using an animal model,” *Scientific Reports*, vol. 5, no. 1, p. 12447, Dec. 2015.

[27] M. B. Yuksel, A. Koyuncuoglu, and H. Kulah, “Thin-Film PZT-Based Multi-Channel Acoustic MEMS Transducer for Cochlear Implant Applications,” *IEEE Sensors Journal*, vol. 22, no. 4, pp. 3052–3060, Feb. 2022.

[28] M. B. Yüksel, B. İlik, A. Koyuncuoğlu, and H. Külah, “Multi-channel thin film piezoelectric acoustic transducer for cochlear implant applications,” in *2019 IEEE SENSORS*, 2019, pp. 1–4.

[29] B. İlik, A. Koyuncuoğlu, Ö. Şardan-Sukas, and H. Külah, “Thin film piezoelectric acoustic transducer for fully implantable cochlear implants,” *Sensors and Actuators A: Physical*, vol. 280, pp. 38–46, 2018.

[30] H. Uluşan, A. Muhtaroglu, and H. Kulah, “A Sub-500 lW Interface Electronics for Bionic Ears H,” *IEEE Access*, vol. PP, p. 1, Sep. 2019.

[31] A. Koyuncuoglu *et al.*, “Bulk PZT Cantilever Based MEMS Acoustic Transducer for Cochlear Implant Applications †,” *Proceedings*, vol. 1, Aug. 2017.

[32] T. Cheng and R. Z. Gan, “Experimental measurement and modeling analysis on mechanical properties of tensor tympani tendon,” *Medical Engineering & Physics*, vol. 30, no. 3, pp. 358–366, 2008.

[33] E. Unur, H. Ulger, and N. Ekinci, “Morphometric and morphological variations of middle ear ossicles in the newborn,” *Erciyes Medical Journal*, vol. 24, pp. 57–63, Jan. 2002.

[34] S. Wadhwa, J.M. Kaul, and A.K. Agarwal, “Morphometric study of stapes and its clinical implications,” *Journal of Anatomical Society of India*, vol. 54, no. 2, pp. 1–9, 2005.

[35] N. K. Harneja and R. P. Chaturvedi, “A study of the human ear ossicles,” *Indian Journal of Otolaryngology*, vol. 25, no. 3, pp. 154–160, 1973.

[36] B. Arensburg, M. Harell, and H. Nathan, “The human middle ear ossicles: Morphometry, and taxonomic implications,” *Journal of Human Evolution*, vol. 10, no. 2, pp. 199–205, 1981.

[37] R. Rusinek, M. Szymanski, and R. Zablotni, “Biomechanics of the Human Middle Ear with Viscoelasticity of the Maxwell and the Kelvin–Voigt Type and Relaxation Effect,” *Materials*, vol. 13, p. 3779, Aug. 2020.

[38] Q. Sun, R. Z. Gan, K.-H. Chang, and K. J. Dormer, “Computer-integrated finite element modeling of human middle ear,” *Biomechanics and Modeling in Mechanobiology*, vol. 1, no. 2, pp. 109–122, 2002.

[39] P. Ferris and P. Prendergast, “Middle-ear dynamics before and after ossicular replacement,” *Journal of biomechanics*, vol. 33, pp. 581–590, Jun. 2000.

[40] M. D. Graham, C. Reams, and R. Perkins, “Human Tympanic Membrane — Malleus Attachment Preliminary Study,” *Annals of Otology, Rhinology & Laryngology*, vol. 87, no. 3, pp. 426–431, May 1978.

[41] M.S. Vlaming, “Middle ear mechanics studied by laser Doppler interferometry,” TU Delft.

[42] T. Cheng and R. Z. Gan, “Mechanical Properties of Stapedial Tendon in Human Middle Ear,” *Journal of Biomechanical Engineering*, vol. 129, no. 6, pp. 913–918, Dec. 2007.

[43] T. Cheng and R. Z. Gan, “Experimental measurement and modeling analysis on mechanical properties of tensor tympani tendon,” *Medical Engineering & Physics*, vol. 30, no. 3, pp. 358–366, 2008.

[44] T. Cheng and R. Z. Gan, “Mechanical properties of anterior malleolar ligament from experimental measurement and material modeling analysis,” *Biomechanics and Modeling in Mechanobiology*, vol. 7, no. 5, pp. 387–394, 2008.

[45] S. Nishihara and R. L. Goode, “Measurement of tympanic membrane vibration in 99 human ears,” in *Middle Ear Mechanics in Research and Otosurgery, edited by K.-B.Hüttenbrink (Dept. of Oto-Rhino-Laryngology, Dresden University of Technology, Dresden, Germany*, 1997, pp. 91–93.

[46] N. Hato, S. Stenfelt, and R. Goode, “Three-Dimensional Stapes Footplate Motion in Human Temporal Bones,” *Audiology & neuro-otology*, vol. 8, pp. 140–152, May 2003.

[47] S. Nishihara, H. Aritomo, and R. L. Goode, “Effect of Changes in Mass on Middle Ear Function,” *Otolaryngology–Head and Neck Surgery*, vol. 109, no. 5, pp. 899–910, Nov. 1993.

[48] D. J. Young, M. A. Zurcher, T. T. Trang, C. A. Megerian, and W. H. Ko, “Characterization of Ossicular Chain Vibration at the Umbo: Implications for a Middle Ear Microelectromechanical System Design,” *ENT Journal*, vol. 89, pp. 21–26, 2010.

[49] X. Zhang, X. Guan, D. Nakmali, V. Palan, M. Pineda, and R. Z. Gan, “Experimental and Modeling Study of Human Tympanic Membrane Motion in the Presence of Middle Ear Liquid,” *Journal of the Association for Research in Otolaryngology*, vol. 15, no. 6, pp. 867–881, 2014.

[50] W. Chien, J. J. Rosowski, M. E. Ravicz, S. D. Rauch, J. Smullen, and S. N. Merchant, “Measurements of stapes velocity in live human ears,” *Hearing research*, vol. 249, no. 1–2, pp. 54–61, 2009.

[51] S. Labassi, M. Beliaeff, V. Péan, and P. Van de Heyning, “The Vibrant Soundbridge® middle ear implant: A historical overview,” *Cochlear Implants International*, vol. 18, no. 6, pp. 314–323, Nov. 2017.

[52] J. M. Anderson, “Biocompatibility,” *Polymer Science: A Comprehensive Reference, 10 Volume Set*, vol. 9, pp. 363–383, Jan. 2012.

[53] Stoeckel, “The Shape Memory Effect Phenomenon, Alloys and Applications,” in *Proceedings: Shape memory alloys for power systems EPRI*, 1995, pp. 1–13.

[54] G. L. Kelly and B. Eiseman, “Development of a new vascular prosthetic: lessons learned,” *Archives of Surgery*, vol. 117, no. 10, pp. 1367–1370, 1982.

[55] V. Hasırcı and N. Hasırcı, “Titanium Alloys,” in *Fundamentals of Biomaterials*, New York: Springer International Publishing, 2018, pp. 42–43.

[56] H. Molly Subhash, A. Nguyễn, R. Wang, S. Jacques, N. Choudhury, and A. Nuttall, “Feasibility of spectral-domain phase-sensitive optical coherence tomography for middle ear vibrometry,” *Journal of biomedical optics*, vol. 17, p. 60505, Jun. 2012.

[57] R. Z. Gan, B. Feng, and Q. Sun, “Three-Dimensional Finite Element Modeling of Human Ear for Sound Transmission,” *Annals of Biomedical Engineering*, vol. 32, no. 6, pp. 847–859, 2004.

[58] A. H. Voie and F. A. Spelman, “Three-dimensional reconstruction of the cochlea from two-dimensional images of optical sections,” *Computerized medical imaging and graphics*, vol. 19, no. 5, pp. 377–384, 1995.

[59] R. Z. Gan, B. P. Reeves, and X. Wang, “Modeling of Sound Transmission from Ear Canal to Cochlea,” *Annals of Biomedical Engineering*, vol. 35, no. 12, pp. 2180–2195, 2007.

[60] M. Zurcher, D. Young, M. Semaan, and C. Megerian, *Effect of Incus Removal on Middle Ear Acoustic Sensor for a Fully Implantable Cochlear Prosthesis*. 2006.

[61] V. Evans, “Newton’s Laws, G-forces and the impact on the brain,” *Australasian Journal of Neuroscience*, vol. 30, pp. 24–29, Jan. 2020.

[62] Q. Wu *et al.*, “Impact response and energy absorption of human skull cellular bones,” *Journal of the Mechanical Behavior of Biomedical Materials*, vol. 81, pp. 106–119, 2018.

[63] R. Nadda and C. K. Nirala, “Chapter 5 - Recent developments in spark erosion–based machining processes: A state of the art in downscaling of spark erosion based machining processes,” in *Handbooks in Advanced Manufacturing*, K. Gupta and A. B. T.-A. M. and F. Pramanik, Eds. Elsevier, 2021, pp. 177–215.

[64] “INEMO inertial module: Always-on 3D accelerometer and 3D gyroscope.” [Online]. Available: https://www.st.com/resource/en/datasheet/lsm6dsl.pdf. [Accessed: 06-Jun-2022].

[65] R. Z. Gan, M. W. Wood, R. K. Dyer, and K. J. Dormer, “Mass Loading on the Ossicles and Middle Ear Function,” *Annals of Otology, Rhinology & Laryngology*, vol. 110, no. 5, pp. 478–485, May 2001.

[66] D. J. Kelly, P. J. Prendergast, and A. W. Blayney, “The Effect of Prosthesis Design on Vibration of the Reconstructed Ossicular Chain: A Comparative Finite Element Analysis of Four Prostheses,” *Otology \& Neurotology*, vol. 24, pp. 11–19, 2003.

[67] B. Dahroug, B. Tamadazte, S. Weber, L. Tavernier, and N. Andreff, “Review on Otological Robotic Systems: Toward Microrobot-Assisted Cholesteatoma Surgery,” *IEEE Reviews in Biomedical Engineering*, vol. 11, pp. 125–142, 2018.

[68] T. Liem, “Chapter 17 - The organ of hearing and balance,” T. B. T.-C. O. (Second E. Liem, Ed. Edinburgh: Churchill Livingstone, 2004, pp. 605–633.

[69] H. Külah *et al.*, “A Fully-Implantable Mems-Based Autonomous Cochlear Implant,” in *2022 IEEE 35th International Conference on Micro Electro Mechanical Systems Conference (MEMS)*, 2022, pp. 396–399.

[70] R. J. (Ronald J. . Baken and R. F. Orlikoff, *Clinical measurement of speech and voice*, 2nd ed. San Diego: Singular Thomson Learning, 2000.

[71] N. R. French and J. C. Steinberg, “Factors Governing the Intelligibility of Speech Sounds,” *The Journal of the Acoustical Society of America*, vol. 19, no. 1, pp. 90–119, Jan. 1947.

[72] Y. Suzuki and H. Takeshima, “Equal-loudness-level contours for pure tones.,” *The Journal of the Acoustical Society of America*, vol. 116 2, pp. 918–933, 2004.

[73] L. Wagner, R. Altindal, S. K. Plontke, and T. Rahne, “Pure tone discrimination with cochlear implants and filter-band spread,” *Scientific Reports*, vol. 11, no. 1, p. 20236, 2021.

[74] L. Beker, Ö. Zorlu, N. Goksu, and H. Kulah, *Stimulating auditory nerve with MEMS harvesters for fully implantable and self-powered cochlear implants*. 2013.

[75] P. Muralt, “Piezoelectric thin films for mems,” *Integrated Ferroelectrics*, vol. 17, no. 1–4, pp. 297–307, Sep. 1997.

[76] M. Dekkers *et al.*, “The significance of the piezoelectric coefficient$d_{31,\mathrm{eff}}$determined from cantilever structures,” *Journal of Micromechanics and Microengineering*, vol. 23, no. 2, p. 25008, 2012.

[77] M. D. Nguyen, R. Tiggelaar, T. Aukes, G. Rijnders, and G. Roelof, “Wafer-scale growth of highly textured piezoelectric thin films by pulsed laser deposition for micro-scale sensors and actuators,” *Journal of Physics: Conference Series*, vol. 922, p. 12022, 2017.

[78] T. Kamel *et al.*, “Modeling and characterization of MEMS-based piezoelectric harvesting devices,” *Journal of Micromechanics and Microengineering*, vol. 20, p. 105023, Sep. 2010.

[79] M. Wu *et al.*, “Multi-resonant wideband energy harvester based on a folded asymmetric M-shaped cantilever,” *AIP Advances*, vol. 5, no. 7, p. 77149, Jul. 2015.

[80] M. A. Zurcher, M. Semaan, C. A. Megerian, W. H. Ko, and D. J. Young, “A MEMS capacitive accelerometer design as middle ear microphone based on

ossicular chain micromechanic characterization at umbo for fully implantable cochlear prosthesis," *Sensors and Materials*, vol. 22, pp. 297–312, 2010.

[81] S. Majee, D. Barshilia, S. Kumar, P. Mishra, and J. Akhtar, "Signature of growth deposition technique on the properties of PECVD and thermal SiO2," *AIP Conference Proceedings*, vol. 1989, no. 1, p. 20023, Jul. 2018.

[82] A. Koyuncuoğlu, D. Işık Akçakaya, Ö. Şardan Sukas, and H. Külah, "Wet etching of platinum (Pt) electrodes for piezoelectric transducers using a thick photoresist mask," *Micro and Nano Engineering*, vol. 16, p. 100153, 2022.

[83] P. Ashrafi, "A synthetic tympanic membrane for middle ear acoustic sensor tests of a fully implantable cochlear prothesis," 2018.

[84] A. K. Soydan, "System integration of mems devices on flexible substrates," Middle East Technical University, 2019.

[85] M. B. Yüksel, "Mems based multi-channel piezoelectric acoustic transducer for fully implantable cochlear implants," Middle East Technical University, 2020.

[86] S. Nabavi and L. Zhang, "Design and Optimization of Wideband Multimode Piezoelectric MEMS Vibration Energy Harvesters †," *Proceedings*, vol. 1, p. 586, Aug. 2017.

[87] P. Udvardi *et al.*, "Spiral-Shaped Piezoelectric MEMS Cantilever Array for Fully Implantable Hearing Systems," *Micromachines*, vol. 8, p. 311, Oct. 2017.